NEUTRON SCATTERING OFF WEYL SEMIMETALS

by

Michael Bjerngaard

A dissertation submitted to The Johns Hopkins University in conformity with the requirements for the degree of Doctor of Philosophy.

Baltimore, Maryland

August, 2020

Abstract

Weyl semimetals are a recently discovered, fascinating class of materials with a topologically non-trivial band structure in three dimensions, due to linearly crossing conduction and valence bands, forming so-called Weyl nodes. Weyl nodes are associated with a chirality meaning that excitations' spins are aligned parallel or antiparallel to their direction of momentum. A consequence of Weyl nodes, for example, is desirable topological responses to electromagnetic fields. Bulk experimental probes that can measure properties of its bulk band topology, such as the chirality and spin-momentum locking are needed.

We show that inelastic neutron scattering can provide a new, unexpected way to detect type-I Weyl nodes with a realistic anisotropy. A generic material does not have relativistic symmetry. However, in many circumstances, the dynamics of the excitations can be mapped to a relativistic process. The neutron's coupling to Weyl fermions breaks this symmetry, but only in an indirect way. These material-dependent couplings act as an emergent magnetic moment and can be larger than the ordinary Bohr magneton, thus compensating for the small density of states. This can cause the

ABSTRACT

neutron scattering rate to be large enough for experiments to be practically possible. The cross-section of a fully unpolarized measurement reveals spin-momentum locking of Weyl fermions. Furthermore, kinematic constraints allow one to control the momentum and spin of the excited particle-hole pairs at maximum momentum transfer for a given energy transfer. Consequently, in an experiment with incident polarized neutrons, the scattered neutron beam remains fully polarized in a direction determined by the coupling parameters. This has the remarkable consequence that the chirality of Weyl fermions for inversion symmetric nodes is measurable independently of the many unknown couplings, which reflects its topological character.

This detailed analysis opens new questions about Weyl excitations in external magnetic fields (not necessarily induced by neutrons). For example, this theory suggests that neutron scattering can generate highly unusual particle-hole bound states of the Weyl excitations. These would have strong momentum-dependent properties, and the dynamics of these might be explained through an emergent electric dipole moment (which is not ruled out by symmetry unlike the case of a free electron).

Primary Reader and Advisor: Oleg Tchernyshyov

Secondary Reader: Yi Li

Acknowledgments

Foremost, I owe my deepest gratitude to my present advisor Oleg Tchernyshyov and previous advisor Ari M. Turner for their patience and teachings of different aspects of theoretical condensed matter physics. Especially, I would like to thank Collin Broholm for his encouragement in the project that is the content of this dissertation, and sharing his knowledge of experimental neutron scattering. Also, I highly valued the numerous explanations of neutron scattering from Wesley T. Fuhrman, Guy Marcus, Youzhe Chen and Jonathan Gaudet. I appreciate the close collaboration with Derek Reitz, Bogdan Galilo, Maciej Misiorny, and Jens Paaske on various projects, and discussions with Sayak Dasgupta and Yi Li. Additionally, I would like to thank my officemates Anirban Ghosh, Jake Mokris and Haoyu Wang for many engaging conversations about physics and beyond. Lastly, a special thanks goes to Nariman El Said for help proof reading this dissertation and her companionship, along with comrades and friends on-and off campus.

Contents

List of Figures

Chapter 1

Introduction

In 1928, P. A. M. Dirac [1] presented the equation that describes free relativistic spin-$\frac{1}{2}$ electrons. The following year, H. Weyl [2] proposed that the massless limit of the $(3+1)$ dimensional Dirac equation describes Weyl fermions characterized by having a conserved chirality $\chi = 1$ or -1. That is, spin is either aligned parallel or antiparallel with the direction of canonical momentum. To this day, Weyl fermions have not been detected in nature.

As often before, elements of high-energy particle physics appear in condensed matter systems as emergent phenomena. Here, this is the beautiful phenomenon in which a macroscopic solid, containing a vast number of electrons interacting with one another in the potential of an underlying lattice, dresses the electrons to become simple non-interacting quasi-particles. In this new context, the Weyl equation appears as describing two linear energy bands crossing at some point in the Brillouin zone.

As Lorentz invariance is broken, the Weyl equation describing quasi-particles allows for a modification to that sought to describe fundamental particles. Yet, there is still a coupling between the velocity and spin of these excitations, called spin-momentum locking, with the caveat that spin is no longer related to real spin in a definite way and is therefore referred to as pseudospin.

While this has been know since the 1930's, only recently [3, 4, 5, 6] was it realized that Weyl nodes have a topological meaning in the context of topological semimetal materials. The chirality $\chi = \pm 1$ assigned to a Weyl node is a topological number, or a charge, and the total charge of Weyl nodes in a material, referred to as a Weyl semimetal, has to be zero [7, 8]. This endows it with topological responses [9], for example the chiral anomaly, and topological surface states, called Fermi arcs.

To identify a given material as a Weyl semimetal, one can in principle detect any of the above properties. The ongoing discovery [10, 11, 12] of topological semimetals has benefited from the application of a variety of experimental techniques, each having its own strength and limitation. Common for several of these techniques is that contributions from Fermi surfaces are superimposed, such that the overall response comes from the entire Brillouin zone and a full understanding of the probe response requires band calculations to varying extent. Inherent surface probes such as angle-resolved photoemission spectroscopy [13, 14, 15, 16, 17] and scanning tunneling microscopy [18, 19] have been very successful in measuring the Fermi arc guided by band structure calculations. To date, only a few experiments have not rigorously

met the necessary criteria [20]. The latter probe has identified the surface-bulk connectivity, and the former has directly measured the bulk valence band dispersion, despite not being fully resolved due to finite resolution effects. Quantum oscillations [21, 22, 23] have been used to reconstruct bulk Fermi surfaces, and surface Fermi arcs at both top and bottom surfaces that completes a loop via bulk states. However, this technique has limitations for topological characterizations of multi-band systems. In addition to these efforts, it is necessary to find probes that can characterize the bulk topology of nodes. To this end, there are interesting proposals for using polarization-resolved x-ray scattering [24], circular dichroism [25], and the circular photogalvanic effect [26] to measure the chirality of nodes.

1.1 Motivation, Aim, and Structure of Dissertation

Because of the aforementioned reasons, Weyl semimetals have drawn attention from neutron scattering experimentalists aspiring to investigate properties of Weyl excitations. Yet the literature lacks a theory[1] elucidating how to disentangle the necessary signatures in the neutron cross-section. This dissertation addresses this gap. The contents of this dissertation are based on parts of the publication Ref. [28] in

[1] One interesting recent preprint, Ref. [27], develops a theory of neutron scattering off magnon Weyl nodes. This theory utilizes similar ideas as those in our publication Ref. [28].

collaboration with Bogdan Galilo and supervised by Ari M. Turner.

When neutrons pass through a material, they may bounce off various excitations in it. We simply ask how, from the nature of these interactions, is it possible to recognize the existence of Weyl nodes from the scattering cross-section. Excitations of Weyl nodes are characterized by their spin-momentum locking. This means that a small perturbation, which induces a slight change of their momentum, leads to very strong effects on the excitations' pseudospin. We will identify characteristic properties of the neutron scattering cross-section that reflect this property, thus providing an indirect measurement of the bulk topology of Weyl semimetals.

The inspiration to use neutron scattering in this way to probe Weyl nodes, and to construct the cross-section, comes from the massless neutrino[2] theory's [29, 30, 31, 32] attempt to describe parity violation in β-decay. The analogy between these two very different theories is illustrated by the proposal of Lee and Yang, that the possibility of non-conservation of parity could be observed by measuring the angular distribution of electrons emitted in β-decay. That is so because, the spin of a nucleus is invariant under parity but momentum is odd under parity, the direction of the decay products (including an electron) being emitted is changed under parity. For a spinning nucleus emits an electron in the direction of its intrinsic spin, in the image process, the image nucleus will emit an electron in the opposite direction of its spin, see Fig. 1.1. Hence, if

[2]Here neutrinos satisfy the relativistic Weyl equation.

parity was conserved, there would not be any preferred direction in the distribution of emitted particles along the axis of the nucleus' spin, because the image process always accompanies the actual process. However, this assumption contradicted experimental observations and therefore lead to the discovery of parity violation. This further implies that only particles and antiparticles of certain chiralities participate in this weak process.

The basic property of β-decay, that the direction of the emitted particles is correlated to the initially aligned spin of the nucleus, motivates that one can use neutron scattering to detect excitation of Weyl nodes, which are chiral excitations at low energy. A neutron acts like a magnetic perturbation to the Weyl node and this will excite two relativistic bulk excitations analog to the emission of an electron and an antineutrino in the transition of a neutron to a proton. The rate of neutron scattering depends on the probability of creating such a pair, the excitations of which have momentum locked to spin. The cross-section will therefore contain the information about how the excitations' spin is correlated to their direction of motion. So, somewhat along the lines of Lee and Yang's suggestion, we predict how the momentum of the Weyl excitations will be correlated to the spin of the perturbing incident neutron. This is given by the cross-section recorded by the neutron detector. From this, we will interpret the cross-section in various ways to find characteristics of Weyl nodes.

To recap, the primary aim of this dissertation is to investigate whether inelastic

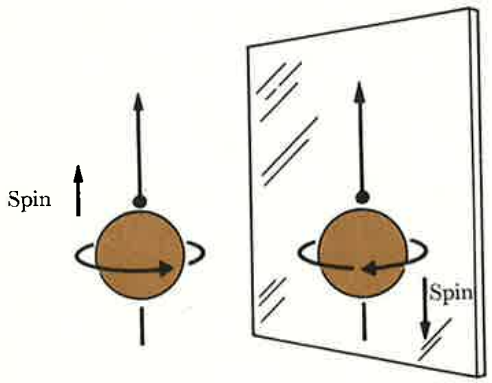

Figure 1.1: A spinning nucleus emitting particles in the direction of its spin. In the mirror, the image nucleus is emitting particles in the direction opposite to the spin. From Ref. [30].

neutron scattering can probe Weyl nodes. The most fundamental characteristic of the Weyl semimetal bulk topology is encoded in the chirality, also known as the topological charge, of Weyl nodes which we are interested in measuring. In the case that chirality is inaccessible to measurement, then measuring spin-momentum locking can yield a bulk signature of Weyl nodes in Weyl semimetal materials.

The rest of this chapter gives a short introduction to Weyl semimetals. Chapter 2 is a preliminary study of neutron scattering off ideal Weyl nodes, before the remaining part considers nodes with realistic anisotropy. Here, the basic ideas and problems associated with studying Weyl nodes with neutron scattering are outlined. Chapter 3 is devoted to the theoretical formulation and derivation of the inelastic neutron cross-section. This basically consists of mapping the excitations created in the scattering process to a relativistic process, like the creation of an electron and antineutrino in β-decay. Because the spin of a Weyl fermion is often pseudospin in materials, the interaction of the neutron with Weyl fermions takes the form of an emergent magnetic moment, which is determined by a scourge of anisotropic g-factors

specified by the Weyl semimetal band structure. The scattering rate for neutrons is thus equivalent to the rate of exciting relativistic Weyl fermions with an applied field of a certain polarization determined by g-fators of the neutron-Weyl fermion interaction. Chapter 5 illustrates some of the concepts needed to use this theory with a toy model of a Weyl semimetal. In this model, where Weyl nodes are close, the g-factors can be very large, such that the magnetic moment induced by the neutron's magnetic field is much stronger than that of a free electron. In the context of this dissertation, the magnetic field is induced by the magnetic moment of the neutron, but it does not have to be. The cross-sections that are measured in experiments are formally summarized in Ch. 4, and Ch. 6 offers ways to interpret them. While the cross-section's intensity distribution is highly influenced by the many g-factors, it turns out that it is possible to measure the dispersion and probe spin-momentum of the excitations in the easiest fully unpolarized experiment. Also, the cross-section scattering edge is discontinuous, which is a strong signature of scattering between Weyl nodes transformed into Lorentz invariant form, and furthermore, it has a pattern reflecting scattering Weyl fermions. Lastly, it is possible to measure the chirality of inversion-symmetric Weyl nodes. This is remarkable as this measurement can be done without any prior knowledge of the g-factors, and furthermore, there is not a simple analogy of spin-conservation in the scattering process. Chapter 7 contains a summary and discusses prospects of using this theory, together with suggestions for extending this work. The theory developed suggests some interesting questions, such

as whether neutron scattering generates highly unusual particle-hole bound states of the Weyl excitations. These would have strong momentum-dependent properties, and the dynamics of these might be explained through an emergent electric dipole moment (which is not ruled out by symmetry unlike the case of a free electron).

1.2 Weyl Fermion - Massless Electron to Quasi-particle

As mentioned above, one of the pillars of modern physics is the Dirac equation [31, 33] which reconciled quantum mechanics with special relativity in the description of spin-$\frac{1}{2}$ particles. As a Schrödinger equation $H\psi = E\psi$, its Hamiltonian reads,

$$H = \begin{pmatrix} -c\boldsymbol{\sigma}\cdot\mathbf{k} & mc^2 \\ mc^2 & c\boldsymbol{\sigma}\cdot\mathbf{k} \end{pmatrix}. \tag{1.1}$$

Here, the linear 3-momentum is $\mathbf{k} = (k_x, k_y, k_z)$, c is the speed of light, and $\boldsymbol{\sigma} = (\sigma_x, \sigma_y, \sigma_z)$ denotes a vector of the three Pauli matrices. The Dirac 4-spinor $\psi = (\psi_L, \psi_R)^T$ mixes the 2-spinors $\psi_{L,R}$ due to the mass m of the electron. The energy spectrum of Eq. (1.1) is relativistic $E = \pm c\sqrt{|\mathbf{k}|^2 + (cm)^2}$ and degenerate with a gap $\Delta = 2m$. In the massless, or ultra-relativistic, limit of an electron, $m = 0$, the Dirac

equation decouples into the Weyl equations,

$$-c\boldsymbol{\sigma}\cdot\mathbf{k}\psi_L = E\psi_L \quad , \quad c\boldsymbol{\sigma}\cdot\mathbf{k}\psi_R = E\psi_R\,, \tag{1.2}$$

with energy dispersing linearly $E = c|\mathbf{k}|$ with the speed of light. The 2-spinors ψ_L and ψ_R are eigenspinors of $\boldsymbol{\sigma}\cdot\hat{\mathbf{k}}$ with eigenvalues $\chi = -1$ and 1, respectively, also referred to as left- and right-handedness, meaning that the spin is aligned antiparallel and parallel to its motion, respectively. This is illustrated in Fig. 1.2 for the right-handed case.

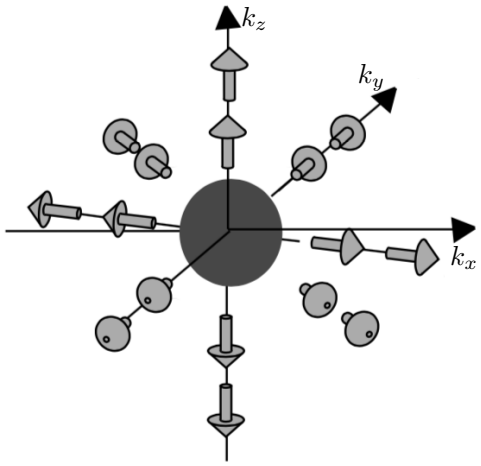

Figure 1.2: Hedgehog in momentum space. The average of $\boldsymbol{\sigma}$ in an eigenspinor points parrallel to momentum for chirality $\chi = +1$. Adapted from Ref. [3].

The fundamental difference between Dirac and Weyl fermions is the property of handedness. One definition of handedness that applies to both massive and massless

particles is helicity, associated with the helicity operator,

$$h = \mathbf{\Sigma} \cdot \hat{\mathbf{k}} \quad , \quad \mathbf{\Sigma} = \begin{pmatrix} \boldsymbol{\sigma} & 0 \\ 0 & \boldsymbol{\sigma} \end{pmatrix} , \tag{1.3}$$

which is a measure of the projection of spin along 3-momentum. Eigenvalues of h are -1 and 1, which we call left- and right-helical. What makes this interesting is that the operator h commutes[3] with both Eq. (1.1) and (1.2), meaning that handedness is a constant of time for both Dirac and Weyl particles. However, helicity of a massive particle depends on the frame of reference. One can boost it to another frame where momentum is opposite, but spin is unchanged. For massless particles traveling at the speed of light, one cannot boost to such a frame. Hence, the Dirac fermion cannot be exclusively left- or right-helical in all frames, whereas a Weyl fermion is exclusively left- or right-helical. Another sense of handedness is associated with a matrix γ^5 with the properties $\gamma^{5,\dagger} = \gamma^5$ and $(\gamma^5)^2 = 1$ having two eigenvalues -1 and 1 referred to as left- and right-chiral. Here, the Weyl/chiral representation is useful, in which,

$$\gamma^5 = \begin{pmatrix} -\sigma^0 & 0 \\ 0 & \sigma^0 \end{pmatrix} , \tag{1.4}$$

where σ^0 is the 2×2 identity matrix. The chirality operator, γ^5, does not commute with the $(3+1)$ dimensional Dirac Hamiltonian, Eq. (1.1), because of the mass term.

[3]The helicity operator commutes with Eq. (1.2) in the sense that the Weyl equations are regrouped into a 4×4 matrix equation.

Therefore, if a massive particle is found to be in a left- or right chiral state, its chirality will change over time. Hence, neither helicity nor chirality is a definite characteristic of massive Dirac particles.

The 2-spinors appearing in the Weyl equations (1.2) are left- and right-helical, because they are eigenspinors of $\hat{\mathbf{k}} \cdot \boldsymbol{\sigma}$, which is the helicity operator in the 2-spinor subspace. From these, one can form 4-spinors that contain purely left- or right-helical components as $\psi^L = \left(\begin{smallmatrix} \psi_L \\ 0 \end{smallmatrix}\right)$ and $\psi^R = \left(\begin{smallmatrix} 0 \\ \psi_R \end{smallmatrix}\right)$. These 4-spinors are simultaneously eigenspinors of the helicity operator, $\boldsymbol{\Sigma} \cdot \hat{\mathbf{k}} \psi^L = -\psi^L$ and $\boldsymbol{\Sigma} \cdot \hat{\mathbf{k}} \psi^R = +\psi^R$, and eigenspinors of the chirality operator, $\gamma^5 \psi^L = -\psi^L$ and $\gamma^5 \psi^R = +\psi^R$. Hence, for massless particles in $(3+1)$ dimensions helicity and chirality coincide, and therefore is handedness for Weyl fermions unambiguous. A Weyl fermion with a given handedness $\chi = \pm 1$ remains with that handedness for all time according to all observers. Since 4-spinors ψ^L and ψ^R exist for both positive and negative energy, they are degenerate states.

To see how a Weyl fermion can appear as an emergent particle in low-energy physics, one needs only an old pillar of condensed matter physics: band theory [34]. Many properties of crystalline solids can be understood simply by their energy bands. With translational invariance, the crystal momentum $\mathbf{k}$ is a good quantum number and the energy bands are functions of $\mathbf{k}$ in the Brillouin zone. The energy bands specify the energies that electrons in the crystal are allowed to take. The non-interacting ground state is obtained by minimizing the kinetic energy when filling up unoccu-

pied states from the lowest energy with electrons in compliance with Pauli's exclusion principle. The energy corresponding to the last placed electron, denoted as the Fermi level or chemical potential, demarcates all the occupied from unoccupied states. Depending on the material, there may be an energy gap Δ between the highest occupied and lowest unoccupied states.

With this simple picture of a ground state, one can classify certain crystals. If the Fermi level lies within a large energy gap, $\Delta \gg k_B T$ (T room temperature), an electron in an occupied state cannot repopulate an unoccupied state when applying a small external electric field. Consequently, the system does not respond to an external electric field, and the crystal is referred to as an insulator. On the other hand, a metal has a high mobility of electrons. Here, an unoccupied state can easily be populated by an electron from a filled state when applying a small electric field allowing current to flow. This means that the Fermi level has to be within a band. In-between these two types of crystals is the semiconductor. While it has a band gap, it is far smaller than for an insulator and typically $\Delta \lesssim k_B T$. A few electrons can be thermally excited into the conduction band, and these electrons can move freely carrying a small amount of current. When this gap closes, i.e., $\Delta = 0$, the Fermi level is within a band like in a metal, but the density of states is vanishing near the Fermi level in contrast to a metal. A Weyl node/point is exactly such a case.

A Weyl node is formed when two non-degenerate, linearly dispersing valence and conduction bands cross at a single momentum, say $\mathbf{k} = \mathbf{k}_0$, which is a degenerate

point. Figure 1.3 illustrates these basic band structures. If the chemical potential $\mu > 0$ lies above the Weyl node, the Weyl semimetal (a material containing multiple Weyl nodes, which will be introduced in next subchapter) has metallic character. To this day, it remains a scholarly debate [35, 36, 37, 38, 39, 40], whether Weyl nodes can be aligned exactly at the chemical potential.

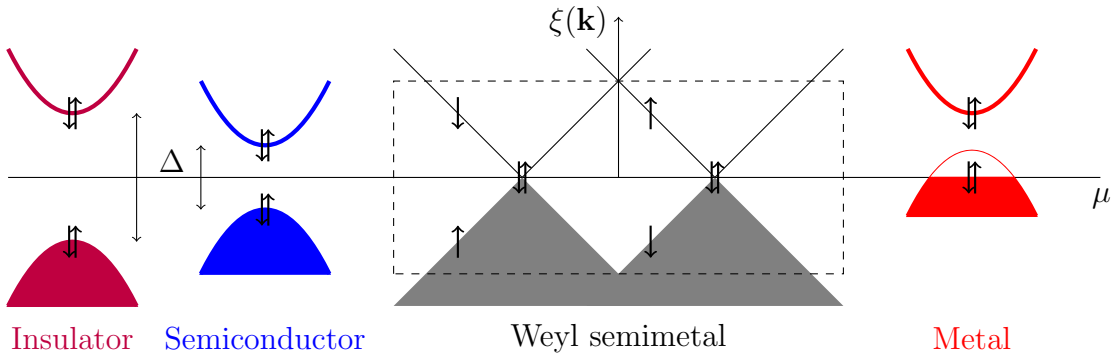

Figure 1.3: A simple classification of crystalline solids. Any real material has a multi-band structure, but here only the highest occupied and lowest unoccupied bands are illustrated. A minimal Weyl semimetal is illustrated with two nodes of opposite chirality separated in momentum space.

In a generic two-band subspace, two scenarios can occur: either bands cross or they do not. In the latter case, the energy spectrum is gapped and the mechanism behind it is known as level repulsion of a two state system. In the former case, the spectrum is gapless and bands are nondegenerate except at the node. One may ask, how likely is it that this scenario occurs without restrictions from symmetry or Hermiticity of the Hamiltonian? The answer is that such an accidental degeneracy [41, 42], can occur by tuning three parameters of the two state Hamiltonian. In band theory, one may regard the crystal momenta as parameters, the number of

which equals the dimension of momentum space. Therefore, in 1 and 2-dimensions, an accidental degeneracy is unlikely to occur[4], whereas in 3-dimensions it can. By expanding the two-state system to linear order in $\mathbf{k}$ near the Weyl node, one obtains a form of the Weyl Hamiltonian,

$$H = \epsilon(\mathbf{k})\sigma^0 + \chi v_{\mathrm{F}} \boldsymbol{\sigma} \cdot (\mathbf{k} - \mathbf{k}_0)\,. \tag{1.5}$$

Here, $\boldsymbol{\sigma}$ is a vector of the three Pauli matrices corresponding to pseudospin, σ^0 is the identity matrix, and $\chi = \pm 1$ is the chirality. Due to the resemblance of the second term in Eq. (1.5) with the relativistic Weyl equation (1.2), this Hamiltonian deserves its name. The immediate difference is that the speed of light c has been replaced by the Fermi velocity v_{F} and a new term, $\epsilon(\mathbf{k})$, is allowed which acts as a momentum dependent chemical potential. A condensed matter Weyl fermion has two internal states, which we refer to as pseudospin. It can either be real spin, indexing sublattices or other degrees of freedom. Since Eq. (1.5) is expanded in all Pauli matrices and the identity matrix, no local perturbation can gap out its spectrum. The most a local perturbation can do is to change the position of the node in energy and momentum space or distort the isotropic spectrum, $\boldsymbol{\sigma} \cdot (\mathbf{k} - \mathbf{k}_0)$, to an anisotropic form $\sigma_i \lambda_{ij} (\mathbf{k} - \mathbf{k}_0)_j$, where λ is a real 3×3 matrix. Here, Einstein's summation convention is used throughout the dissertation unless otherwise mentioned explicitly.

[4]By additional tuning parameters or symmetries, a degeneracy can occur. For example, graphene.

1.3 Weyl Semimetals

The stability of the Weyl node, Eq. (1.5), alluded to above has a topological origin [3, 43]. A Weyl node corresponding to Bloch band n can be considered as a magnetic monopole in momentum space with a topological charge density $\rho_n(\mathbf{k}) = \chi 2\pi\delta(\mathbf{k})$. Drawing a Gauss sphere in momentum space surrounding the node, one will find it having a topological charge $Q_n = \chi 2\pi$. Importantly, this is a quantized number, the sign of which is determined by the chirality of the node. Hence, a single Weyl node cannot disappear spontaneously, but only by annihilating with a node of opposite chirality. From this, one can understand the topological stability of a Weyl semimetal. Weyl nodes may occur at any energy formed between two bands in a multi-band structure, but their total topological charge has to be zero (see argument below). The total charge is found by enclosing the entire first Brillouin zone by a Gauss box and calculating the total topological flux through it. On the other hand, due to periodicity of the Brillouin zone, one can deform this Gauss box to enclose a volume with no topological charge in it, see illustration in Fig. 1.4. Consequently, the total topological charge, i.e., the sum of chiralities of nodes at the chemical potential, is zero. This expresses a topological sum-rule for a Weyl semimetal.

The above topological sum rule expresses the solid state physics version of the fermion doubling theorem [7, 8], which in other words says that Weyl nodes have to come in pairs of each chirality. Furthermore, a Weyl semimetal is topologically protected if nodes are separated in momentum space. The Weyl semimetal is therefore

a topological semimetal, contrary to a non-topological/ordinary semimetal. Together with symmetry considerations, this helps us to classify different Weyl semimetal phases. Analogous to Eq. (1.5), we define a prototype node at $\mathbf{k}_0$ with a given chirality χ as $H(\mathbf{k}) = \chi v_{\mathrm{F}} \boldsymbol{\sigma} \cdot (\mathbf{k} - \mathbf{k}_0)$, as one may ignore the term $\epsilon(\mathbf{k})$ for topological considerations. Inversion symmetry operation takes $\mathbf{k} \to -\mathbf{k}$ and $\boldsymbol{\sigma} \to \boldsymbol{\sigma}$, thus its image node will have the form $H(\mathbf{k}) = -\chi v_{\mathrm{F}} \boldsymbol{\sigma} \cdot (\mathbf{k} + \mathbf{k}_0)$ located at $\mathbf{k} = -\mathbf{k}_0$. Hence, the minimum number of nodes for an inversion invariant Weyl semimetal is two with opposite chirality. Similarly, time-reversal operation takes $\mathbf{k} \to -\mathbf{k}$ and $\boldsymbol{\sigma} \to -\boldsymbol{\sigma}$, thus the image node will have the form $H(\mathbf{k}) = +\chi v_{\mathrm{F}} \boldsymbol{\sigma} \cdot (\mathbf{k} + \mathbf{k}_0)$ located at $\mathbf{k} = -\mathbf{k}_0$. As the two nodes have the same chirality, the total sum of these is not zero, which it should be according to the sum-rule. But, a zero sum can be achieved by adding two nodes of opposite chirality. Hence, the minimum number of nodes for a time-reversal invariant Weyl semimetal is four, with two nodes of $\chi = +1$ chirality and two nodes of $\chi = -1$ chirality. From this follows that for a system invariant under both time-reversal and inversion symmetry, any node would have to be superimposed with a node of the opposite chirality, which is no longer a Weyl semimetal with only two bands crossing. Furthermore, a time-reversal invariant Weyl semimetal thus has to break inversion symmetry and vice versa. Lastly, if the system does not respect any symmetry, then Weyl nodes can be anywhere in momentum space with an even number of left- and right-handed chiralities.

In 2015, Weyl semimetals in crystalline solids were experimentally observed [13,

16, 17] in materials whose electronic excitations have a strong coupling between spin and orbital degrees of freedom and belonging to the class of time-reversal invariant, inversion symmetry-breaking, Weyl semimetals. While many Weyl semimetals of the time-reversal invariant class have been reliably identified, unambiguous experimental confirmation of Weyl semimetals belonging to the inversion invariant class is still a challenging task. Only a few materials [44, 45, 46], among many candidates, are experimentally confirmed to be Weyl semimetals.

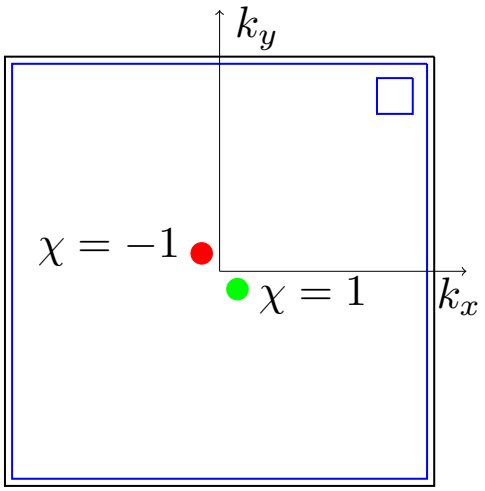

Figure 1.4: Brillouin zone in the $k_x k_y$-plane. A Gauss box (blue line) enclosing the entire first Brillouin zone (black line), and a Gauss box (small blue square) enclosing a region with no Weyl nodes are drawn. Two Weyl nodes with chirality $\chi = 1$ and -1 are indicated by a red and green dot, respectively.

We have seen in Eq. (1.5) that a term $\epsilon(\mathbf{k})$ independent of pseudospin is allowed in addition to the relativistic version of the Weyl equation. From the above classification of Weyl semimetals, we know that Weyl nodes will generally not be at high symmetry points of the Brillouin zone edge, and definitely not at time-reversal invariant momenta (TRIM) of the Brillouin zone. Only at these special points [47] will $\epsilon(\mathbf{k}) = 0$, generally. Hence, in generic Weyl semimetal materials, it is expected that

$\epsilon(\mathbf{k}) = \epsilon_0 + \mathbf{v} \cdot (\mathbf{k} - \mathbf{k}_0)$ with ϵ_0, a constant energy off-set, and $\mathbf{v}$, a vector of three parameters. In chapter 3 we will return to a discussion about such a term.

This chapters made it clear that a Weyl semimetal is a special kind of semimetal, a topological one. As with any topological state of matter, this manifests itself in various remarkable ways, in particular, in topological surface states and responses to applied electromagnetic fields, see Refs. [48, 10] for review. Of type-I Weyl semimetals, most of these exotic phenomena have the strongest and clearest signatures when: the nodes are pinned at (or near) the Fermi energy, the term $\epsilon(\mathbf{k})$ of Eq. (1.5) is negligible, and no trivial bands near the Fermi level exist. A Weyl semimetal with these bulk properties is referred to as "ideal", see Fig. 1.3. To the author's knowledge, only one material [49] has been discovered with a single pair of Weyl nodes at the Fermi level without any coexisting trivial bands. This material has a term $\epsilon(\mathbf{k}) = \mathbf{v} \cdot (\mathbf{k} - \mathbf{k}_0)$ independent of pseudospin. However, Ref. [35] predicts a fully ideal[5] Weyl semimental in the HgTe-class of materials.

1.3.1 Inversion Invariant Weyl Semimetal Model

Now, we focus on the protected topological surface states, which are most easily explained in the context of a Weyl semimetal model, providing us some intuition about how Weyl semimetals occur and their relation to other states of matter. A

[5] In photonic crystals and topological circuits, fully ideal type-I Weyl nodes have been observed.

model[6] of a Topological Insulator (TI) and Normal Insulator (NI) heterostructure [50, 51, 52] will be used. Later, in Ch. 5, when illustrating the coupling of a neutron to Weyl fermion, we will use a toy model of this more realistic model.

A topological insulator thin-film Hamiltonian $H_{TI} = v_{\mathrm{F}}\tau^z(\hat{\mathbf{z}} \times \boldsymbol{\sigma}) \cdot \mathbf{k}$ has two-dimensional gapless surface states on each surface designated by τ^z, where $\boldsymbol{\sigma}$ is a vector of Pauli spin matrices. In a thin-film, the surfaces are hybridized by $H_{\Delta_S} = \Delta_S\tau^x$. One can gap out these surface states [53, 54] by doping with magnetic impurities $H_Z = m\sigma^z$. In conclusion, the entire Hamiltonian is $H_{slab} = H_{TI} + H_{\Delta_S} + H_Z$ which can be written in a block diagonal form $H_{slab} = v_{\mathrm{F}}(\hat{\mathbf{z}} \times \boldsymbol{\sigma}) \cdot \mathbf{k} + m_r\sigma^z$, where mass m_r depends on m and Δ_S with each block indexed by $r = \pm 1$. Figure 1.5 illustrates these gapped 2D Dirac fermions on the edges of the slab after magnetization. From this, one constructs a finite size TI-NI heterostructure by interlacing NI slabs with TI slabs, where d is the length of the superlattice in the z-direction, see Fig. 1.5. This creates a Hamiltonian $H_{TI-NI} = v_{\mathrm{F}}(\hat{\mathbf{z}} \times \boldsymbol{\sigma}) \cdot \mathbf{k} + M(k_z)\sigma^z$ where a new mass term $M(k_z)$ is considered a function of k_z for a given m, Δ_S and Δ_D, where Δ_D is the coupling between two neighbor TI slabs.

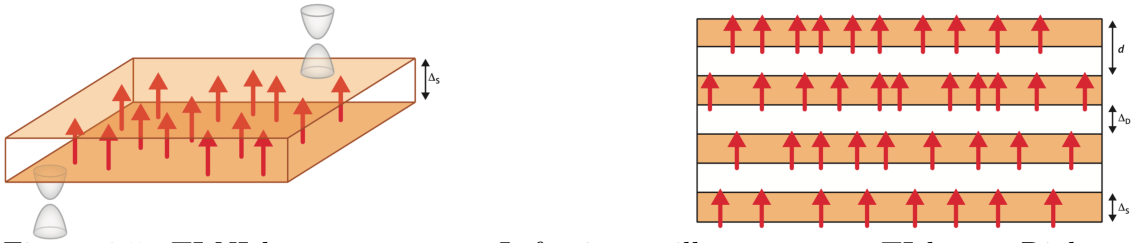

Figure 1.5: TI-NI heterostructure. Left picture illustrates one TI layer. Right picture illustrates many TI-NI layers. From Ref. [52].

[6] To date, no Weyl semimetal material has been found that realizes this model.

The evolution of the Weyl semimetal phase diagram, see Fig. 1.6, can be understood as follows. In the time-reversal and inversion symmetric limit, $m = 0$, the two Weyl nodes are superimposed and form a double degenerate linear spectrum of the massless Dirac Eq. (1.1), which is a phase transition point, $\Delta_S/\Delta_S = 1$, between a normal and topological insulator [4, 5]. On increasing m from zero to $m = |\Delta_S - \Delta_D|$, the Dirac node splits into nondegenerate bands forming separated Weyl nodes at $\mathbf{k} = (0, 0, \pm k_0)$. As m is increased further, the two nodes keep moving along k_z and eventually meet for $m = |\Delta_S + \Delta_D|$ to annihilate and leave the spectrum fully gapped.

Figure 1.6: Phase diagram of TI-NI heterostructure. Left diagram is with no doping. Right diagram is with doping. From Ref. [51].

It is convenient to regard the bulk Hamiltonian as a gapped 2D Dirac Hamiltonian with a mass $M(k_z)$ for a fixed k_z, i.e., $H_{k_z}(k_x, k_y)$. When varying the parameter k_z, the sign of the mass changes across $k_z = \pm k_0$, at the Weyl nodes where the gap closes, i.e., $M(\pm k_0) = 0$. It is well known [55, 56, 57] that such a point marks a quantum Hall phase transition where the Hall conductance defined in the 2D $k_x k_y$-plane, $\sigma_{xy}(k_z) = \frac{1}{2}\frac{e^2}{h} sign[M(k_z)]$, jumps $\Delta\sigma_{xy} = \sigma_{xy}(M > 0) - \sigma_{xy}(M < 0) = \frac{e^2}{h}$. In a continuum model, one can only calculate the change in the Hall conductance.

However, one can also find the sign if the Hall conductance at a k_z before this new state is known. In Fig 1.7, the mass function $M(k_z)$ is illustrated for the present case $m \neq 0$, but also for the reference state, i.e., the time-reversal symmetric phase with $m = 0$. Since the reference state is a 2D insulator, either a normal or topological one depending on ratio Δ_S/Δ_D, (see phase diagram Fig. 1.6), the sign of its mass is constant (here negative) for all k_z. We now know the regions of k_z, where the mass did not change sign in-between $m = 0$ to $m \neq 0$, are trivial with no Hall conductivity. Likewise, the remaining regions of k_z are non-trivial with a nonzero Hall conductivity, since the mass did change sign in-between $m = 0$ to $m \neq 0$.

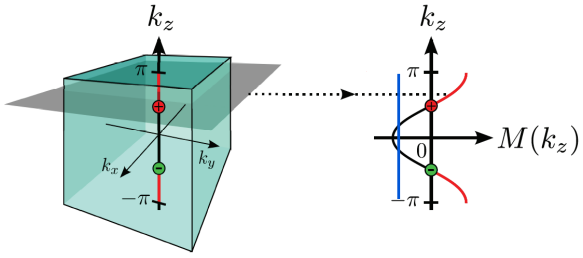

Figure 1.7: Weyl semimetal as a 2D Dirac Hamilton $H_{k_z}(k_x, k_y)$ with mass $M(k_z)$. The mass corresponding to no doping (blue line) differs from a doped one (red to black curve). Adapted from Ref. [58].

Each Hall layer / Fermi arc state (a chiral edge state) contributes a Hall conductivity of $\sigma_{xy}(k_z) = \frac{e^2}{2\pi h}$, and thus the total Hall conductivity is $\sigma_{xy} = \frac{e^2}{2\pi h} 2k_0$. Therefore, a Weyl semimetal can be viewed as a phase of $2k_0$ (length of Fermi arc) stacked 2D Chern insulators[7]. Furthermore, the anomalous Hall conductivity of a Weyl semimetal is proportional to the separation $2k_0$ between the nodes. If disorder is included (but interactions ignored) the Weyl semimetal persists being a metal and not an insulator. Hence, a Weyl semimetal is *not* a Hall insulator, but an un-

[7] A Chern insulator [59] is a 2D insulator but has a Hall conductivity without a magnetic field.

usual metallic state characterized by a finite nonquantized quantum anomalous Hall conductivity.

When the doping m reaches maximum and beyond $m \geq |\Delta_S + \Delta_D|$, the two nodes meet (spanning the Fermi arc from Brillouin zone edge to edge) and annihilate each other, and the Weyl semimetal makes a phase transition into a quantum anomalous Hall insulator phase, which is characterized by Hall conductivity $\sigma_{xy}|_{k_0=\pi/d} = \frac{e^2}{hd}$, i.e., is quantized $\frac{e^2}{h}$ per TI layer d, see Fig. 1.8.

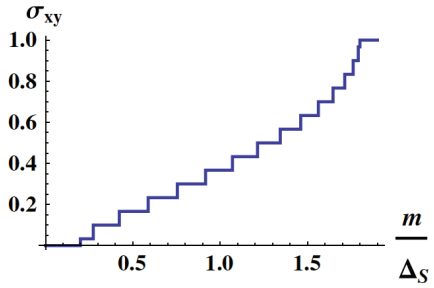

Figure 1.8: Hall conductivity σ_{xy} per $\frac{e^2}{h}$ as function of m/Δ_S. From Ref. [50].

The planes in momentum space with a normal direction parallel to the k_z axis are trivial, since the bulk Weyl nodes contribute a zero total topological flux through these planes. On the remaining 2 planes, topological protected surface states, called Fermi arcs [6, 60], exist and in general form open arcs on the surface Brillouin zones for the upper and lower surfaces, see Fig. 1.9. In other words, the Fermi arc on one either surface does not form a closed loop as does a Fermi surface conventionally[8]. Hence, this Fermi arc could *not* have occurred in a 2D system nor in a gapped system. As the bulk is half-filled right to the energy of the Weyl nodes, the bulk Fermi surface

[8]They are defined as the intersection of the dispersion and chemical potential.

is just two points which remains two points in the surface Brillouin zone after being projected onto the surface. In this case, the Fermi arcs (the constant zero energy contour), end at the surface Brillouin zone projections of the bulk Weyl nodes of opposite chiralities. Another interesting feature is that surface states delocalize into the bulk $\sim e^{-z|k_z-k_0|} \to 1$ until the Weyl node projection, $k_z = k_0$, at which the surface states are merged to bulk bands and no longer well-defined.

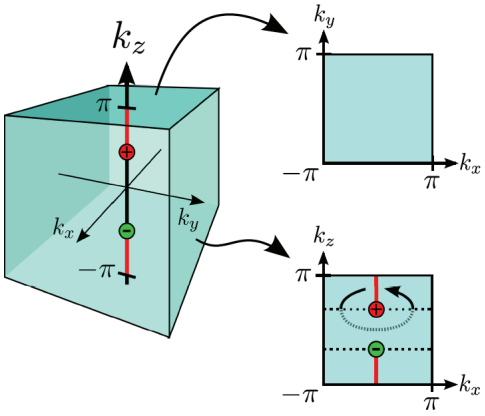

Figure 1.9: Total Fermi surface at half filled bands: both bulk (red and green point) and surface arc (red line) Fermi surfaces. From Ref. [58].

Chapter 2

Introduction to Neutron Scattering Off Weyl Nodes

Except for establishing magnetic structure [61, 62, 63], spin dynamics [64], and probing magnon excitations [27, 65], neutron scattering has by and large been absent in revealing the physics in topological semimetals [10, 48]. Weyl semimetals, however, are characterized by the property that their bulk excitations are spin-momentum locked, meaning that an excitation's velocity is correlated with the orientation of its spin, which is characterized by the chirality. The state of positive or negative chirality can be thought classically as spin parallel or antiparallel with momentum. The magnetic property of Weyl excitations in momentum space indicates that inelastic neutron scattering could measure such a correlation as it is a probe well-suited for measuring magnetic properties of excitations, since a neutron interacts weakly with

matter via a magnetic dipole interaction besides short-ranged forces.

The basic idea behind an inelastic neutron scattering experiment on Weyl semimetals, is that as a neutron scatters from the system, it excites an electron from a state below the Fermi energy to one above. The chance of the electron's velocity being deflected in a given direction depends on the angle between this direction and the initial and final spins of the neutron (which in principle can be controlled experimentally). If this can be seen in an experiment, it would be a sign of spin-momentum locking and thereby a signature of Weyl nodes.

Inelastic neutron scattering would provide information that other experimental techniques cannot obtain. For example, it would go beyond angle-resolved photoemission spectroscopy in being able to resolve all three components of momenta and so would be able to probe spin-momentum locking more cleanly. Inelastic neutron scattering would correctly distinguish a Weyl semimetal from a narrow gap semiconductor because the spin-momentum locking does not occur in the latter (at least not at low energies).

However, it has long been known, that inelastic neutron scattering is a technique that has severe difficulties probing electronic excitations due to kinematic restrictions, form factor, and low density of states at the Fermi level. For normal metallic systems, the cross-section intensity was predicted [66] to be as low as[1] $10^{-4} - 10^{-3}$ mb/meV sr f.u.. At first glance, the prospects of probing excitations

[1]Here, b denotes a barn with unit of meter squared, eV denotes an electron volt with unit of joule, sr denotes a steradian which is dimensionless, and f.u. denotes a formula unit which is dimensionless.

in Weyl semimetals seem worse, since the cross-section should be limited by the small density of states at a Weyl point. We will show that the coupling between neutrons and Weyl fermions has a contribution in addition to the usual form factor, which can be large enough to compensate for the low density of states. The strength of cross-section may therefore be large enough to be experimentally possible.

Besides this practical/experimental concern we will encounter a plethora of conceptual issues relating to the prospects of neutrons resolving any properties of Weyl fermions. These come in two forms. First, a neutron scattering event creates a single particle-hole Weyl pair. However, the possible excitations form a particle-hole pair continuum in their energies with respect to a given neutron momentum transfer. Hence, the neutron response receives contributions from a whole particle-hole continuum. However, only the neutron momentum transfer is known, but this can result from many different combinations of momenta of the excited particle and hole, each of which corresponds to a different change in the neutron spin. Second, a neutron interacts with Weyl excitation's pseudospin because of the magnetic field of its magnetic moment. However, pseudospin is not directly related to real spin. The coupling of neutron to pseudospin is therefore determined by specific material parameters, which are *a priori* unknown. Thus, at first, it seems impossible that neutron scattering could be used to identify Weyl fermions. On the contrary, our theory shows that neutron scattering can detect spin-momentum locking of Weyl excitations in the easiest (fully unpolarized) experiment. Furthermore, the scattering region of the cross-section has

a discontinuous edge, which is a strong signature of scattering between Weyl nodes transformed into Lorentz invariant form. This allows measurement of the anisotropic Weyl nodes' dispersion. It is surprising that despite pseudospin not relating to real spin in a definite way, there is still an analogue of spin-conservation in the interaction between the neutron and the Weyl fermion. This has the remarkable consequence that the chirality, or topological charge, of inversion symmetric nodes is measurable independently of the in general unknown and arbitrary coupling parameters.

Besides the primary problem discussed here of how to deduce the properties of Weyl excitations from neutron scattering, the detailed analysis reveals that certain elements discovered could give new information about Weyl semimetals. For example, the coupling of a Weyl fermion to magnetic fields (not necessarily induced by a neutron) is very different from the bare coupling to electrons. Without restrictions from symmetry, the coupling can have 16 independent parameters and, more importantly, be larger than the ordinary Bohr magneton. Furthermore, the analysis suggests that highly unusual types of particle-hole excitations could be generated by a neutron scattering event, the pair of which would, in addition, be allowed to interact through an electric dipole-dipole interaction, which free electrons can not do.

This dissertation investigates theoretically inelastic neutron scattering off a type-I Weyl semimetal. To make the discussion general, we will consider Weyl nodes with realistic anisotropy. The rest of this chapter is a first encounter with inelastic neu-

tron scattering off ideal/isotropic Weyl nodes. Chapters, 3, 4, and 5, construct the neutron scattering cross-section measured in a hypothetical experiment on realistic anisotropic Weyl nodes. Once having derived this, chapter 6 will exclusively focus on its interpretation. It turns out to require non-trivial transformations of the detected response in order to measure the dispersion of bulk Weyl excitations, their characteristic spin-momentum locking, and associated chirality.

2.1 Neutron Scattering Off Ideal Weyl Nodes

Let us begin considering the simplest Weyl semimetal introduced in Sec. 1.3, that is one with two Weyl nodes at momenta $\mathbf{k}_{0,1}$ and $\mathbf{k}_{0,2}$. Furthermore, let us assume that the Hamiltonians near these are on the idealized form,

$$H_{0,i}(\mathbf{k}) = \chi_i v_{\mathrm{F}} \boldsymbol{\sigma} \cdot (\mathbf{k} - \mathbf{k}_{0,i}) \ . \tag{2.1}$$

Here, v_{F} is the velocity of Weyl particles and $\chi_i = \pm 1$ is their chirality which we will be interested in measuring. The vector of pseudospin Pauli matrices is $\boldsymbol{\sigma}$. It is convenient to introduce $\mathbf{p} = \mathbf{k} - \mathbf{k}_{0,i}$, the momentum measured relative to the Weyl point, because the Weyl equation has two solutions corresponding to the conduction and valence band, labeled by $\eta = \pm 1$, with energy $\xi_\eta^{\mathrm{w}}(\mathbf{p}) = \eta v_{\mathrm{F}} |\mathbf{p}|$. The eigenfunctions of Eq. (2.1) are $\psi_{i,\eta}(\mathbf{r}) = e^{i\mathbf{k}\cdot\mathbf{r}/\hbar} u_{\chi_i \eta}(\hat{\mathbf{p}})$, where $u_{\chi_i \eta}(\hat{\mathbf{p}})$ represents a 2-component pseudospinor depending on momentum $\hat{\mathbf{p}} = (\sin\theta_{\mathbf{p}} \cos\phi_{\mathbf{p}}, \sin\theta_{\mathbf{p}} \sin\phi_{\mathbf{p}}, \cos\theta_{\mathbf{p}})$ relative

to the node as,

$$u_+(\hat{\mathbf{p}}) = \begin{pmatrix} \cos\theta_{\mathbf{p}}/2 \\ e^{i\phi_{\mathbf{p}}}\sin\theta_{\mathbf{p}}/2 \end{pmatrix} \quad , \quad u_-(\hat{\mathbf{p}}) = \begin{pmatrix} e^{-i\phi_{\mathbf{p}}}\sin\theta_{\mathbf{p}}/2 \\ -\cos\theta_{\mathbf{p}}/2 \end{pmatrix} . \tag{2.2}$$

The average of pseudospin $\boldsymbol{\sigma}$ in $u_{\chi_i\eta}(\hat{\mathbf{p}})$ is pointing either parallel or antiparallel to the momentum $\hat{\mathbf{p}}$, according to $\chi_i\eta = 1$ and $\chi_i\eta = -1$, as illustrated in Fig. 1.2.

If the chemical potential lies at the Weyl nodes, a neutron with initial momentum $\mathbf{q}_i$ can scatter a Weyl fermion with momentum $\mathbf{k}_i$ below the Fermi energy to a state above the Fermi energy with momentum $\mathbf{k}_f$. In such a scattering event, two kinds of excitations are possible: *intra*node and *inter*node excitations. In intranode scattering, the neutron scatters an electron in one node to a state within the same node, see Fig. 2.1 illustrated by the M^0 transition. In the case of internode scattering, the neutron scatters an electron from one Weyl node to another node, see Fig. 2.1, illustrated by the two transitions $\mathrm{M}^{\pm}$. In any case, the neutron transfers energy $\hbar\omega$ and momentum $\mathbf{q} = \mathbf{q}_i - \mathbf{q}_f$ to the Weyl semimetal with, accordingly, a change in internal energy $\Delta\xi^{\mathrm{w}}$ and momentum $\Delta\mathbf{k} = \mathbf{k}_f - \mathbf{k}_i$ due to energy and momentum conservation in the scattering event. In this dissertation only internode scattering will be discussed. Intranode scattering is discussed in Refs. [28, 67].

Such a scattering process is the result of a neutron interacting with the electronic system. Several descriptions exist and a discussion can be found in Refs. [68, 69]. Here, we find it useful to begin with a description of the process as the vector poten-

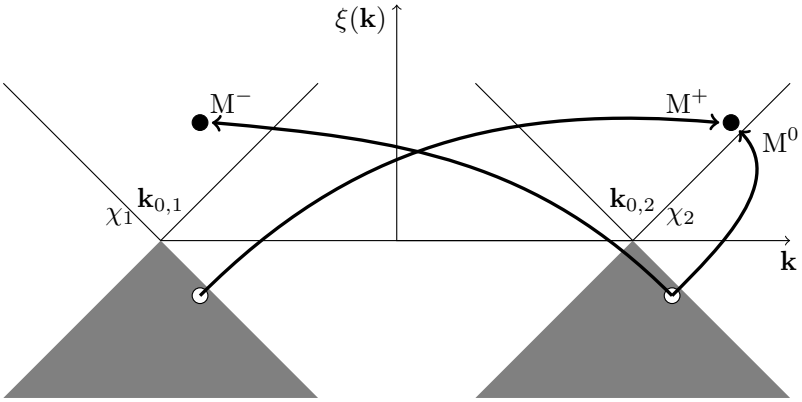

Figure 2.1: Low energy region of two isotropic Weyl nodes located at $\mathbf{k}_{0,2} = -\mathbf{k}_{0,1}$ with chirality χ_2 and χ_1, respectively. At zero temperature the valence band is filled (grey). A possible internode transition is indicated by M^0. The two internode transitions are indicated by $\mathrm{M}^{\pm}$.

tial[2] operator $\mathbf{A}(\mathbf{r})$ of the neutron's magnetic moment interacting with the currents of the electronic system. As the neutron probe the Weyl semimetal bulk, we can safely ignore possible scattering contributions from the Fermi arcs (see Sec. 1.3.1). In a neutron experiment, the detector's counting rate per incoming neutron flux, called the differential cross-section, is proportional to the dynamic structure factor, i.e., heuristically,

$$\frac{\mathrm{d}^2\sigma(\mathbf{q},\omega)}{\mathrm{d}\Omega \mathrm{d}E_f} \propto S_{l\,m}(\mathbf{q},\omega)\,. \tag{2.3}$$

This is the frequency and momentum Fourier transform of the scattering function $S_{l\,m}(\mathbf{r},t) = \langle J_l(\mathbf{r},t) J_m(\mathbf{0},0)\rangle_0$, which is a correlator of the electronic transition current

[2]The vector potential $\mathbf{A}(\mathbf{r}-\mathbf{r}_\mathrm{n}) = (\mu_0/4\pi)\boldsymbol{\mu}_\mathrm{n} \times (\mathbf{r}-\mathbf{r}_\mathrm{n}/|\mathbf{r}-\mathbf{r}_\mathrm{n}|^3)$ at spacepoint $\mathbf{r}$ induced by a neutron magnetic moment operator $\boldsymbol{\mu}_\mathrm{n} = \gamma\frac{\hbar}{2}\boldsymbol{\tau}$ at $\mathbf{r}_\mathrm{n}$, where $\gamma = \frac{g\mu_\mathrm{n}}{\hbar}$ with nuclear magneton magnetic moment $\mu_\mathrm{n} = \frac{e\hbar}{2m_\mathrm{n}}$, neutron g-factor g. The permeability of free space is μ_0.

operators. The ultimate aim of Ch. 3 is to determine $S_{l\,m}(\mathbf{q},\omega)$. To do so, we will need to find the current operator that describes the electronic transitions generated in the scattering event. In Sec. 3.2 we will return to this pursuit. Nevertheless, the response is overall determined by energy and momentum constraints of the scattering event, which in turn are dictated by the dispersion of the bulk excitations. We will see in Sec. 3.1 that dispersions in realistic Weyl semimetals are most likely not described by Eq. 2.1. However, such an idealized Weyl semimetal still gives a good intuition of the observed cross-section, which we will therefore content ourselves with for the rest of this chapter.

The internode scattering process has momentum conservation represented by a factor $\delta^3(\mathbf{q}-\Delta\mathbf{k}) = \delta^3(\mathbf{p}-\boldsymbol{\Delta})$, where it is convenient to introduce new variables $\boldsymbol{\Delta}$ and $\mathbf{p}$. The first is defined by $\boldsymbol{\Delta} = \Delta\mathbf{k}_0 - \mathbf{q}$, i.e., the deviation between the transferred momentum and the vector connecting the exact positions of the nodes $\Delta\mathbf{k}_0 = \mathbf{k}_{0,f} - \mathbf{k}_{0,i}$. The second is defined by $\mathbf{p} = \mathbf{p}_f - \mathbf{p}_i$, where the variables $\mathbf{p}_i, \mathbf{p}_f$ are the parts of the momenta that appear in the Weyl equation, i.e., the deviation of each momentum from the corresponding Weyl point. These momenta may be regarded as a sort of "kinetic momenta" because they determine in which direction the particle moves and its spin state, while $\mathbf{k}_{0,1}$ and $\mathbf{k}_{0,2}$ are just constant offsets.

The change in energy of the electron, due to scattering from a negative energy state at the first node to a positive energy state at the second node, is $\Delta\xi^{\mathrm{w}} = v_{\mathrm{F}}|\mathbf{p}_f| - (-v_{\mathrm{F}})|\mathbf{p}_i|$, so energy conservation is described by $\delta[\hbar\omega - v_{\mathrm{F}}(|\mathbf{p}_f| + |\mathbf{p}_i|)]$.

Graphically, the transferred "kinetic momentum" $-\mathbf{\Delta}$ is represented by a vector connecting the end-points of $\mathbf{p}_f$ and $\mathbf{p}_i$ and the energy is proportional to the sum of their lengths. Thus, by using the triangle inequality then,

$$\hbar\omega \geq v_{\mathrm{F}}|\mathbf{\Delta}|\,, \tag{2.4}$$

which is the region of nonzero density of states of Weyl excitations (see Sec. 6.1).

The most basic observation using neutron scattering is the region of $\mathbf{q},\omega$-space in which the fully unpolarized cross-section is nonzero. The shape of this region is determined by the region of density of states of Weyl excitations, Eq. (2.4), with an intensity modulation due to the matrix elements for creating a particle-hole Weyl pair. Suppose one plots the scattering cross-section at a fixed energy transfer. Then the above inequality, Eq. (2.4), says that the scattering cross-section is nonzero only inside of a sphere; the sphere is expected to appear with a strong relief as the cross-section jumps sharply from zero at its surface. Clearly identifying this region from the measured cross-section is contingent on the intensity of the Weyl fermion scattering channel being sufficiently large compared to the intensity of background channels, which will inevitably be present in a real experiment. To proceed developing the theory, we assume that the Weyl fermion scattering channel has been cleanly separated from background channels. Section 6.1 discusses the strength of the Weyl fermion

scattering channel and possible background channels. Furthermore, suggestions about how isolate the Weyl fermion scattering intensity from background intensity will be presented. In an actual experiment, if one plots the cross-section at a fixed $\hbar\omega$ as a function of the momentum transfer $\mathbf{q}$, one will see two spheres of radii $\hbar\omega/v_{\mathrm{F}}$ centered at $\pm 2\mathbf{k}_0$ as in Fig. 2.2, which correspond to transitions (see Fig. 2.1) from the first Weyl node to the second, or vice versa, which we call $\mathrm{M}^{\pm}$ transitions. The $\mathrm{M}^{\pm}$ transitions are displaced in momentum because the physical momentum differs from $\mathbf{p}$ by offsets $\Delta\mathbf{k}_0 = \pm 2\mathbf{k}_0$. The way the cross-section varies within these spheres is interesting to understand in detail because it is connected to spin-momentum locking (see Sec. 6.2). However, from just observing the spheres one can determine the Weyl node dispersion. By measuring the radius of a sphere as a function of transferred energy, one may deduce the Fermi velocity of the Weyl excitations. The linear relationship between the radius of a sphere and the transferred momentum reflects the linear dispersion of Weyl excitations.

The scattering cross-section, or structure factor $S_{lm}(\mathbf{q}, \omega)$, at a given momentum transfer $\mathbf{q}$ does not have a sharp peak at a single transferred energy $\hbar\omega$ (as one would have when exciting magnons), but instead shows a broad peak indicative of a continuum of energies of a particle-hole pair for a fixed momentum transfer $\mathbf{q}$. There are two ways to understand this: for each $\mathbf{\Delta}$ there are different ways to divide momentum between hole and particle because of $\mathbf{\Delta} = \mathbf{p}_f - \mathbf{p}_i$. This gives a range of energies $\Delta\xi^{\mathrm{w}}$ for each $\mathbf{\Delta}$. Alternatively, for a fixed energy $\hbar\omega = \Delta\xi^{\mathrm{w}}$ there is a range of $\mathbf{\Delta}$'s. The

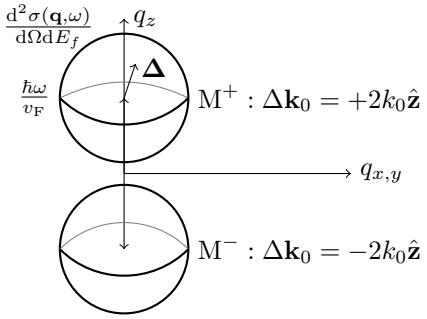

Figure 2.2: Region of nonzero scattering between two nodes at $\mathbf{k}_{0,2} = -\mathbf{k}_{0,1} = k_0\hat{\mathbf{z}}$. The cross-section as a function of momentum transfer $\mathbf{q}$ varies within spheres, $|\mathbf{\Delta}| \leq \hbar\omega/v_\mathrm{F}$, for nodes on form Eq. (2.1). For anisotropic nodes, Eq. (3.1), the nonzero regions would be ellipsoids centered on $\Delta\mathbf{k}_0$. Such a system can be reduced to an isotropic system (provided $\mathbf{v}_0^{(i)} = \mathbf{0}$) by applying a transformation $\mathcal{T}$ to reshape the regions into spheres $|\mathcal{T}\mathbf{\Delta}| \leq \hbar\omega/v_\mathrm{F}$.

latter is expressed by $\hbar\omega \geq v_\mathrm{F}|\mathbf{\Delta}|$ and illustrated in Fig. 2.2 by $\mathbf{\Delta}$ ranging within the spheres of radii $\hbar\omega/v_\mathrm{F}$.

We have already come to an important realization: a Weyl particle-hole continuum is generated in the scattering event, meaning that the response $S_{l\,m}(\mathbf{q},\omega)$ measured will sum up contributions from all the pairs in the continuum. From this consideration it thus seems doubtful that one is able to measure spin-momentum locking of excitations, and even more doubtful to measure their chirality. One may legitimately object that in the above analysis only the neutron momentum transfer $\mathbf{q}$ was controlled. Still, even if we controlled the maximum experimentally possible parameters, i.e., $\mathbf{q}$ and both incident and scattered neutron spin, a Weyl particle-hole continuum is generated in the scattering event, which means we still face the same issues mentioned. Later, we will see that the coupling of neutron to Weyl fermions is given by a

scourge of arbitrary coupling parameters, which mixes up the matrix elements from each particle-hole pair of the continuum contributing to the measured response. This poses the question: is a neutron spin-flip process accompanied by a corresponding spin-flip of a Weyl fermion? If indeed it is the case, that spin is not conserved in a scattering event, then the slightest prospect of measuring chirality seem precluded. Remarkably, it turns out that one can circumvent all of these obstacles. In Ch. 3, we will investigate, in detail, why all these obstacles occur and, in Ch. 6 how to circumvent them.

Chapter 3

Inelastic Neutron Scattering Off Anisotropic Weyl Nodes

In this chapter we ask, what is the theoretically expected cross-section in an inelastic neutron scattering experiment off Weyl semimetals? Section 3.1 begins with keeping the discussion as general as needed, but in Sec. 3.1.2 we restrict the Weyl nodes involved in a scattering event. We will soon realize that we need to change coordinates of the Weyl nodes, which are derived in Sec. 3.1.1. To derive the dynamical structure factor, we first need to derive the coupling of neutrons to Weyl nodes, which is done in Sec. 3.2. With all this in our hands, we turn to the actual derivation of the dynamic structure factor in Sec. 3.3. In chapter 4, all the knowledge gathered here is collected into a concise formulation of the inelastic neutron cross-section to be obtained in a measurement assuming background scattering channels having been

removed.

3.1 Isotropic vs. Physical Coordinates

In contrast to a relativistic description of Weyl fermions, a condensed matter Weyl semimetal manifestly breaks [70] Lorentz invariance, because nodes are separated in momentum space, and the i^{th} Weyl node expanded to linear order in the momentum has the form,

$$H_{0,i}(\mathbf{k}) \;=\; \sigma_0 \mathbf{v}_0^{(i)} \cdot \mathbf{p} + v_{\mathrm{F}} \sigma_l \lambda^{(i)}_{l\,m} p_m \quad , \quad \mathbf{p} = \mathbf{k} - \mathbf{k}_{0,i}\,, \tag{3.1}$$

where σ_0 is the identity matrix and $\lambda_{l\,m}$ is an arbitrary real matrix of parameters (we use Einstein's summation convention). Unlike the Hamiltonian Eq. (2.1) which describes idealized Weyl nodes, Eq. (3.1) is the Hamiltonian for the most general form of Weyl nodes aligned with the chemical potential. This includes [71] the possibility of a term independent of pseudospin, $\mathbf{v}_0^{(i)}$, and an anisotropic term, $\lambda^{(i)}$. The dispersion of nodes in Eq. (3.1) is,

$$\begin{aligned} \xi_i(\mathbf{k}) \;&=\; \mathbf{v}_0^{(i)} \cdot \mathbf{p} \pm v_{\mathrm{F}} \sqrt{\mathbf{p}^{\mathrm{T}} \lambda^{(i),\mathrm{T}} \lambda^{(i)} \mathbf{p}} \quad , \quad \mathbf{p} = \mathbf{k} - \mathbf{k}_{0,i} \\ &=\; K^{(i)}(\mathbf{p}) \pm U^{(i)}(\mathbf{p}) \end{aligned} \tag{3.2}$$

The presence of $\mathbf{v}_0^{(i)}$ and $\lambda^{(i)}$ affects the Weyl node energy in different ways. In Fig. 3.1 these effects are illustrated by the contour plots of constant energies. For "ideal isotropic" nodes (black lines), i.e., $\mathbf{v}_0^{(i)} = \mathbf{0}$ and $\lambda^{(i)} = \sigma^0$, these contours are circles in a 2-dimensional plot of p_x and p_y, where $\mathbf{p}$ is the momentum away from Weyl node $\mathbf{k}_{0,i}$. Due rotational symmetry with respect to the Weyl nodes these contours are spheres as a function of p_x, p_y, p_z. On the other hand, the constant energy contours of "tilted isotropic" nodes (red lines), e.g., $\mathbf{v}_0^{(i)}/v_\mathrm{F} = 0.1\hat{\mathbf{x}}$ and $\lambda^{(i)} = \sigma^0$, are distorted circles in a 2-dimensional plot of p_x and p_y and similarly p_x and p_z. The term $\mathrm{v}_{0,x}^{(i)} p_x$ tilts the isotropic node in the direction of p_x. Finally, the constant energy contours of "anisotropic" nodes (blue lines), e.g., $\mathbf{v}_0^{(i)} = \mathbf{0}$ and $\lambda^{(i)} = \mathrm{diag}(2, 1, 1)$, are ellipses in a 2-dimensional plot of p_x and p_y. Due to symmetry between p_y and p_z, these are ellipsoids as a function of p_x, p_y, p_z.

Before continuing, let us take note that in our definition of Weyl nodes Eq. (3.1), the factorization of the coefficients of the second term as $v_\mathrm{F}\lambda^{(i)}$ is arbitrary; v_F can be chosen in a convenient way, and the remaining factors which describe the anisotropy are placed in $\lambda^{(i)}$. We have chosen to stick with Weyl nodes defined by Eq. (3.1), which we have to keep in mind in Ch. 3.1.1. As the dimensionless anisotropic matrix $\lambda^{(i)}$ has row index in pseudospin space and column index in momentum space, it has no generic symmetry. One therefore interprets $v_{(i)}^2 = v_\mathrm{F}^2 \lambda^{(i),T} \lambda^{(i)}$ as the squared velocity matrix, which is necessarily symmetric and therefore orthogonally diagonalizable. The eigenvectors of $v_{(i)}^2$ are the principal axes of the node, and the square root of

its eigenvalues are the speeds of the excitations along the principal directions. For example, in the above anisotropic case, the excitations are moving along principal directions $\hat{\mathbf{x}}, \hat{\mathbf{y}}$ and $\hat{\mathbf{z}}$ with magnitudes $2v_{\mathrm{F}}, v_{\mathrm{F}}$ and v_{F}, respectively, i.e., the slope of the dispersion along the x-axis is twice that of the y- and z-directions. For isotropic Weyl nodes on the other hand, the velocities are the same in any direction.

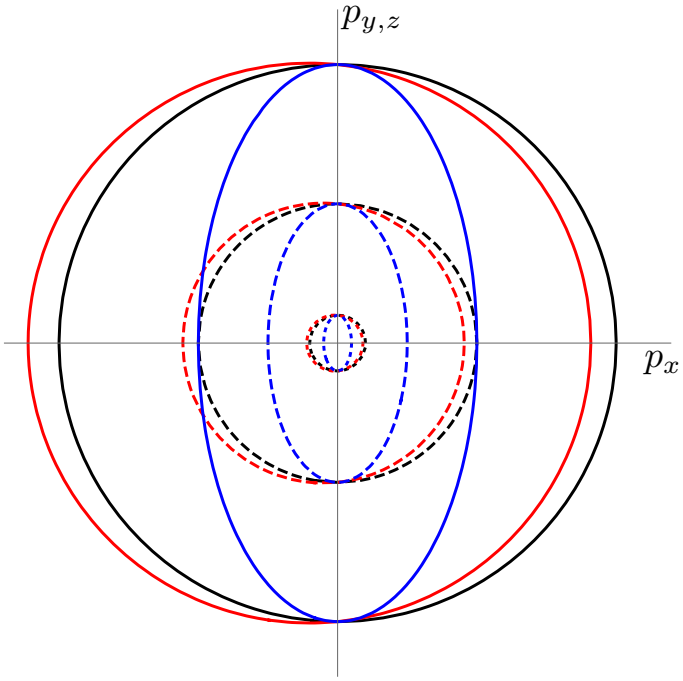

Figure 3.1: Constant energy contours of a Weyl node dispersion Eq. (3.3) as a function of momentum p_x and p_y (and similarly p_x and p_z). Full, dashed and dotted lines are contours of constant energy ξ_i for larger to smaller energy. Black lines plot an isotropic node. Red lines plot an isotropic node "tilted" in the x-direction. Blue lines plot an anisotropic node with symmetry in y- and z-directions.

Weyl nodes are generally classified into 4 types [72]. Here, we only have to draw the distinction between type-I and II nodes before continuing developing a theory for inelastic neutron scattering off type-I Weyl nodes. The distinction between a type-I and type-II node is that a node is type-II if there exists a direction $\mathbf{p}'$ in momentum space where $K(\mathbf{p}') \geq U(\mathbf{p}')$. When that is the case, electron and hole pockets co-exist at finite momentum, producing a finite density of states at the chemical potential.

This scenario is very different from type-I, where the density of states is vanishing at the chemical potential because of its point-like Fermi surface.

Contrary to Weyl nodes on the form Eq. (2.1), the form Eq. (3.1) poses questions about the possibility of obtaining any useful information from the structure factor. The foremost concern is the momentum conservation in a scattering event. We saw in Ch. 2 that the constraint of momentum conservation in scattering between nodes means that momenta from the two nodes are subtracted. The problem is that nodes on the form Eq. (3.1) have the possibility that their principal axes are *not* aligned with each other[1]. If so, the momentum conservation in internode scattering would mix components of momentum from the hole and particle along their different principal axes; i.e., no momentum conservation in a single coordinate system at all. Hence, to ensure momentum conservation in a single coordinate system, we need to transform the nodes in the original "physical" coordinates $\mathbf{p}$ into "isotropic" coordinates $\tilde{\mathbf{p}}$, where their principal axes are aligned. The dynamic structure factor, Eq. (2.3), which we seek is therefore $S_{l\,m}(\tilde{\mathbf{q}}, \omega)$ and no longer $S_{l\,m}(\mathbf{q}, \omega)$.

[1]Note that for intranode scattering this is not a problem, since the momenta of both hole and particle is within the *same* node. However, still in this case for the sake of calculating the dynamic structure factor, it is convenient (which will become apparent in Ch. 3.3) to transform momentum into isotropic coordinates.

3.1.1 Principal Axis Transformation $\mathcal{T}$

From now on, we will assume scattering is between a pair of nodes that are related by either time-reversal or inversion symmetry. Only with this restriction are we able to find the transformation to isotropic coordinates.

Define the nodes to be at $\mathbf{k}_{0,2} = -\mathbf{k}_{0,1} = \mathbf{k}_0$. The above symmetry takes a particle at the second Weyl point in the first-quantized state ψ_2 to $\psi_1 = T\psi_2$ or $\psi_1 = I\psi_2$ at the first Weyl point, in the case of time-reversal and inversion, respectively, where $T = \theta K$ and $I = \theta$ with K, a complex conjugation and θ, a unitary matrix. The matrix θ can be chosen *arbitrarily*, since the two states at each Weyl point are pseudospin states. One can choose the states in some particular way at the second Weyl point and define the two states at the first Weyl point by the transformation of these states under the appropriate symmetry combined with a convenient θ. Notice, that it *is* required that $T^2 = -1$ and $I^2 = 1$, but rather than constraining θ, they determine the way that T and I transform the first Weyl point back to the second. For example, for inversion symmetry θ does not have to square to 1 as long as $\psi_1 \to \psi_2 = \theta^\dagger \psi_1$ then $I^2 = 1$.

Let us unpack this knapsack and temporarily assume $\mathbf{v}_0^{(i)} = \mathbf{0}$ in Eq. (3.1). The total Hamiltonian in momentum representation is then,

$$H \;=\; \sum_{i=1,2} \sum_{\mathbf{k}} c^\dagger_{\mathbf{k},i} H_{0,i}(\mathbf{p}) c_{\mathbf{k},i} \quad , \quad H_{0,i}(\mathbf{p}) = v_{\mathrm{F}} \sigma_l \lambda^{(i)}_{l\,m} p_m \quad , \quad \mathbf{p} = \mathbf{k} - \mathbf{k}_{0,i}\,. \tag{3.3}$$

The Hamiltonian has to be Hermitian, which means that $\lambda_{l\,m}^{(i)} \in \mathbb{R}$ for both nodes $i = 1, 2$. The requirement that the Hamiltonian is invariant under time-reversal or inversion symmetry means that the nodes are related by $\theta H_{0,2}^{*}(\mathbf{k})\theta^{\dagger} = H_{0,1}(-\mathbf{k})$ and $\theta H_{0,2}(\mathbf{k})\theta^{\dagger} = H_{0,1}(-\mathbf{k})$, respectively, for any choice of unitary matrix θ. We choose $\theta = \sigma_y$ for time-reversal symmetry, because with this choice, the requirement that the Hamiltonian is invariant under this symmetry dictates that $\lambda^{(1)} = \lambda^{(2)}$. For inversion symmetry we choose $\theta = \sigma_0$, because with this choice, the requirement that the Hamiltonian is invariant under this symmetry dictates that $\lambda^{(1)} = -\lambda^{(2)}$. In other words, for both kinds of symmetry the dispersion of a node and its image is the same, which ensures that the transformation $\mathcal{T}$ we seek (not to be confused with time-reversal operation T) acts simultaneously on both nodes in the scattering process. Moreover, these choices of θ are particularly neat because *only* with these can the standard isotropic form of both Hamiltonians $H_{0,1}$ and $H_{0,2}$ occur. For example, define $H_{0,2} = v_{\mathrm{F}}\boldsymbol{\sigma} \cdot (\mathbf{k} - \mathbf{k}_0)$ to be on the standard isotropic form, then the time-reversed image for $\theta = \sigma_x$ is $H_{0,1} = v_{\mathrm{F}}[\sigma_x(\mathbf{k} + \mathbf{k}_0)_x - \sigma_y(\mathbf{k} + \mathbf{k}_0)_y - \sigma_z(\mathbf{k} + \mathbf{k}_0)_z]$, whereas for $\theta = \sigma_y$ it is $H_{0,1} = v_{\mathrm{F}}\boldsymbol{\sigma} \cdot (\mathbf{k} + \mathbf{k}_0)$. Both forms of $H_{0,1}$ are right-handed as $H_{0,2}$, but only $\theta = \sigma_y$ transforms $H_{0,1}$ to the standard isotropic form as $H_{0,2}$.

We seek a principal axis transformation $\mathcal{T}$ of original momentum, which together with a change of basis on pseudospin, transforms the original anisotropic Weyl node Hamiltonian Eq. (3.3) into isotropic form Eq. (3.5). This transformation must have

a determinant of one to ensure that the density of states for exciting Weyl fermions does not change in the momentum transformation (see Sec. 3.3). Hence, in the factorization of Eq. (3.3), the anisotropy matrix λ was required to be chosen such that it has a determinant of one as well. This, in return, determines the new velocity v_{F} of the isotropic Weyl nodes, Eq. (3.5). Because of our choice to define a Weyl node Hamiltonian with above factorization of the anisotropic term, the requirement $|\mathcal{T}| = 1$ is not aesthetic but physical.

In order to transform both nodes into isotropic form, it is sufficient to perform a singular value decomposition on $\lambda^{(2)}$ only because of $\lambda^{(1)} = \pm\lambda^{(2)}$. A singular value decomposition [73] is a general way to diagonalize non-Hermitian matrices; it is a representation in the form $\lambda^{(2)} = ODR^{\mathrm{T}}$ with orthogonal matrices O and R and a diagonal matrix $D_{ab} = d_a\sigma^0_{ab}$ (Einstein summation convention suspended), the elements of which are the singular values, i.e., the components of vector $\mathbf{d}$ are the square root of the eigenvalues of $\lambda^{(2),\mathrm{T}}\lambda^{(2)}$. To transform the anisotropic Weyl node Hamiltonian, Eq. (3.3), into isotropic form, one then transforms both momentum and spin degrees of freedom. The new "isotropic" coordinate for momentum $\tilde{\mathbf{p}} = \mathcal{T}\mathbf{p}$ is obtained from the original "physical" coordinate $\mathbf{p}$ by a transformation,

$$\mathcal{T} = R^{\mathrm{T}}D \quad , \quad |\mathcal{T}| = 1 \quad , \quad \tilde{\mathbf{p}} = \mathcal{T}\mathbf{p}\,. \tag{3.4}$$

This transformation is a coordinate rotation R^{T} (transpose of R) and scaling $d_a > 0$.

If spin is transformed [74] by a unitary matrix U such that $O_{a\,i}\sigma_i = U^\dagger \sigma_a U$, then the transformation $H_{0,2}(\mathbf{p}) \to U H_{0,2}(\mathcal{T}^{-1}\tilde{\mathbf{p}})U^\dagger$ brings the second node, and thus both nodes, into isotropic form,

$$H_{0,i}(\mathbf{p}) \to H_{0,i}(\tilde{\mathbf{p}}) = \chi_i v_{\mathrm{F}} \boldsymbol{\sigma} \cdot \tilde{\mathbf{p}}\,, \tag{3.5}$$

where the velocity v_{F} is now the geometric mean of the three principal velocities of Eq. (3.3). Here, chirality is $\chi_1 = \chi_2$ for time-reversal symmetric nodes, and $\chi_1 = -\chi_2$ for inversion symmetric nodes, or alternatively $\chi_i = sign|\lambda^{(i)}|$.

By the transformation Eq. (3.4) we can relate the dispersion of anisotropic nodes, Eq. (3.3), to isotropic nodes, Eq. (3.5). Because the dispersions for both time-reversal and inversion symmetry related nodes are the same due to $\lambda^{(1)} = \pm\lambda^{(2)}$, their dispersions are,

$$\begin{aligned} \xi_i(\mathbf{k}) &= \pm v_{\mathrm{F}} \sqrt{\mathbf{p}^{\mathrm{T}} \lambda^{(2),\mathrm{T}} \lambda^{(2)} \mathbf{p}} \quad , \quad \mathbf{p} = \mathbf{k} - \mathbf{k}_{0,i}\,, & \text{(3.6a)} \\ &= \pm v_{\mathrm{F}} |\tilde{\mathbf{p}}| \qquad\qquad\quad , \quad \tilde{\mathbf{p}} = \mathcal{T}\mathbf{p}\,. & \text{(3.6b)} \end{aligned}$$

In the second form we used $\lambda^{(2)} = ODR^{\mathrm{T}}$ and Eq. (3.4) to define $\tilde{\mathbf{p}} = \mathcal{T}\mathbf{p}$. Notice that the contours of constant energy of the dispersion in physical coordinates, Eq. (3.6a), as a function of $\mathbf{p}$ is ellipsoidal, whereas the dispersion in isotropic coordinates, Eq. (3.6b), as a function of $\tilde{\mathbf{p}}$ is a sphere. Figure 3.1 illustrates the contours of constant

energy for dispersions Eq. (3.6) in the isotropic case and for a specific anisotropy.

Section 5.1 and 5.2 illustrate how to transform the Hamiltonian of a toy model Weyl semimetal from physical to isotropic coordinates. In these chapters, we will also use the opportunity to dwell on the particular factorization of Weyl node anisotropy of Eq. (3.1), which is of utmost importance when deriving the transformation Eq. (3.4).

3.1.1.1 Measuring the Principal Axis Transformation $\mathcal{T}$

In order to unravel several properties of Weyl fermions from the cross-section data, one needs to experimentally measure the principal axis transformation $\mathcal{T}$, that is required to transform the cross-section data before one can interpret it.

Recall that Ch. 2 introduced the transferred momentum $\mathbf{\Delta}$ as the convenient variable to describe internode scattering between isotropic Weyl nodes. It was defined as $\mathbf{\Delta} = \Delta\mathbf{k}_0 - \mathbf{q}$, i.e., the deviation between the transferred neutron momentum $\mathbf{q}$ and the vector connecting the exact positions of the nodes $\Delta\mathbf{k}_0$. The internode vector $\Delta\mathbf{k}_0 = \pm 2\mathbf{k}_0$ corresponds to the two $\mathrm{M}^{\pm}$ transitions illustrated in Fig. 2.1. Chapter 2 explained furthermore that the region of nonzero scattering between idealized nodes, Eq. (2.4), is restricted to $\hbar\omega \geq v_{\mathrm{F}}|\mathbf{\Delta}|$, i.e., two spheres for a fixed energy as illustrated in Fig. 2.2. For a material with nodes already in the isotropic form, no principal axis transformation $\mathcal{T}$ is needed, but only for nodes that are anisotropic.

In general, the dispersion of Weyl fermions is likely to be anisotropic. We can find the region of allowed momentum and energy transfer by utilizing the transformation of anisotropic nodes, Eq. (3.3), to isotropic form, Eq. (3.5), by the principal axis transformation $\mathcal{T}$, Eq. (3.4), which we need to measure from an experiment. Hence, from the result of Ch. 2 together with the transformation, we have,

$$\hbar\omega \geq v_{\mathrm{F}}|\tilde{\mathbf{\Delta}}|\,, \tag{3.7a}$$

$$\hbar\omega \geq v_{\mathrm{F}}\sqrt{\mathbf{\Delta}^{\mathrm{T}}\lambda^{(2),\mathrm{T}}\lambda^{(2)}\mathbf{\Delta}}\,. \tag{3.7b}$$

Hence, for a fixed energy $\hbar\omega$ the nonzero regions are two spheres as a function of $\tilde{\mathbf{\Delta}} = \mathcal{T}\mathbf{\Delta}$, whereas they are two ellipsoids as a function of $\mathbf{\Delta}$. The regions of allowed scattering therefore correspond to the single particle constant energy contours of Eq. (3.6) illustrated in Fig. 3.1.

In an experiment, one measures the cross-section as a function of neutron momentum transfer, $\mathbf{q}$, at a given neutron energy transfer, $\hbar\omega$, and will therefore observe Eq. (3.7b), i.e., two ellipsoid regions centered on $\pm 2\mathbf{k}_0$. By measuring the directions and lengths of the principal axes of one of these ellipsoids, one can construct $\mathcal{T}$. The directions of the principal axes give the eigenvectors $\hat{\mathbf{v}}_i$ of $\lambda^{(2),\mathrm{T}}\lambda^{(2)}$ used to construct the coordinate rotation matrix $R = [\hat{\mathbf{v}}_1, \hat{\mathbf{v}}_2, \hat{\mathbf{v}}_3]$. The lengths of the principal axes, $\hbar\omega/v_{\mathrm{F}}d_i$, give the eigenvalues squared d_i^2 of $\lambda^{(2),\mathrm{T}}\lambda^{(2)}$ used to construct the diagonal "stretching" matrix with elements $\mathbf{d} = (d_1, d_2, d_3)^{\mathrm{T}}$ ordered as $d_1 \geq d_2 \geq d_3 > 0$.

From these measurements, one can construct the linear transformation $\mathcal{T}$, Eq. (3.4), that distorts this ellipsoid to a sphere given by Eq. (3.7a) upon redefining $\tilde{\mathbf{\Delta}} = \mathcal{T}\mathbf{\Delta}$. In other words, these are measurements of the anisotropic Weyl node dispersion.

Notice that the regions of allowed momentum and energy transfer, Eq. (3.7), are the same regions of the density of states of Weyl excitations (see Sec. 6.1). The structure factor and cross-section are therefore also restricted to these regions, although the intensity would vary within the region because of spin-momentum locking. In the case that spin-momentum locking causes the intensity along a principal axis to be too low to be resolved, one can then vary the energy $\hbar\omega$ of Weyl fermions. In this way, one can measure from the cross-section the principal axes, velocities of the dispersion, as well as the transformation $\mathcal{T}$ that will be important to be able to see the predictions of this theory (see Ch. 6).

Section 5.3 illustrates how to measure the transformation $\mathcal{T}$ for inelastic neutron scattering from a toy model Weyl semimetal.

3.1.2 Conditions for Lorentz Invariance and its Consequences

This section summarizes which type-I Weyl nodes our theory of internode scattering is applicable to. The scattering is restricted to pairs of nodes which can simultaneously be *transformed* to the relativistic (Lorentz invariant) form Eq. (2.1). We will

see below that Lorentz invariance leads to some special properties of the cross-section: physically (measurable), there is a discontinuity of the cross-section at the surface of the spherical regions in momentum space where the cross-section is nonzero; mathematically, the variation of the cross-section as a function of momentum can be found using Lorentz transformations.

As explained in Sec. 3.1.1, transforming the momentum by a linear transformation $\tilde{\mathbf{p}} = \mathcal{T}\mathbf{p}$ as well as the spin, we can remove the anisotropy of Eq. (3.1). However, there is no way to eliminate the term independent of pseudospin by a coordinate transformation. This transforms the Hamiltonian of the i^{th} $(i = 1, 2)$ low energy region into,

$$H_{0,i}(\tilde{\mathbf{k}}) = \sigma_0 \tilde{\mathbf{v}}_0^{(i)} \cdot \tilde{\mathbf{p}} + \chi_i v_{\text{F}} \boldsymbol{\sigma} \cdot \tilde{\mathbf{p}} \quad , \quad \tilde{\mathbf{p}} = \mathcal{T}\mathbf{p} = \mathcal{T}(\mathbf{k} - \mathbf{k}_{0,i}) \,, \tag{3.8}$$

where $\tilde{\mathbf{v}}_0^{(i)}$ is $\mathbf{v}_0^{(i)}$ in the new coordinates. The type of symmetry connecting the Weyl nodes determines their relative chirality; for time-reversal and inversion symmetry, they are $\chi_1 = \chi_2$ and $\chi_1 = -\chi_2$, respectively.

This form of the Hamiltonian makes it clear that the only term which breaks Lorentz symmetry is $\tilde{\mathbf{v}}_0^{(i)}$. In this dissertation, we will focus on the cross-section[2] in the Lorentz-invariant case $\tilde{\mathbf{v}}_0^{(i)} = \mathbf{0}$. This case is a good starting point for understanding

[2]Notice, that the cross-section of any type-I Weyl semimetal, $|\tilde{\mathbf{v}}_0| \leq v_{\text{F}}$, is analytically tractable as outlined in Ref. [28]

neutron scattering off Weyl semimetals, although the term $\tilde{\mathbf{v}}_0^{(i)}$ is present in generic Weyl semimetals (c.f. Sec. 1.3) and it can change some of the predictions made here.

The transformation $\mathcal{T}$ is constructed such that the second term in Eq. (3.1) transforms into the standard isotropic form of Eq. (3.8). If the term $\tilde{\mathbf{v}}_0^{(i)}$ is negligible, then the Hamiltonian is clearly isotropic and even has a relativistic symmetry. Importantly, because of the time-reversal or inversion symmetry, the transformation $\mathcal{T}$ is the same for both nodes; i.e., the nodes have their *principal axes aligned* and are *isotropic* in a single coordinate system. This is crucial for our calculation of the dynamic structure factor (see Sec. 3.3); without it, we would not be able to use Lorentz symmetry, and the contour of constant energy of excitations would not have the simple ellipsoidal shape that is found in Sec. 6.1. As a consequence, the regions of nonzero scattering would not end sharply. In order to compare experimental results to this theory, it will be necessary to determine the transformation. We showed in Sec. 3.1.1.1 that it is easy to see the form of $\mathcal{T}$ experimentally from a plot of the structure factor at fixed neutron energy transfer, and Sec. 5.3 illustrates this for a Weyl semimetal toy model.

The following are the precise conditions under which Lorentz invariance can be assumed:

1. The nodes involved in the scattering are aligned (or nearly aligned) with the chemical potential. This requires careful doping of the materials discovered so

far. But in a material where all the Weyl nodes are at the same energy, due to symmetry, it can be an automatic property of a compound with an even number of electrons per unit cell.

2. Scattering is between two nodes connected by either time-reversal or inversion symmetry.

3. The three components of $\tilde{\mathbf{v}}_0^{(i)}$ in Eq. (3.8) vanish. Although *this* condition is not generally satisfied exactly, we will assume it to be, in order to be able to use Lorentz invariance. A nonzero but small, $|\tilde{\mathbf{v}}_0|/v_\mathrm{F} \ll 1$, does not change the predictions too much.

Under these conditions, the dynamics of the excitations of the material are entirely Lorentz invariant, but their interaction with neutrons is not. Thus, the cross-section will not be Lorentz invariant, but it can be predicted using Lorentz symmetry. It turns out that the cross-section for a given initial and final neutron polarization is a certain component of a relativistic tensor (see Ch. 4); the tensor for any net momentum $\tilde{\mathbf{\Delta}}$ can be obtained by applying a Lorentz transformation to that tensor in the rest frame (see Sec. 3.3 and Appx. B).

3.2 Neutron-Weyl Fermion Interaction

In a neutron experiment, one is bound to be concerned with the strength of the cross-section, because one always has to have adequate counting statistics in order to be able to detect any signal. In purely conventional magnetic scattering, the strength of the cross-section is basically determined by the density of states of excitations times the classical electron radius squared because the bare coupling of neutron to magnetic moment per Bohr magneton is $\frac{g}{2} = 1$ for an electron spin-$\frac{1}{2}$ magnetic moment $\frac{g}{2}\mu_{\mathrm{B}}\boldsymbol{\sigma}$. In Weyl semimetals, the density of states of excitations for a single Weyl node is $\propto (\hbar\omega)^2$, which is small for low energy transfers $\hbar\omega$. Although, we will show in Ch. 6 that all the obstacles of inelastic neutron scattering off Weyl semimetals mentioned in Ch. 2 can be circumvented; still, it is a practical concern whether the strength of a signal is large enough. In this section, the coupling of neutron to Weyl fermions will be derived in generality. It turns out that this coupling behaves very differently from that of conventional magnetic scattering and can be large enough to compensate for the small density of states. In Sec. 5.4, we will use a Weyl semimetal toy model as a proof of concept to illustrate this point. The strength of the cross-section will be discussed in Ch. 6.

The interaction of a neutron with a Weyl semimetal (treated in the Born approximation) was hitherto described as the vector potential operator $\mathbf{A}(\mathbf{r})$ of the neutron's

magnetic moment interacting with the current $\mathbf{J}(\mathbf{r})$ of the electronic system:

$$H_{\mathbf{A}} = -\int_V \mathrm{d}\mathbf{r}\, \mathbf{J}(\mathbf{r}) \cdot \mathbf{A}(\mathbf{r} - \mathbf{r}_{\mathrm{n}})\,, \tag{3.9}$$

where $\mathbf{A}(\mathbf{r} - \mathbf{r}_{\mathrm{n}})$ is the vector potential of a neutron at $\mathbf{r}_{\mathrm{n}}$. If a full realistic band structure is available, a direct way to calculate the scattering function $S_{l\,m}(\mathbf{r}, t) = \langle J_l(\mathbf{r}, t) J_m(\mathbf{0}, 0)\rangle_0$ would be to evaluate the matrix elements of the exact current operator (including spin and orbital parts) between the Bloch states. However, near a Weyl point, one can focus on a few parameters from this calculation and obtain an effective current operator $\mathbf{J}_{eff}(\mathbf{r})$, which can be represented as an effective anomalous magnetic moment operator $\mathbf{M}(\mathbf{r})$. Hence, the interaction between the neutron and the electrons, Eq. (3.9), can be replaced by the standard form for the energy of a dipole in a magnetic field:

$$H_{\mathbf{B}} = -\int_V \mathrm{d}\mathbf{r}\, \mathbf{M}(\mathbf{r}) \cdot \mathbf{B}(\mathbf{r} - \mathbf{r}_{\mathrm{n}})\,, \tag{3.10}$$

where $\mathbf{B}(\mathbf{r}-\mathbf{r}_{\mathrm{n}})$ is the magnetic field induced by a neutron at $\mathbf{r}_{\mathrm{n}}$. Once having obtained $\mathbf{M}(\mathbf{r})$, the dynamic structure factor we seek is $S_{l\,m}(\mathbf{r}, t) = \langle M_l(\mathbf{r}, t) M_m(\mathbf{0}, 0)\rangle_0$. A description in terms of the interaction Eq. (3.9), with $\mathbf{J}_{eff}(\mathbf{r})$ replacing $\mathbf{J}(\mathbf{r})$, or by Eq. (3.10) yields the same cross-section, of course, but offers different interpretations. The former approach, conventional in quantum electrodynamics [29, 75], is intuitive in that a scattering event generates an electronic transition current between nodes.

The latter approach, conventional in neutron scattering literature [76, 77], offers a standard interpretation of $S_{l\,m}(\tilde{\mathbf{q}}, \omega)$ proportional to a pseudospin susceptibility by the dissipation-fluctuation theorem. Furthermore, this naturally leads us to wonder whether an emergent electric dipole moment of the Weyl fermions should exist, as well as the emergent magnetic moment (see Ch. 7). Next, we will find the emergent magnetic moment of Weyl fermions in order to treat the coupling as Eq. (3.10).

3.2.1 Magnetic Moments of Weyl Fermions

In an actual experiment, if one plots the cross-section at a fixed $\hbar\omega$ as a function of the momentum transfer $\mathbf{q}$, one will see two regions of scattering corresponding to the $\mathrm{M}^{\pm}$ transitions as illustrated in Fig. 2.2. Since the two transitions can be related to one another (see Sec. 3.3), we only need to find interaction for the M^{+} transition. To find the effective electronic current operator, describing transition between Weyl nodes, we begin by establishing the low-energy subspaces.

The Weyl Hamiltonian in the vicinity of the Weyl point, $\mathbf{k}_{0,i}$, can be developed from the degenerate states exactly at these points by using time-independent, degenerate perturbation theory. The Hamiltonian at a nearby point $H_{0,i}(\mathbf{k}_{0,i} + \mathbf{p})$ can be found by treating $\mathbf{p}$ as a perturbation. We project it into the twofold degenerate subspace $D_i = \{|s; \mathbf{k}_{0,i}\rangle\}$ *exactly at* the nearby Weyl point, enumerated by an arbitrary pseudospin label $s = \pm 1$. These are not necessarily different spin states;

they can be any two degenerate states, and could differ in orbital structure instead of spin, for example. For momenta $\mathbf{p} \neq \mathbf{0}$ away from the node, the projected Hamiltonian can be expanded to first order as $\mathbf{w}^{(i)} \cdot \mathbf{p}$ which removes the degeneracy, where $\mathbf{w}^{(i)} = \partial H_{0,i}(\mathbf{p} + \mathbf{k}_{0,i})/\partial \mathbf{p}|_{\mathbf{p}=\mathbf{0}}$ is a vector of 2×2 matrices. Expanding in terms of the three Pauli matrices and the identity matrix gives the effective low energy Weyl Hamiltonian Eq. (3.1), under the assumption that the nodes are aligned at the chemical potential. Note that the states $\{|s, \mathbf{k}_{0,i}\rangle\}$ are not eigenstates at a nonzero $\mathbf{p}$; the energy eigenstates take the form $\sum_{s=\pm 1} c_s(\mathbf{p})|s; \mathbf{k}_{0,i}\rangle$, where the c_s's form the eigenvector of $\mathbf{w}^{(i)} \cdot \mathbf{p}$ in its representation D_i. In other words, the c_s's are the components of the eigenspinor $|\mathbf{p}; \eta\chi\rangle$ of the Weyl equation.

For the M^+ transition, we need only the current's overlaps between states of the degenerate subspaces D_1 and D_2. Below, we will see that the current $\mathbf{J}$ forms a vector $\boldsymbol{\mathcal{J}}(2\mathbf{k}_0)$ of 2×2 matrices that describes the effective electronic current within the low-energy subspaces. This matrix has no momentum dependence because it is defined with respect to the basis $\{|s; \mathbf{k}_{0,i}\rangle\}$, which are not energy eigenstates. The momentum and polarization dependence of the neutron cross-section arise from the functions $\mathbf{c}(\mathbf{p})$, as will be explained intuitively in Sec. 6.2.

Within the effective Weyl fermion description, $\boldsymbol{\mathcal{J}}(2\mathbf{k}_0)$ is the 1^{st} quantized operator corresponding to the current; it has the same matrix elements for corresponding states

in the more realistic descriptions. Conservation of momentum gives,

$$\langle s; \mathbf{k}_{0,2} + \mathbf{p}_2 | \mathbf{J}(\mathbf{q}) | \mathbf{k}_{0,1} + \mathbf{p}_1; s' \rangle = \delta^3(\mathbf{q} - 2\mathbf{k}_0 + \boldsymbol{\Delta}) \boldsymbol{\mathcal{J}}(2\mathbf{k}_0)_{ss'}, \tag{3.11}$$

without any dependence of the matrix elements on $\boldsymbol{\Delta}$, which is valid for $|\boldsymbol{\Delta}| \ll |2\mathbf{k}_0|$ as is considered here. The transition current density $\boldsymbol{\mathcal{J}}(2\mathbf{k}_0)$ is purely transverse with respect to $2\mathbf{k}_0$. The electron-neutron coupling is hereby reduced to Eq. (3.9) with the effective Weyl fermion current $\mathbf{J}_{eff}(\mathbf{r})$ replacing $\mathbf{J}(\mathbf{r})$, given by,

$$\mathbf{J}_{eff}(\mathbf{r}, t) = \Psi_2^\dagger(\mathbf{r}, t) \boldsymbol{\mathcal{J}}(2\mathbf{k}_0) \Psi_1(\mathbf{r}, t) + h.c. \tag{3.12}$$

From electromagnetism, we know that current is related to magnetization by $\mathbf{J} = \text{curl } \mathbf{M}$. By standard manipulations [78], we reverse engineer (which is valid for momenta near the nodes) to obtain a magnetization operator,

$$\begin{aligned} \mathbf{M}(\mathbf{r}, t) &= \mathbf{M}^{(+)}(\mathbf{r}, t) + \mathbf{M}^{(-)}(\mathbf{r}, t)\,, & \text{(3.13a)} \\ \mathbf{M}^{(+)}(\mathbf{r}, t) &= \Psi_2^\dagger(\mathbf{r}, t) \boldsymbol{\mathcal{M}} \Psi_1(\mathbf{r}, t)\,, & \text{(3.13b)} \\ \mathbf{M}^{(-)}(\mathbf{r}, t) &= \mathbf{M}^{(+),\dagger}(\mathbf{r}, t)\,. & \text{(3.13c)} \end{aligned}$$

This allows one to express the interaction between the neutron and the electrons as the standard form for the energy of a dipole in a magnetic field, Eq. (3.10), induced by the neutron. Furthermore, the magnetization $\boldsymbol{\mathcal{M}}$, being a 2×2 matrix, can be

expanded as:

$$\boldsymbol{\mathcal{M}} = \mu_{\mathrm{B}} \sigma_{\mu} \mathbf{F}^{\mu} \quad , \quad \mu = 0, 1, 2, 3. \tag{3.14}$$

The j^{th} component of $\mathbf{F}^{\mu} \in \mathbb{C}^3$ is defined as the (j, μ) component of $\mathbf{F}^{\mu}$, a 4×3 matrix which describes the coupling between the magnetic degree of freedom j and the pseudospin degree of freedom μ. Since these indices transform differently (one with spatial rotations and one with redefinition of the pseudospin basis), F_j^{μ} is not a geometrical object. It is merely a collection of complex coupling coefficients which relate the magnetic moment to the pseudospin, similar to the factor $\frac{g}{2}$ for an electron spin-$\frac{1}{2}$ magnetic moment $\frac{g}{2}\mu_{\mathrm{B}}\boldsymbol{\sigma}$, which Eq. (3.14) is a generalization of. Roughly, $\mathbf{F}^{\mu}$ can be interpreted as the "anomalous" components of a "Weyl magnetic moment". However, it is not completely correct to use this analogy. The reason is that the interaction involves a transition between states of two *different* nodes. Hence, the presence of the "anomalous magnetic moment" coupling $\mathbf{F}^{\mu}$ is a *quantum effect from the bands*, which acts like a force on the pseudospin.

It is useful to relate $\mathbf{F}^{\mu}$ to the effective current $\boldsymbol{\mathcal{J}}(2\mathbf{k}_0)$. In doing so, $\mathbf{F}^{\mu}$ can be determined numerically by Eq. (3.15), if one has developed a realistic band structure model, simply by evaluating the current operator (including both orbital and pseudospin currents) between the pair of degenerate wavefunctions as described above.

With respect to internode direction $\hat{\mathbf{k}}_0$, the couplings $\mathbf{F}^{\mu}$ can be divided into longitudinal and transverse parts $\mathbf{F}^{\mu} = \mathbf{F}^{\mu}_{\parallel} + \mathbf{F}^{\mu}_{\perp}$. Because of the neutron magnetic field, only perpendicular components enter the cross-section, meaning that we have

the freedom to set $\mathbf{F}^{\mu}_{\parallel} = \mathbf{0}$ for all μ. From the relations between $\boldsymbol{\mathcal{M}}$, $\mathbf{F}^{\mu}$ and $\boldsymbol{\mathcal{J}}$, we find,

$$\mathbf{F}^{\mu}_{\top} = \hat{\mathbf{k}}_0 \times \mathbf{F}^{\mu} = \frac{i\hbar}{2|2\mathbf{k}_0|\mu_{\mathrm{B}}} \mathrm{Tr}\left[\boldsymbol{\mathcal{J}}(2\mathbf{k}_0)\sigma^{\mu}\right], \tag{3.15a}$$

$$\mathbf{F}^{\mu}_{\perp} = \mathbf{F}^{\mu}_{\top} \times \hat{\mathbf{k}}_0. \tag{3.15b}$$

Contrary to conventional purely magnetic scattering, the coupling Eq. (3.15) is determined by sixteen real numbers without invoking constraints from symmetry. These contain information solely from bands, so without a specific band structure the couplings are unknown. Thus, the coupling is structurally much more complicated than the bare coupling of neutrons with matter, which is just a single number with magnitude $\frac{g}{2} = 1$. That is, $\mathbf{F}^{0}_{\perp} \neq \mathbf{0}$ *generally* and $\mathbf{F}^{i}_{\perp} \cdot \hat{\mathbf{j}} \neq \delta_{ij}$ *always*, (by the constraint $2\mathbf{k}_0 \cdot \mathbf{F}^{i}_{\perp} = 0$), and can even be very asymmetric with either a larger or smaller value than the bare coupling. Furthermore, $\mathbf{F}^{\mu}_{\perp}$ may become divergent upon approaching $|2\mathbf{k}_0| \to 0$, a topological phase transition. An example of these features is illustrated in Sec. 5.4 for a Weyl semimetal toy model[3] mimicking the more realistic model introduced in Sec. 1.3.1. To acquire some intuition about the coupling and its consequences for the cross-section, in Sec. 6.2 we will illustrate it for the case that most closely resemble conventional purely magnetic scattering, i.e., when $\mathbf{F}^{0} = \mathbf{0}$ and $\mathbf{F}^{i} \cdot \hat{\mathbf{j}} = \delta_{ij}$. Section 6.3 considers the cross-section for any possible coupling.

[3]Except for the toy model, the coupling's dependence on various Weyl semimetal' band structures has not been investigated.

3.3 Dynamic Structure Factor

We finally have all the ingredients to calculate the dynamic structure factor: the right coordinate system and interaction. First, the calculation must be done in the isotropic coordinate system $\tilde{\mathbf{q}} = \mathcal{T}\mathbf{q}$ with transformation $\mathcal{T}$ given by Eq. (3.4). The structure factor we calculate is thus $S_{l\,m}(\tilde{\mathbf{q}}, \omega)$, but we use the notation $S_{l\,m}(\mathbf{q}, \omega)$ to emphasize that the neutron actually sees $\mathbf{q}$. So, $S_{l\,m}(\mathbf{q}, \omega)$ means that it is a function of $\mathbf{q}$ implicitly thorough $\mathcal{T}\mathbf{q}$. Second, the interaction, Eq. (3.10), is that of a neutron's magnetic field with an emergent magnetic moment, Eq. (3.13), of the Weyl fermions.

The dynamic structure factor $S_{l\,m}(\mathbf{q}, \omega)$ is the frequency and momentum Fourier transform of the scattering function $S_{l\,m}(\mathbf{r}, t)$. The latter can be decomposed into $S_{l\,m}(\mathbf{r}, t) = S^{(-)}_{l\,m}(\mathbf{r}, t) + S^{(+)}_{l\,m}(\mathbf{r}, t)$, the contributions of the two processes $\mathrm{M}^{\pm}$ defined in Fig. 2.2, since we can ignore intranode scattering. For the M^{+} process,

$$S^{(+)}_{l\,m}(\mathbf{r}, t) \equiv V \left\langle M^{(-)}_{l}(\mathbf{r}, t)\, M^{(+)}_{m}(\mathbf{0}, 0) \right\rangle_{0}, \tag{3.16a}$$

$$= \mu_{\mathrm{B}}^{2} F^{\mu,*}_{l} F^{\nu}_{m} \sigma^{\mu\,\nu}_{(+)}(\mathbf{r}, t), \tag{3.16b}$$

which is a van Hove type correlation function of magnetization operators[4] (Heisen-

[4]Notice that the definition Eq. (3.16a) differs from that presented in previous chapters by having a volume V factor. The structure factor, Eq. (4.1), of the cross-section is the Fourier transform of Eq. (3.16a), and the volume expresses that translational invariance has been used.

berg representation), Eq. (3.13), in the Weyl semimetal equilibrium. The structure factor of a M^- transition follows trivially from that of a M^+ transition simply by interchanging Weyl node labels[5] $1 \leftrightarrow 2$. The Weyl fermion correlator,

$$\sigma^{\mu\,\nu}_{(+)}(\mathbf{r},t) \;=\; V\left\langle \sigma^{\mu}_{(-)}(\mathbf{r},t)\sigma^{\nu}_{(+)}(\mathbf{0},0)\right\rangle_0 \tag{3.17}$$

is an intermediate scattering function of non-Hermitian operators $\sigma^{\mu}_{(-)}(\mathbf{r},t) = \sigma^{\mu,\dagger}_{(+)}(\mathbf{r},t)$ and $\sigma^{\mu}_{(+)}(\mathbf{r},t) = \Psi_2^\dagger(\mathbf{r},t)\sigma^{\mu}\Psi_1(\mathbf{r},t)$. These excite an occupied state from the vicinity of one Weyl node to an empty state in the vicinity of the other Weyl node. Subsequently, we will turn to the particle-hole picture where Eq. (3.17) becomes a particle-hole correlator of the relativistic Weyl fermions.

The susceptibility is decomposed into $\chi^{\mu\,\nu}_{(+)}(\mathbf{q},\omega) = \chi'^{\mu\,\nu}_{(+)}(\mathbf{q},\omega) + i\chi''^{\mu\,\nu}_{(+)}(\mathbf{q},\omega)$, i.e., $\chi'^{(+)}_{\mu\nu}$, the reactive part and $\chi''^{\mu\nu}_{(+)}$, the absorptive part. According to the fluctuation-dissipation theorem, the scattering function and the absorptive part of the generalized susceptibility are related by $\sigma^{\mu\,\nu}_{(+)}(\mathbf{q},\omega) = \kappa(\omega,T)\chi''^{\mu\,\nu}_{(+)}(\mathbf{q},\omega)$ where $\kappa(\omega,T) = 2\hbar/(1 - e^{-\beta\hbar\omega})$ with $\beta^{-1} = k_{\mathrm{B}}T$. We know that $\chi''^{\mu\nu}_{(+)}$ is merely the polarization bubble for the M^+ transition. This could be derived directly from the generalized Kubo formula [77, 79], which expresses the linear response to the perturbation. In doing so, it is crucial to take into account that Eq. (3.17) involves non-Hermitian operators, and $\chi''^{\mu\nu}_{(+)}$ is therefore anti-Hermitian (contrary to being imaginary as its analog in

[5] Weyl node indices 1 and 2 will not appear explicitly, but only implicitly. However, interchanging $1 \leftrightarrow 2$ is equivalent to interchanging signs $(+) \leftrightarrow (-)$, and conjugating couplings $F^{\mu}_{l}F^{\nu,*}_{m} \leftrightarrow F^{\mu,*}_{l}F^{\nu}_{m}$ whenever they appear.

conventional purely magnetic scattering). Rather than doing this tedious derivation, we will resort to the Lehmann representation. At zero temperature and infinite volume limit, for noninteracting Weyl fermions in a translational invariant Weyl semimetal, we get that,

$$\chi''^{\mu\,\nu}_{(+)}(\mathbf{q},\omega) = \frac{\pi V}{(2\pi\hbar)^3}\int \mathrm{d}\tilde{\mathbf{p}}_i \int \mathrm{d}\tilde{\mathbf{p}}_f \;\; \delta(\tilde{\mathbf{p}} - \tilde{\mathbf{\Delta}})\,\delta\left(\hbar\omega - \Delta\xi^{\mathrm{w}}\right) \times \langle -\chi_i;\tilde{\mathbf{p}}_i|\sigma^{\mu}|\tilde{\mathbf{p}}_f;\chi_f\rangle\langle\chi_f;\tilde{\mathbf{p}}_f|\sigma^{\nu}|\tilde{\mathbf{p}}_i;-\chi_i\rangle\,, \tag{3.18}$$

with a change in internal energy $\Delta\xi^{\mathrm{w}} = \xi^{+}_{\tilde{\mathbf{p}}_f} - \xi^{-}_{\tilde{\mathbf{p}}_i}$. The energy of the occupied state $\xi^{-}_{\tilde{\mathbf{p}}_i}$ is negative, and the excited state $\xi^{+}_{\tilde{\mathbf{p}}_f}$ is positive. Equation (3.18) is the Lindhard function weighted by a pseudospin correlation between the Weyl fermion ejected from the occupied state (i.e., $|\tilde{\mathbf{p}}_i;-\chi_i\rangle$), and scattered into the unoccupied state (i.e., $|\tilde{\mathbf{p}}_f;+\chi_f\rangle$). The two-component spinor $|\tilde{\mathbf{p}};\eta\chi\rangle$ is that of Eq. (2.2), but in a notation that is more suitable to the discussion in Ch. 6 pertaining to the cross-section. Now we do a particle-hole transform [80], mainly for the reason that it makes the expressions more symmetric and the relativistic symmetry more apparent. A neutron transfers energy $\hbar\omega$ to the Weyl semimetal and creates a particle-hole Weyl pair. The change in energy can be rewritten as $\Delta\xi^{\mathrm{w}} \to \xi^{p}_{\tilde{\mathbf{p}}_f} + \xi^{h}_{\tilde{\mathbf{p}}_i} = v_{\mathrm{F}}\left(|\tilde{\mathbf{p}}_f| + |\tilde{\mathbf{p}}_i|\right)$ by reinterpreting $-\xi^{-}_{\tilde{\mathbf{p}}_i}$ as the energy $\xi^{h}_{\tilde{\mathbf{p}}_i}$ of the created hole. In order to make this picture consistent, we need to also redefine $\tilde{\mathbf{p}}_i \to -\tilde{\mathbf{p}}_i$, i.e., a sign change on $\tilde{\mathbf{p}}_i$ with

respect to the definition in Ch. 2. In this particle-hole picture, Eq. (3.18) becomes,

$$\chi''^{\mu\,\nu}_{(+)}(\mathbf{q},\omega) = c\int \frac{\mathrm{d}\tilde{\mathbf{p}}_i}{2\tilde{p}_i^0}\int \frac{\mathrm{d}\tilde{\mathbf{p}}_f}{2\tilde{p}_f^0}\,\delta^{(4)}\left(\mathrm{Q}-\mathrm{P}\right) 2\tilde{p}_i^0 2\tilde{p}_f^0\,\langle\chi_i;\widehat{\tilde{\mathbf{p}}}_i|\sigma^\mu|\widehat{\tilde{\mathbf{p}}}_f;\chi_f\rangle\langle\chi_f;\widehat{\tilde{\mathbf{p}}}_f|\sigma^\nu|\widehat{\tilde{\mathbf{p}}}_i;\chi_i\rangle, \tag{3.19}$$

with constant $c = \pi V/v_{\mathrm{F}}(2\pi\hbar)^3$. Now the solutions at 1^{st} Weyl point have chirality[6] $+\chi_i$. In this expression, the energy and 3-momentum delta functions have been combined into an energy-momentum 4-delta function. The neutron energy-momentum 4-vector is $\mathrm{Q}^\mu = (\mathrm{Q}^0, \mathbf{Q})$ with $\mathrm{Q}^0 \equiv \hbar\omega/v_{\mathrm{F}}$ and $\mathbf{Q} \equiv \tilde{\mathbf{\Delta}} = \Delta\tilde{\mathbf{k}}_0 - \tilde{\mathbf{q}}$, while the particle-hole Weyl pair energy-momentum 4-vector is $\mathrm{P}^\mu = (\mathrm{P}^0, \mathbf{P})$ with $\mathrm{P}^0 \equiv \Delta\xi^{\mathrm{w}}/v_{\mathrm{F}}$ and $\mathbf{P} \equiv \Delta\tilde{\mathbf{p}} = \tilde{\mathbf{p}}_1 + \tilde{\mathbf{p}}_2$. The integration measure and 4-delta are Lorentz invariant, but the integrand is not yet written in a relativistic form. In order to do this, we will transform from 2-spinors $|\widehat{\tilde{\mathbf{p}}};\chi\rangle$ to 4-spinors $u^\chi_{\tilde{\mathbf{p}}}$ (as in Sec. 1.2), while simultaneously transforming Pauli matrices to gamma matrices whose Lorentz transformation properties are more transparent. Since we have massless fermions, we chose the Weyl/chiral representation of the gamma matrices, in which,

$$\gamma^5 = \begin{pmatrix} -\sigma^0 & 0 \\ 0 & \sigma^0 \end{pmatrix} \quad , \quad \gamma^\mu = \begin{pmatrix} 0 & \sigma^\mu \\ \bar{\sigma}^\mu & 0 \end{pmatrix} \quad , \quad \sigma^\mu = \left(\sigma^0, \boldsymbol{\sigma}\right) \quad , \quad \bar{\sigma}^\mu = \left(\sigma^0, -\boldsymbol{\sigma}\right) . \tag{3.20}$$

With these definitions, we find that a 4-spinor $\phi = (\phi_1, \phi_2)^T$ satisfies $\gamma^\mu\partial_\mu\phi = 0$, if ϕ_1

[6]Note that the hole actually *does* have chirality $-\chi_i$; there is an additional complex conjugation involved in exchanging the created and annihilated states.

and ϕ_2 satisfy the left- and right-handed Weyl equations respectively. Equation (3.19) can now be written in terms of 4-spinors by introducing positive energy solutions $u_{\tilde{\mathbf{p}}} = (|\widehat{\tilde{\mathbf{p}}}; L\rangle, |\widehat{\tilde{\mathbf{p}}}; R\rangle)^{\mathrm{T}}$, $u^L_{\tilde{\mathbf{p}}} = (|\widehat{\tilde{\mathbf{p}}}; L\rangle, 0)^{\mathrm{T}}$, $u^R_{\tilde{\mathbf{p}}} = (0, |\widehat{\tilde{\mathbf{p}}}; R\rangle)^{\mathrm{T}}$ and $\bar{u}^\chi_{\tilde{\mathbf{p}}} = u^{\chi,\dagger}_{\tilde{\mathbf{p}}}\gamma^0$ since in the particle-hole formalism, both hole and particle have positive energy[7]. We must do further calculations to rewrite the 2×2 Pauli matrices in terms of gamma matrices, in order to determine the correct transformation rules, which differ for the two cases. To that end, we temporarily rename $\chi''^{\mu\,\nu}_{(+)}(\mathbf{q},\omega) \to T^{\mu\,\nu}_{\chi\to\chi}(Q)$ or $I^{\mu\,\nu}_{\chi\to\bar{\chi}}(Q)$ for time-reversal and inversion-symmetric nodes, the final result of which is given in the next chapter by Eq. (4.4) and Eq. (4.6), respectively, in non-relativistic notation in context of the complete formulation of the cross-section. As the methodology for calculating this by using Lorentz invariance is the same for both, albeit the inversion symmetric case is much more difficult, we will only derive the time-reversal symmetric case in Appx. B, and refer the inversion-symmetric case to Ref. [28]

The main point of all this is that $\chi''^{\mu\,\nu}_{(+)}(\mathbf{q},\omega)$ describes a pseudospin susceptibility, i.e., the dynamic response of relativistic Weyl particle-hole pairs in a magnetic field induced by a neutron. The transformation properties of $\chi''^{\mu\,\nu}_{(+)}(\mathbf{q},\omega)$ will be discussed in Ch. 4 when the cross-section is presented, because the cross-section inherits the transformation properties of the susceptibility.

Additionally, this formal discussion of the susceptibility makes it easy to under-

[7]Notice that, here and in Appendix B, the chirality is denoted by L, R for left- and right-handedness, because ± 1 will be reserved for positive and negative energy solutions.

stand the density of states for exciting Weyl fermions. It is clearly the 00-component of a Lorentz 2-rank tensor[8], as is evident from Eq. (3.18) and (3.19), since the density of states for a $\mathrm{M}^{(+)}$ transition in isotropic coordinates reads,

$$D^{(+)}(\tilde{\boldsymbol{\Delta}},\omega) = \frac{1}{(2\pi\hbar)^3}\int \mathrm{d}\tilde{\mathbf{p}}_i \int \mathrm{d}\tilde{\mathbf{p}}_f \;\; \delta(\tilde{\mathbf{p}}-\tilde{\boldsymbol{\Delta}})\,\delta\left(\hbar\omega - \Delta\xi^{\mathrm{w}}\right) . \tag{3.21}$$

Here we shifted the argument to focus on the spherical region in a $(\tilde{\mathbf{q}},\omega)$ plot of the cross-section as illustrated in Fig. 2.2. Equation (3.21) highlights an important fact, that the density of states in isotropic coordinates, $\tilde{\boldsymbol{\Delta}}$, is proportional to the density of states in physical coordinates, $\boldsymbol{\Delta}$, with proportionality factor $|\mathcal{T}|$. This is the physical reason for the normalization of the principal axis transformation Eq. (3.4): $\mathcal{T}$ must be constructed such that it has determinant of one, to ensure that the density of states for exciting Weyl fermions does not change when transforming from physical to isotropic coordinates.

This section completes the derivation of the inelastic neutron cross-section. The formulation of the problem of neutron scattering off Weyl semimetals, basically consisted in mapping the excitations created in the scattering process to a relativistic process. Because the spin of a Weyl fermion is pseudospin, the interaction of the neutron with Weyl fermions takes the form of an emergent magnetic moment, which is

[8]The density of states for exciting Weyl fermions can be calculated analog to the susceptibility of the time-reversal symmetric case in Appx. B. The only difference is that there are no matrix elements.

determined by a scourge of anisotropic g-factors specified by the Weyl semimetal band structure. The scattering rate for neutrons is thus equivalent to the rate of exciting relativistic Weyl fermions with an applied field of a certain polarization determined by g-factors of the neutron-Weyl fermion interaction. Next chapter collects all this information into a concise formulation of the cross-sections for the Weyl fermion scattering channel in experiments.

Chapter 4

Inelastic Cross-section and Formalism

This chapter presents the theoretical neutron cross-sections from scattering off Weyl semimetals in several kinds of experiments. These cross-sections include the Weyl fermion scattering channel only, and the possibility of background scattering channels in the experimentally measured cross-sections will be discussed in Sec. 6.1. The cross-sections presented in this chapter apply if the scattering is between two nodes that are related either by time-reversal or inversion symmetry and are aligned at (or near) the chemical potential. Furthermore, we must assume that the vector $\tilde{\mathbf{v}}_0$ of Eq. (3.8) is negligible. These conditions allow the results to be obtained and interpreted in a relativistic way. Chapter 6 uses these formal cross-sections to make predictions about what information on Weyl fermions can be obtained in

experiments. The formulas presented in this chapter provide the theoretical tools for further interpretation of cross-section data than presented in Ch. 6.

4.1 Total Inelastic Cross-section

First, we will give the total inelastic cross-section for arbitrary, initial, and final neutron polarization, and arbitrary momentum and energy transfer. To be precise, consider an incident neutron of a given momentum $\mathbf{q}_i$ and spin state represented by a spinor $|\tau_i\rangle$. Suppose a detector filters the scattered neutron according to its final momentum and spin eigenvalue $\pm\frac{1}{2}$ along a specific direction and counts only the neutron with eigenvalue $+\frac{1}{2}$, described by the state $|\tau_f\rangle$, say. Then, the counting rate is proportional to the rate of transitions from the initial neutron state $|i_\mathrm{n}\rangle = |\mathbf{q}_i;\tau_i\rangle$ via interactions with the Weyl semimetal defined by the Hamiltonian $H_{0,1} + H_{0,2}$, to the final state $|f_\mathrm{n}\rangle = |\mathbf{q}_f;\tau_f\rangle$. The Weyl semimetal begins in the ground state, $|i_\mathrm{w}\rangle$, and ends in $|f_\mathrm{w}\rangle$ upon absorbing neutron momentum $\mathbf{q} = \mathbf{q}_i - \mathbf{q}_f$ and energy $\hbar\omega$. The total differential cross-section for a M^+ transition is then,

$$\left.\frac{\mathrm{d}^2\sigma^{(+)}(\mathbf{q},\omega)}{\mathrm{d}\Omega\mathrm{d}E_f}\right|_{\tau_i}^{\tau_f} \approx \frac{q_f}{q_i}\left(\frac{m_\mathrm{n}}{2\pi\hbar^2}\right)^2 \frac{\mu_0^2}{2\pi\hbar}\sum_{l,m=1}^{3}\mu_{\perp,l}^{if}\mu_{\perp,m}^{fi}S_{l\,m}^{(+)}(\mathbf{q},\omega)\,, \tag{4.1}$$

where the matrix element of the perpendicular component (with respect to the internode direction) of neutron magnetic moment[1] is $\boldsymbol{\mu}_\perp^{fi} = \langle\tau_f|\boldsymbol{\mu}_\perp|\tau_i\rangle$. The dynamic

[1]The component of $\boldsymbol{\mu}$ that enters the cross-section should really be the component perpendicular to the momentum transfer $\mathbf{q}$, but since we focus on low energy scattering, $|\mathbf{q} - 2\mathbf{k}_0| \ll |2\mathbf{k}_0|$, the

structure factor, Eq. (3.16), is given by,

$$S_{ij}^{(+)}(\mathbf{q},\omega) = \mu_{\mathrm{B}}^2 F_i^{\mu,*} F_j^{\nu} \sigma_{(+)}^{\mu\,\nu}(\mathbf{q},\omega)\,, \tag{4.2}$$

where Roman indices $i,j = 1,2,3$ and Greek indices $\mu,\nu = 0,1,2,3$.

For conventional neutron scattering, the neutrons interact mainly with the spin degrees of freedom and hence $\sigma_{(+)}^{\mu\nu}(\mathbf{q},\omega)/2\hbar$ describes the spin susceptibility. In this case, the states of the Weyl fermions are pseudospin states, so $\boldsymbol{\sigma}$ does not correspond to the spin necessarily. Instead, $\sigma_{(+)}^{\mu\nu}(\mathbf{q},\omega)/2\hbar$ describes the full magnetic susceptibility including both orbital and spin contributions to the magnetic moments, since we determined the magnetization operator in a way that includes all these contributions.

The susceptibility can be calculated by integrating over all possible Weyl particle-hole pairs. At zero temperature, we exploit Lorentz invariance to evaluate this analytically (see Sec. 3.3 and Appx. B). The susceptibility for the scattering process is,

$$\chi_{(+)}''^{\mu\,\nu}(\mathbf{q},\omega) = \sigma_{(+)}^{\mu\,\nu}(\mathbf{q},\omega)/2\hbar\,, \tag{4.3}$$

which is a function of the physical neutron momentum transfer, $\mathbf{q}$, implicitly through $\tilde{\boldsymbol{\Delta}} = \mathcal{T}\boldsymbol{\Delta} = \mathcal{T}(2\mathbf{k}_0 - \mathbf{q})$. For Weyl nodes related by time-reversal symmetry, the chiralities are the same, $\chi_i = \chi_f = \chi$. In this case, the susceptibility Eq. (4.3) is a

error is negligible, about $\hbar\omega/v_{\mathrm{F}}k_0$.

Lorentz invariant rank-2 tensor with components:

$$a^{-1}\chi''^{0\,0}_{(+)}(\mathbf{q},\omega) = |\tilde{\mathbf{\Delta}}|^2\,, \tag{4.4a}$$

$$a^{-1}\chi''^{0\,i}_{(+)}(\mathbf{q},\omega) = a^{-1}\chi''^{i\,0}_{(+)}(\mathbf{q},\omega) = \chi(\hbar\omega/v_{\rm F})\tilde{\Delta}_i\,, \tag{4.4b}$$

$$a^{-1}\chi''^{i\,j}_{(+)}(\mathbf{q},\omega) = \tilde{\Delta}_i\tilde{\Delta}_j + \delta_{i\,j}[(\hbar\omega/v_{\rm F})^2 - |\tilde{\mathbf{\Delta}}|^2]\,, \tag{4.4c}$$

with constant,

$$a = \frac{\pi^2}{3}\frac{V}{v_{\rm F}(2\pi\hbar)^3}. \tag{4.5}$$

For Weyl nodes related by inversion symmetry, the chiralities are opposite, $\chi_i = -\chi_f = \chi$. In this case, the susceptibility Eq. (4.3) transforms differently (see Ref. [28]) for various $\mu,\nu = 0,1,2,3$ and breaks up into three different tensors:

$$a^{-1}\chi''^{0\,0}_{(+)}(\mathbf{q},\omega) = (3/2)[(\hbar\omega/v_{\rm F})^2 - |\tilde{\mathbf{\Delta}}|^2]\,, \tag{4.6a}$$

$$a^{-1}\chi''^{0\,i}_{(+)}(\mathbf{q},\omega) = a^{-1}\chi''^{i\,0}_{(+)}(\mathbf{q},\omega) = 0\,, \tag{4.6b}$$

$$a^{-1}\chi''^{i\,j}_{(+)}(\mathbf{q},\omega) = \delta_{i\,j}[(\hbar\omega/v_{\rm F})^2 + |\tilde{\mathbf{\Delta}}|^2]/2 - \tilde{\Delta}_i\tilde{\Delta}_j + \chi\, i\,\epsilon_{i\,j\,k}\,(\hbar\omega/v_{\rm F})\,\tilde{\Delta}_k\,. \tag{4.6c}$$

Here, $\chi''^{0\,0}_{(+)}$ is a Lorentz scalar. The tensor $\chi''^{i\,j}_{(+)}$ appears not to be Lorentz covariant since it has only spatial indices, but it actually is a usual type of tensor.

Combining Eq. (4.1) and (4.2) with either the time-reversal or inversion-symmetric susceptibility, Eq. (4.4) or (4.6), gives the cross-section for scattering with both a polarized beam and a polarized detector. The susceptibility is expressed in the isotropic

coordinate system obtained from the physical one by applying the transformation $\tilde{\mathbf{\Delta}} = \mathcal{T}\mathbf{\Delta}$. The dynamic structure factor, Eq. (4.2), depends on the parameters $\mathbf{F}^{\mu}$ with $\mu = 0, 1, 2, 3$ which determines the coupling of neutron to Weyl fermions. These are *a priori* unknown without a specific band structure. Chapter 6 explains that properties of Weyl fermions can be measured independently of knowing these parameters. However, the coupling can be calculated by using Eq. (3.15) if a material's band structure is known. Having such information prior to an experiment will be an advantage to the experimentalist since this fully determines the Weyl fermion scattering cross-section, Eq. (4.1), for all neutron momentum and energy transfer.

The structure factor $S_{l\,m}(\mathbf{q}, \omega) = S^{(+)}_{l\,m}(\mathbf{q}, \omega) + S^{(-)}_{l\,m}(\mathbf{q}, \omega)$ considered as a function of neutron momentum transfer $\mathbf{q} = \pm 2\mathbf{k}_0 - \mathbf{\Delta}$, will be concentrated in small spheres centered at $\pm 2\mathbf{k}_0$, as illustrated in Fig. 2.2, *only* if the nodes are in the isotropic form, Eq. (2.1), prior to measurement. However, if nodes are in the anisotropic form, Eq. (3.1), then $S_{l\,m}(\mathbf{q}, \omega)$ will be ellipsoids for a fixed energy transfer $\hbar\omega$. A linear transformation $\tilde{\mathbf{q}} = \mathcal{T}\mathbf{q}$ is necessary to transform these ellipsoidal regions into spheres centered on $\pm 2\tilde{\mathbf{k}}_0$. Thereby $S_{l\,m}(\tilde{\mathbf{q}}, \omega)$ plotted in isotropic $\tilde{\mathbf{q}}$ coordinates will look like Fig. 2.2 with $\tilde{\mathbf{\Delta}}$ replacing $\mathbf{\Delta}$. Section 3.1.1.1 explained how to find the principal axis transformation $\mathcal{T}$ *experimentally*, and this procedure is illustrated for a toy model in Figs. 5.2 and 5.3. Once having obtained $\mathcal{T}$ from a measurement, one has also obtained the first information about Weyl fermions: their anisotropic dispersion, and thereby the form of the Weyl equation (3.1) describing the Weyl nodes involved in

the scattering process. The interiors of the spherical regions of $S_{l\,m}(\tilde{\mathbf{q}},\omega)$ contain the scattering channel from Weyl fermions. To focus on the spherical region for an M^{+} transition, it is convenient to describe the cross-section in a coordinate system of $\tilde{\mathbf{\Delta}}$.

4.1.1 Unpolarized Detector

In realistic neutron scattering experiments, the initial neutron beam of $N \gg 1$ neutrons has an average polarization vector $\mathbf{P}$, which can be described by a density matrix $\boldsymbol{\rho} = (\tau_0 + \mathbf{P}\cdot\boldsymbol{\tau})/2$, where $\boldsymbol{\tau}$ is a vector of Pauli matrices and τ_0 is the identity matrix in neutron spin basis. The inelastic cross-section, Eq. (4.1), of the scattered beam measured by an *unpolarized* detector is given by [69, 76],

$$\frac{\mathrm{d}^2\sigma^{(+)}(\mathbf{q},\omega;\mathbf{P})}{\mathrm{d}\Omega\mathrm{d}E_f} = \frac{q_f}{q_i}\left(\frac{gr_0}{4}\right)^2\left[\Sigma^{(+)}(\mathbf{q},\omega) + \mathbf{P}\cdot\mathbf{\Sigma}^{(+)}(\mathbf{q},\omega)\right],$$

where g is the neutron g-factor and r_0 is the classical electron radius, and

$$\begin{aligned}
\Sigma^{(+)}(\mathbf{q},\omega) &\equiv \left\langle \mathbf{M}_{\perp}^{(-)}(-\mathbf{q},-\omega)\,\cdot\,\mathbf{M}_{\perp}^{(+)}(\mathbf{q},\omega)\right\rangle/2\pi\hbar\mu_{\mathrm{B}}^2\,,\\
&= \mathbf{F}_{\perp}^{\mu,*}\cdot\mathbf{F}_{\perp}^{\nu}\chi''^{\,\mu\,\nu}_{(+)}(\mathbf{q},\omega)/\pi\,, \qquad (4.7a)\\
\mathbf{\Sigma}^{(+)}(\mathbf{q},\omega) &\equiv i\left\langle \mathbf{M}_{\perp}^{(-)}(-\mathbf{q},-\omega)\times\mathbf{M}_{\perp}^{(+)}(\mathbf{q},\omega)\right\rangle/2\pi\hbar\mu_{\mathrm{B}}^2\,,\\
&= i\mathbf{F}_{\perp}^{\mu,*}\times\mathbf{F}_{\perp}^{\nu}\chi''^{\,\mu\,\nu}_{(+)}(\mathbf{q},\omega)/\pi\,. \qquad (4.7b)
\end{aligned}$$

The effective couplings $\mathbf{F}_{\perp}^{\mu,*} \cdot \mathbf{F}_{\perp}^{\nu}$ and $\mathbf{F}_{\perp}^{\mu,*} \times \mathbf{F}_{\perp}^{\nu}$ select which components of the pseudospin susceptibility $\chi''^{\mu\,\nu}_{(+)}(\mathbf{q},\omega)$ are measured by neutron scattering. They are somewhat analogous to a polarizer for light - just as light with a certain electric field strength is modulated when it is rotated relative to a polarizer, the signal of the Weyl fermions in neutron scattering oscillates when the direction of $\mathbf{q}$ is rotated relative to $\mathbf{F}_{\perp}^{\mu,*} \cdot \mathbf{F}_{\perp}^{\nu}$, and/or $\mathbf{F}_{\perp}^{\mu,*} \times \mathbf{F}_{\perp}^{\nu}$, even though it is the tensor $\chi''^{\mu\,\nu}_{(+)}(\mathbf{q},\omega)$ which rotates.

The $(\mu,\nu) = (0,0)$ component of the effective couplings gives rise to no angular $\tilde{\mathbf{\Delta}}$-dependence in the cross-section. However, the remaining Hermitian $(i,j = 1,2,3)$ parts do and can be written in their spectral decompositions,

$$\mathbf{F}_{\perp}^{i,*} \cdot \mathbf{F}_{\perp}^{j} = \sum_{l=1}^{2} \alpha_l \, \hat{\mathbf{a}}_l^{j} \, \hat{\mathbf{a}}_l^{i*} , \tag{4.8a}$$

$$\mathbf{F}_{\perp}^{i,*} \times \mathbf{F}_{\perp}^{j} = -i\hat{\mathbf{k}}_0 \sum_{l=1}^{2} \beta_l \, \hat{\mathbf{b}}_l^{\,i} \, \hat{\mathbf{b}}_l^{\,j*} , \tag{4.8b}$$

where α_l and $\hat{\mathbf{a}}_l$ are the l^{th} eigenvalue and normalized eigenvector of the matrix $\mathbf{F}_{\perp}^{i,*} \cdot \mathbf{F}_{\perp}^{j}$. Likewise, β_l and $\hat{\mathbf{b}}_l$ are the l^{th} eigenvalue and eigenvector of the matrix $i\hat{\mathbf{k}}_0 \cdot \mathbf{F}_{\top}^{i,*} \times \mathbf{F}_{\top}^{j}$. To prove these, we used the fact that $\mathbf{F}_{\perp}^{i} \cdot \hat{\mathbf{k}}_0 = 0$ for each i, hence $\det[\mathbf{F}^i \cdot \hat{\mathbf{j}}] = 0$ and therefore Eq. (4.8a) and (4.8b) will have a zero eigenvalue. Notice that in Eq. (4.8a) there is a direction, $\hat{\mathbf{a}}_3 = \hat{\mathbf{a}}_1 \times \hat{\mathbf{a}}_2$, in neutron spin space which is not coupled to pseudospin space. Likewise, there exists the direction, $\hat{\mathbf{b}}_3 = \hat{\mathbf{b}}_1 \times \hat{\mathbf{b}}_2$, in Eq. (4.8b). For example, the coupling most closely resembling purely conventional magnetic scattering is $\mathbf{F}^0 = 0$ and $\mathbf{F}^i \cdot \hat{\mathbf{j}} = \delta_{ij}$, which for a material with internode

direction $\hat{\mathbf{k}}_0 = \hat{\mathbf{z}}$, yields an effective coupling for a cross-section with an unpolarized detector that is,

$$\mathbf{F}_\perp^{i,*} \cdot \mathbf{F}_\perp^j = \begin{pmatrix} (F_x^x)^2 & 0 & 0 \\ 0 & (F_y^y)^2 & 0 \\ 0 & 0 & 0 \end{pmatrix}_{ij} . \tag{4.9}$$

By the spectral decomposition, Eq. (4.8a), this has eigenvalues $\alpha_1 = (F_x^x)^2$ and $\alpha_1 = (F_y^y)^2$ with associated eigenvectors $\hat{\mathbf{a}}_1 = \hat{\mathbf{x}}$ and $\hat{\mathbf{a}}_2 = \hat{\mathbf{y}}$, and a direction $\hat{\mathbf{a}}_3 = \hat{\mathbf{z}}$ where neutron spin is not coupled to pseudospin.

The formal cross-sections presented in this chapter reveal several conceptually and experimentally interesting cases, which we will discover in Ch. 6. In that chapter, we will illustrate both ways of thinking about the effective couplings Eq. (4.8) i.e., both as a matrix like Eq. (4.9) and its spectral decomposition.

Chapter 5

Toy Model Weyl Semimetal

In this chapter, we will illustrate most of the concepts introduced in Ch. 3 by using a simple toy model of an inversion invariant, time-reversal symmetry-breaking Weyl semimetal. This model does not represent a model of a realistic Weyl semimetal, so we do not discuss the stability of its Weyl semimetal phase. Section 5.1 and 5.2 illustrate how to transform the Hamiltonian from physical to isotropic coordinates. Section 5.3 illustrates how to measure the principal axis transformation $\mathcal{T}$, Eq. (3.4), from the region of nonzero scattering intensity. Most importantly, Sec. 5.4 explains how to derive the coupling, Eq. (3.15), of neutrons to Weyl fermions. As a proof of principle, this model illustrates that the coupling can be much larger than the bare coupling.

5.1 Physical Coordinates

In section 1.3.1, a model of an inversion invariant, time-reversal symmetry-breaking Weyl semimetal was introduced. That model [50, 51] consisted of a heterostructure of topological insulator slabs interlaced with normal insulator slabs. When the topological insulator slabs were doped by magnetic impurities a Weyl semimetal phase was generated. In this chapter, we introduce a toy model of that more realistic model. As the topological-normal insulator heterostructure model was explained in length, we will keep the discussion of this toy model brief.

A toy model of the heterostructure can be obtained by starting with a material that is tuned to the transition between a topological and normal insulator, and by introducing magnetic impurities. In a time-reversal symmetric material that is tuned to the transition point, the gap is closed thus producing 3D Dirac points, which we suppose to be at zero momentum. The Dirac points are described by a Hamiltonian $H_{3\,\mathrm{D}} = v_{\mathrm{D}}\mathbf{k}\cdot\boldsymbol{\sigma}\tau^z$, which is the massless limit of the Dirac Hamiltonian Eq. (1.1). These may be regarded as two degenerate Weyl nodes, labeled by $\tau^z = \pm 1$, having opposite chiralities, also given by τ_z. The $\boldsymbol{\sigma}$ corresponds to the spin of the state, while τ labels different bands. As one moves away from the topological transition, a hybridization term appears $H_\delta = \delta\sigma^0\tau^x$ that couples the nodes with strength δ and produces a gap. Returning to the transition point and introducing magnetic impurities $H_{\mathrm{Z}} = -m\sigma^z\tau^0$ that are assumed to order ferromagnetically along the z-direction and interact equally with both orbitals breaks time-reversal symmetry

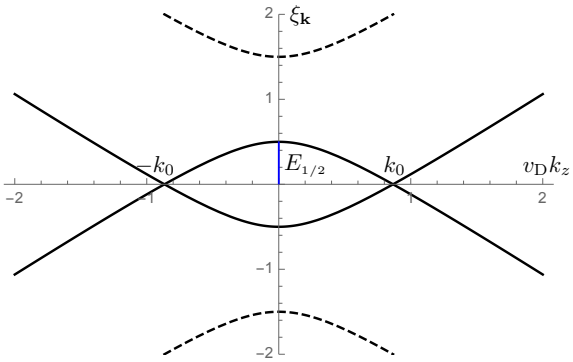

Figure 5.1: Energy spectrum of four-band model for $|\delta|/m = 0.5$. The half-energy gap (blue line) $E_{1/2} = m - |\delta|$ is indicated.

and separates the nodes in momentum space. If the hybridization term is present as well and not too large, then it will not open a gap and the Weyl points will remain stable as long as $m > |\delta|$, assuming that $m > 0$. This yields a minimal time-reversal breaking and inversion invariant Weyl semimetal four-band toy model whose Hamiltonian $H_0^4 = H_{3\,\mathrm{D}} + H_\delta + H_{\mathrm{Z}}$ has nodes at $\mathbf{k}_{0,2} = -\mathbf{k}_{0,1} = k_0\hat{\mathbf{z}}$, where $v_{\mathrm{D}}k_0 = \sqrt{m^2 - \delta^2}$, and its spectrum is,

$$\xi_0^4(\mathbf{k}) = \pm\sqrt{(v_{\mathrm{D}}|\mathbf{k}|)^2 + m^2 + \delta^2 \pm 2m\sqrt{\delta^2 + (v_{\mathrm{D}}k_z)^2}}\,, \tag{5.1}$$

which is plotted as a function of k_z in Fig. 5.1 along $k_x = k_y = 0$.

Each node $i = 1, 2$ has a degenerate subspace $D_i = \{|s; \mathbf{k}_{0,i}\rangle\}$ enumerated by pseudospin label $s = \pm$. Although the low energy sector of the Hilbert space consists of four states, only the two states within a given degenerate subspace are required to be orthonormal. The Hamiltonian is inversion symmetric, i.e., $PH_0^4(\mathbf{k})P^{-1} = H_0^4(-\mathbf{k})$, where inversion is $P = \sigma^0\tau^x$. As explained in Sec. 3.1.1, in order to ensure the effective Hamiltonian can be transformed into an isotropic form, the in-

version symmetry must act as the identity–this *is* true within the space of degenerate states since $P|s,\mathbf{k}_1\rangle = |s,\mathbf{k}_2\rangle$. The degenerate states are $|+;\mathbf{k}_{0,1}\rangle = (u_-,u_+,0,0)^{\mathrm{T}}$, $|-;\mathbf{k}_{0,1}\rangle = (0,0,u_-,u_+)^{\mathrm{T}}$ and $P|s;\mathbf{k}_{0,1}\rangle$ normalized such that $|u_-|^2+|u_+|^2=1$ with $u_\pm = (1/\sqrt{2})\sqrt{1\pm\sqrt{1-(\delta/m)^2}}$. Following the guidelines of Sec. 3.2.1, we find the effective low energy two-band model,

$$H_{0,i}(\mathbf{k}) = \chi_i \sigma_l v^{(i)}_{l\,m} p_m \quad , \quad \mathbf{p} = \mathbf{k} - \mathbf{k}_{0,i}\,, \tag{5.2}$$

which has the form Eq. (3.1) with $v^{(1)} = -v^{(2)} = v_{\mathrm{D}}\,\mathrm{diag}(+1,+1,-\sqrt{\Lambda})$, where $\Lambda = 1-(\delta/m)^2$, $\mathbf{v}_0^{(i)} = \mathbf{0}$ and chiralities $\chi_2 = -\chi_1 = 1$.

Notice, that Eq. (5.2) has not yet been factored to the form Eq. (3.1). The $v^{(i)}$ is deceptively simple and invites us to simply write $v^{(i)} = v_{\mathrm{D}}\lambda^{(i)}$, in which case the dispersion is $\xi_i(\mathbf{k}) = \pm v_{\mathrm{D}}\sqrt{p_x^2+p_y^2+(\sqrt{\Lambda}p_z)^2}$, meaning that the velocity $v_{\mathrm{D}}\sqrt{\Lambda}$ along z-direction is slower than v_{D} along the x and y-directions. Hence, upon rescaling momenta to isotropic coordinates $\tilde{\mathbf{p}} = \mathcal{T}\mathbf{p}$ with $\mathcal{T}_{ab} = d_a\sigma^0_{ab}$ (Einstein summation convention suspended) and $\mathbf{d} = (1,1,\sqrt{\Lambda})^{\mathrm{T}}$ will transform the anisotropic dispersion into isotropic form $\xi_i(\tilde{\mathbf{p}}) = \pm v_{\mathrm{D}}|\tilde{\mathbf{p}}|$. This factorization would be allowed in many instances, but not in ours: $|\mathcal{T}| \neq 1$ in the Weyl semimetal phase region.

Recall that the factorization of $v^{(i)}$ relative to the isotropic speed $\tilde{v}_{\mathrm{D}}$, i.e., $v^{(i)} = \tilde{v}_{\mathrm{D}}\lambda^{(i)}$, is arbitrary up to a principal axis transformation matrix $\mathcal{T}$, Eq. (3.4). The

requirement $|\mathcal{T}| = 1$ restricts $|\lambda^{(i)}| = 1$ and therefore,

$$\tilde{v}_{\mathrm{D}} = |v^{(i)}|^{1/3} = v_{\mathrm{D}}\Lambda^{1/6}\,. \tag{5.3}$$

The correct factorization of the effective low energy Hamiltonian of the two Weyl nodes is therefore,

$$H_{0,i}(\mathbf{k}) = \chi_i \tilde{v}_{\mathrm{D}} \sigma_l \lambda^{(i)}_{l\,m} p_m \quad , \quad \mathbf{p} = \mathbf{k} - \mathbf{k}_{0,i}\,, \tag{5.4}$$

with new speed given by Eq. (5.3), and dimensionless anisotropy matrix $\lambda^{(1)} = -\lambda^{(2)} = \mathrm{diag}(+\Lambda^{-1/6}, +\Lambda^{-1/6}, -\Lambda^{1/3})$. The anisotropic dispersion is,

$$\xi_i(\mathbf{k}) = \pm\tilde{v}_{\mathrm{D}}\sqrt{(\Lambda^{-1/6}p_x)^2 + (\Lambda^{-1/6}p_y)^2 + (\Lambda^{1/3}p_z)^2}\,. \tag{5.5}$$

5.2 Isotropic Coordinates

The Weyl nodes, Eq. (5.4), can be orthogonally diagonalized simultaneously by $\lambda^{(2)} = ODR^{\mathrm{T}}$ with $R^{\mathrm{T}} = R^{-1}$ and $O^{\mathrm{T}} = O^{-1}$. The singular values d_j of $\lambda^{(2)}$ are the square roots of the eigenvalues of the velocity matrix $\lambda^{(2),\mathrm{T}}\lambda^{(2)} = \mathrm{diag}(\Lambda^{-1/3}, \Lambda^{-1/3}, \Lambda^{2/3})$, so $D_{ij} = d_j\sigma^0_{ij}$ (Einstein summation convention suspended) with elements $d_1 = d_2 = \Lambda^{-1/6} \geq d_3 = \Lambda^{1/3} > 0$. The right singular eigenvectors $\hat{\mathbf{v}}_j$ of $\lambda^{(2)}$ are the eigenvectors of $\lambda^{(2),\mathrm{T}}\lambda^{(2)}$ which form a basis for $\mathbb{R}^3$. Thus, $R = [\hat{\mathbf{v}}_1, \hat{\mathbf{v}}_2, \hat{\mathbf{v}}_3] = \sigma^0$. The left sin-

gular eigenvectors $\hat{\mathbf{o}}_j$ of $\lambda^{(2)}$ are $\hat{\mathbf{o}}_j = (1/d_j)\lambda^{(2)}\hat{\mathbf{v}}_j$ forms $O = [\hat{\mathbf{o}}_1, \hat{\mathbf{o}}_2, \hat{\mathbf{o}}_3]$. The linear combination $\sigma_i O_{ia}$ can be written as a rotation of a Pauli matrix σ_a by a unitary matrix U, i.e., $O_{ai}\sigma_i = U^\dagger \sigma_a U$, which in this case is a π rotation around the z-axis, so $U = e^{-i\frac{\pi}{2}\boldsymbol{\sigma}\cdot\hat{\mathbf{z}}}$. Changing the basis of pseudospin yields,

$$H_{0,2}(\mathbf{p}) \to H_{0,2}(\tilde{\mathbf{p}}) = \chi_2 \tilde{v}_{\mathrm{D}} \boldsymbol{\sigma} \cdot \tilde{\mathbf{p}}\,, \tag{5.6}$$

which transforms both nodes to the standard isotropic form with opposite chiralities $\chi_2 = -\chi_1 = 1$. In other words, the effective Hamiltonian Eq. (5.4) is transformed into isotropic form Eq. (5.6) with coordinates $\tilde{\mathbf{p}} = \mathcal{T}\mathbf{p}$ with $\mathcal{T}_{ab} = d_a \sigma^0_{ab}$ (Einstein summation convention suspended) and $\mathbf{d} = (\Lambda^{-1/6}, \Lambda^{-1/6}, \Lambda^{1/3})^{\mathrm{T}}$. Finally, the anisotropic dispersion, Eq. (5.5), becomes isotropic,

$$\xi_i(\tilde{\mathbf{p}}) = \pm \tilde{v}_{\mathrm{D}} |\tilde{\mathbf{p}}|\,, \tag{5.7}$$

upon rescaling momenta by $\tilde{p}_a = p_a d_a$ with new isotropic speed Eq. (5.3).

5.3 Measuring the Principal Axis Transformation $\mathcal{T}$

In the two previous sections, we saw again how one theoretically derives the principal axis transformation $\mathcal{T}$ that transforms the effective anisotropic Hamilton to an isotropic form. In a real experiment, one has to construct $\mathcal{T}$ from a measurement. This was explained in Sec. 3.1.1.1, but here we will use the toy model as an example. Notice that this measurement constitutes a measurement of the Weyl nodes' dispersions, i.e., the principal axes and velocities of the anisotropic nodes.

From an experiment, one simply looks at the region of $\mathbf{q}, \omega$-space in which the cross-section is nonzero. In other words, this is the region of density of states of the Weyl excitations, except for intensity modulations within this region due to spin-momentum locking of the Weyl fermions. We know from Ch. 2 that, if nodes are isotropic, then the plot of the cross-section, at a fixed energy transfer $\hbar\omega$ as a function of the neutron momentum transfer $\mathbf{q}$, will show two spheres of radii $\hbar\omega/v_{\mathrm{F}}$ centered at $\pm 2\mathbf{k}_0$ as in Fig. 2.2, corresponding to the two allowed $\mathrm{M}^{\pm}$ transitions (see Fig. 2.1). However, this toy model Hamiltonian, Eq. (5.4), is anisotropic. One would still see two nonzero regions centered at $\pm 2\mathbf{k}_0$, but they would be ellipsoids described by Eq. (3.7b). Let us focus on the region corresponding to the M^{+} transition, which as

a function of neutron momentum transfer $\mathbf{q}$ is described by,

$$\hbar\omega \geq \sqrt{\mathbf{\Delta}^{\mathrm{T}} v^2 \mathbf{\Delta}} \quad , \quad v^2 = \tilde{v}_{\mathrm{D}}^2 \lambda^{(2),\mathrm{T}} \lambda^{(2)} \, , \tag{5.8}$$

where $\mathbf{\Delta} = 2\mathbf{k}_0 - \mathbf{q}$, and is illustrated in Fig. 5.2.

From measuring the directions and magnitudes of this ellipsoid's principal axes, one measures the eigenvectors and square root eigenvalues of the velocity matrix v^2. In the case of this toy model, the principal axes are $\hat{\mathbf{v}}_1 = \hat{\mathbf{x}}$, $\hat{\mathbf{v}}_2 = \hat{\mathbf{y}}$ and $\hat{\mathbf{v}}_3 = \hat{\mathbf{z}}$, corresponding to the two minor axes and major axis. The lengths from the center $2\mathbf{k}_0$ to the edge will be measured to be $\hbar\omega/\tilde{v}_{\mathrm{D}} d_1$, $\hbar\omega/\tilde{v}_{\mathrm{D}} d_2$ and $\hbar\omega/\tilde{v}_{\mathrm{D}} d_3$, where $d_1 = d_2 = \Lambda^{-1/6}$ and $d_3 = \Lambda^{1/3}$. From these measurements, one constructs the coordinate rotation matrix $R = [\hat{\mathbf{v}}_1, \hat{\mathbf{v}}_2, \hat{\mathbf{v}}_3]$ and diagonal "stretching" matrix with elements $\mathbf{d} = (d_1, d_2, d_3)^{\mathrm{T}}$ ordered as $d_1 = d_2 \geq d_3 > 0$. Thereby, one has experimentally measured the principal axis transformation, Eq. (3.4), determined to be $\mathcal{T} = R^{\mathrm{T}} D$ with $D_{a\,b} = d_a \sigma^0_{a\,b}$ (Einstein summation convention suspended). To interpret the cross-section, it will be necessary to transform it from physical coordinates, $\mathbf{q}$, to isotropic coordinates, $\tilde{\mathbf{q}} = \mathcal{T}\mathbf{q}$. To check $\mathcal{T}$, one transforms the cross-section into $\tilde{\mathbf{q}}$. If it is correct, the ellipsoidal regions distort into spheres centered at $2\tilde{\mathbf{k}}_0$, illustrated in Fig. 5.3, and satisfy $|\mathcal{T}| = 1$.

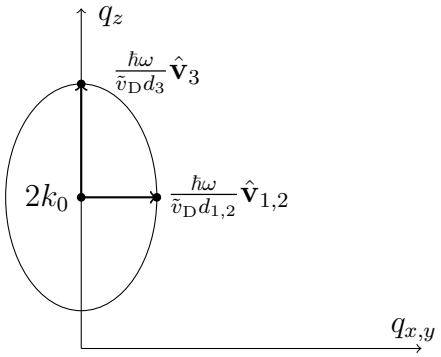

Figure 5.2: Region of nonzero scattering in physical coordinates $\mathbf{q}$ for fixed neutron energy $\hbar\omega$.

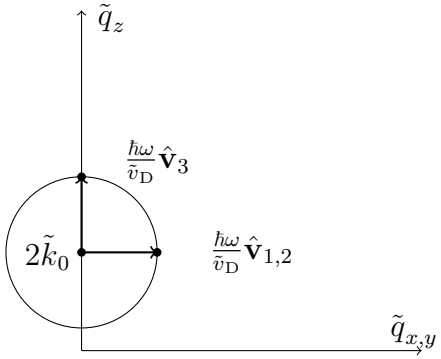

Figure 5.3: Transformed region of nonzero scattering. The ellipsoidal region in $\mathbf{q}, \omega$-space, see Fig. 5.2, has been reshaped to a sphere in isotropic coordinates $\tilde{\mathbf{q}} = \mathcal{T}\mathbf{q}$.

5.4 Coupling of Neutron to Weyl Fermions

As we consider only scattering within the low energy sector of the nodes, the coupling of neutrons to Weyl fermions Eq. (3.14) is determined by evaluating the matrix elements of the $H_{\mathbf{A}}$ interaction exactly at the Weyl node positions, i.e., evaluating the left-hand side of Eq. (3.11) for the eigenfunctions of our model with $\mathbf{p}_1 = \mathbf{p}_2 = \mathbf{0}$ (i.e., $\mathbf{p}_i = \mathbf{k} - \mathbf{k}_{0,i}$ for $i = 1, 2$), and comparing to the $H_{\mathbf{B}}$ interaction using the effective description, Eq. (3.14).

To evaluate the left-hand side of this matrix equation, we introduce the current operator $\boldsymbol{\mathcal{J}} = ev_{\rm D}\boldsymbol{\sigma}\tau^z$, obtained from H_0^4 by a minimal substitution. On the right-hand side, in the effective model, the spin operators σ^i are necessarily redefined to act on the two-dimensional subspace, e.g., $\sigma^z|s;\mathbf{k}_{0,i}\rangle = s|s;\mathbf{k}_{0,i}\rangle$, whereas the eigenstates are not eigenfunctions of the original σ^z. Solving this matrix equation for $\mathbf{F}^\mu$ gives

Eq. (3.15). Consequently, $\mathbf{F}^{\mu}_{\perp}$ has nonzero components $F^{x}_{\perp,x}$ and $F^{y}_{\perp,y}$, which both have the same magnitude,

$$F^{x}_{\perp,x} = \frac{e v_{\mathrm{D}}}{\mu_{\mathrm{B}}} \frac{\delta}{m} \frac{\hbar}{|2\mathbf{k}_0|} = \pm \frac{m_{\mathrm{e}} v_{\mathrm{D}}^2}{v_{\mathrm{D}} k_0} \frac{(v_{\mathrm{D}} k_0)^2 - E_{1/2}^2}{(v_{\mathrm{D}} k_0)^2 + E_{1/2}^2}, \tag{5.9}$$

where $E_{1/2} = m - |\delta| \leq v_{\mathrm{D}} k_0$ is the half-energy gap at $\mathbf{k} = \mathbf{0}$ indicated in Fig. 5.1. The second expression is written in terms of parameters of the bands' dispersion; the sign depends on the sign of δ which cannot be seen from the dispersion.

For example, for a Fermi velocity of order[1] $v_{\mathrm{D}} = c/300$, where c is the speed of light, the magnetic moment per Bohr magneton for the internode coupling, i.e., its $\frac{g}{2}$-factor, is plotted in Fig. 5.4 as a function of node position and half-energy gap. Hence, the coupling of a neutron to nodes is comparable to, smaller, or even much larger than that of the electron and may diverge upon approaching the topological phase transition. The cross-section will be estimated in the Sec. 6.1. The above features hold, at least for this toy model which does not represent a realistic model. However, these features could be more generic in nature and thus present in real Weyl semimetals, but this question is left unanswered here. Alternatively, some Weyl materials will be found that can actually be described as topological insulators with magnetic impurities.

[1]For most Weyl semimetal materials realized so far, a velocity of order $v_{\mathrm{D}} = c/300$ is typical. At least Ref. [81] is an exception.

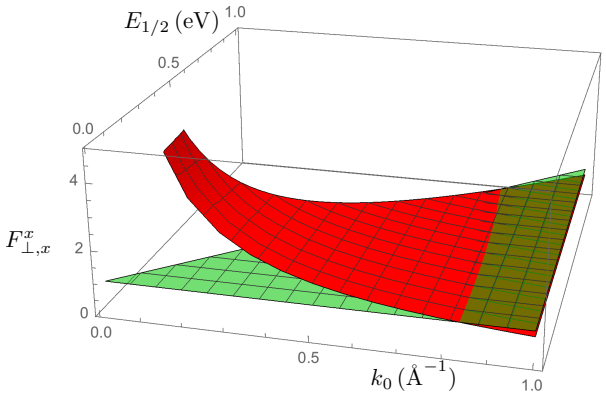

Figure 5.4: Coupling of neutron to Weyl fermions. The coupling, Eq. (5.9), for $v_{\rm D} = c/300$ is plotted (red) as a function of node position k_0 and half-energy gap $E_{1/2}$ of spectrum in Fig. 5.1. The bare coupling of neutron to electrons, i.e., $\frac{1}{2} = 1$, is the (green) plane.

Chapter 6

Experimental Predictions and Interpretations

Chapter 4 summarized the theory needed to understand, interpret, and predict features of the cross-sections to be measured in experiments. The scattering process is distinguished by whether the symmetry relation between the two nodes involved is time-reversal or inversion. While the density of states is the same for either type of symmetry, the cross-sections differ, for two reasons. First, the chiralities are different in the two cases and hence the relativistic susceptibilities have different forms, see Eq. (4.4) and (4.6). Second, the symmetry constraints on the coupling between neutrons and Weyl nodes are different for time-reversal and inversion symmetry. Appendix A shows that,

$$\mathbf{F}^0 = \mathbf{0} \quad , \quad \mathbf{F}^j \in \mathbb{C}^3 \text{ with } j = 1, 2, 3\,, \tag{6.1}$$

for time-reversal symmetric nodes, whereas,

$$\mathbf{F}^{\mu} \in \mathbb{R}^3 \text{ with } \mu = 0, 1, 2, 3\,, \tag{6.2}$$

for inversion symmetric nodes.

In this chapter, we will interpret the cross-section for two kinds of measurements: an unpolarized detector (Sec. 6.2 and 6.3) and a polarized detector (Sec. 6.4). Although there are many parameters describing the coupling of neutrons to Weyl fermions (see Eq. (6.1) and (6.2)), we will see that there are several theoretically interesting predictions. Already at the level of an unpolarized detector (Sec. 6.2) it is possible to observe spin-momentum locking in the cross-section for an experiment with an unpolarized incident neutron beam. This is remarkable given that the coupling is *a priori* arbitrary and unknown, and furthermore, since the neutron spin states are unresolved. If the incident beam is polarized, it is possible to measure the chirality for inversion symmetric nodes only if the couplings are known. Even when the couplings are unknown, it is still possible to determine the chiralities of the Weyl fermions as will be explained in Sec. 6.4, however a polarized detector is required. The scattering region has a discontinuous edge (Sec. 6.1), which is a strong signature of scattering between Weyl nodes that are transformed into Lorentz invariant form. A feature of this edge (Sec. 6.3) is that the cross-section has a pattern reflecting scattering Weyl fermions.

The predictions and interpretations of the cross-sections are most likely not exhaustive. Some of these may not be the most experimentally useful ways to identify properties of, or characterize, Weyl nodes. However, we utilize them as proofs of principles that all of the conceptual obstacles mentioned in Ch. 2 about measuring Weyl fermions can be circumvented. Furthermore, all the predictions assume that Weyl fermion scattering is the only channel in the total measured cross-section, or rather, that background channels have been eliminated in the region of Weyl fermion scattering. However, in any real experiment, background channels of various kinds will be present. We begin in Sec. 6.1 discussing the density of states of Weyl excitations to estimate the strength of the cross-section for the Weyl fermion scattering channel that we are interested in. Background channels will be discussed on general grounds, as these depend highly on the compound at hand.

6.1 Scattering Channels: Weyl Fermion vs. Background

The rate of neutron scattering depends on which electron-hole pairs can be produced in the material, which in turn is determined by the density of states of Weyl excitations and the matrix element for creating the particle-hole pair. Here, we begin by describing the density of states, which helps us to understand the intensity of the cross-section. Section 6.2 returns to the matrix elements of the interaction, which are

responsible for the polarization of neutrons.

The density of states of excitations is defined as an integral over all internal states that conserve energy and momentum for the M^+ transition, i.e., Eq. (3.21). The constant energy contour for particle-hole pairs, plotted in Fig. 6.1, has a simple geometric description. The momentum transfer is a point displaced from the origin by $\tilde{\mathbf{\Delta}}$. If the initial electron momentum is represented by a point P displaced from the origin by $\tilde{\mathbf{p}}_i$, then the *final* momentum $\tilde{\mathbf{p}}_f = \tilde{\mathbf{p}}_i - \tilde{\mathbf{\Delta}}$ is the vector from $\tilde{\mathbf{\Delta}}$ to P, according to conservation of momentum $\delta(\tilde{\mathbf{p}} - \tilde{\mathbf{\Delta}})$ which is the generalization of conservation of momentum for isotropic nodes (see Sec. 2.1) to anisotropic nodes. The change in energy is $v_{\mathrm{F}}(|\tilde{\mathbf{p}}_f| + |\tilde{\mathbf{p}}_i|)$, so conservation of energy forces P to lie on a prolate ellipsoid with foci at $\mathbf{0}$ and $\tilde{\mathbf{\Delta}}$. When scattering is exactly from one node to the other, i.e., $|\tilde{\mathbf{\Delta}}| = 0$, the ellipsoid turns into a sphere. For maximum momentum transfer, i.e., $|\tilde{\mathbf{\Delta}}| = \hbar\omega/v_{\mathrm{F}}$, the ellipsoid degenerates into a line segment connecting the two foci. Hence, the region of nonzero density of states is defined by $|\tilde{\mathbf{\Delta}}| \leq \hbar\omega/v_{\mathrm{F}}$ as we already argued in Eq. (3.7a). Within this region, the density of states is found[1] to be,

$$D^{(+)}(\tilde{\mathbf{\Delta}}, \omega) = \frac{\pi}{2v_{\mathrm{F}}(2\pi\hbar)^3}[(\hbar\omega/v_{\mathrm{F}})^2 - (1/3)|\tilde{\mathbf{\Delta}}|^2]\,. \tag{6.3}$$

Hence, the density of states of internode scattering scales as square of the transferred

[1]The calculation is the same as that of the susceptibility for time-reversal invariant nodes in Appx. B except that there is no matrix element.

energy, like the density of states of a single node.

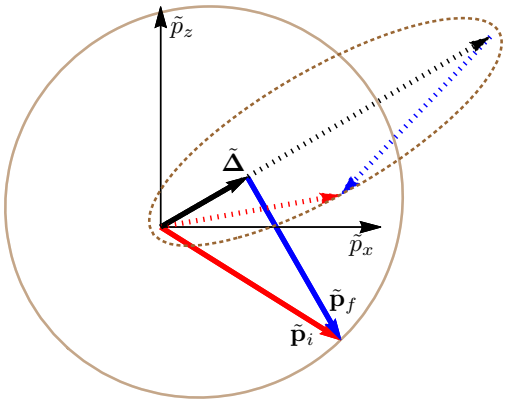

Figure 6.1: Contour of constant energy transfer $\hbar\omega$ for Weyl excitations produced in a scattering event: A prolate spheroid (brown line) in the $\tilde{p}_x, \tilde{p}_z$-plane with symmetry axis (black arrow) along $\tilde{\mathbf{\Delta}}$ and foci at origin of initial $\tilde{\mathbf{p}}_i$ (red arrow) and final $\tilde{\mathbf{p}}_f$ (blue arrow) excitations for a given $|\tilde{\mathbf{\Delta}}|$. Solid lines are for $|\tilde{\mathbf{\Delta}}| = 0.25\hbar\omega/v_\mathrm{F}$, and dashed lines are for $|\tilde{\mathbf{\Delta}}| = 0.95\hbar\omega/v_\mathrm{F}$.

The scattering cross-section scales like the density of states of excitations, which can be problematic, since experiments have to be restricted to a small energy window where bands are dispersing linearly. In particular, the momentum transfer can be at most of order $|\mathbf{k}_0|$ since beyond that distance from one Weyl node, the other node's Weyl Hamiltonian becomes a better approximation as illustrated in Fig. 1.3. However, the strength of the cross-section is proportional to the effective coupling (see Eq. (4.8)), which can be larger than the bare coupling to an electron. Consequently, the low density of states at small energies can be compensated for by the coupling being larger than the usual g-factor of an electron. To illustrate this, we employed a Weyl semimetal toy model in Sec. 5.4. In this model, the g-factors $\mathbf{F}^\mu$ are enhanced and even diverge as the spacing $2k_0$ between the Weyl nodes approaches zero. As the scattering region is at most of order $|\mathbf{k}_0|$, it vanishes in the above limit. Therefore, to have a finite region of Weyl fermion scattering, the spacing between Weyl nodes

must be kept finite, which we will do in an estimate below.

To give a concrete estimate of the unpolarized cross-section, Eq. (4.7a), we return to the four-band model. An estimate can be achieved by considering exact internode scattering, i.e., $\mathbf{q} = 2\mathbf{k}_0$, for which it has magnitude,

$$\frac{1}{V}\frac{q_i}{q_f}\frac{\mathrm{d}^2\sigma^{(+)}(\mathbf{q},\omega)}{\mathrm{d}\Omega \mathrm{d}E_f} = \left(\frac{gr_0}{4}\right)^2 \frac{\pi}{3}\frac{(\hbar\omega)^2}{(2\pi\hbar v_{\mathrm{F}})^3}(F^x_{\perp,x})^2\,, \tag{6.4a}$$

$$\lesssim 5\cdot 10^{-2}\frac{v_{\mathrm{F}}}{c}\,\frac{\mathrm{mb}}{\mathrm{meV\,\mathring{A}^3\,sr}}\,. \tag{6.4b}$$

The expression Eq. (6.4a) is generally applicable for any inversion invariant Weyl semimetal with a coupling $\mathbf{F}^0 = \mathbf{0}$ and $F^i_j = F^x_{\perp,x}\delta_{i\,j}$ like the four-band model. The estimate[2] Eq. (6.4b) is for the four-band model where the coupling is given by Eq. (5.9). Since the estimate is for exact internode scattering, i.e., $|\tilde{\mathbf{\Delta}}| = 0$, the scattering region is only a single point in neutron momentum transfer $\mathbf{q},\omega$-space. The cross-section Eq. (6.4b) therefore does not allow one to resolve properties of Weyl fermions (to be obtained in the remaining part of this chapter), except for estimating the coupling. For an estimate for $|\tilde{\mathbf{\Delta}}| > 0$ scattering, the estimate Eq. (6.4) would roughly decrease similarly to the density of states of excitations Eq. (6.3). In the estimate, Eq. (6.4b), we made the following substitutions. Since the susceptibility $\chi''^{\mu\nu}_{(+)}$ was derived in the isotropic coordinate system, Eq. (3.5), the factor of v_{F} is not the physical velocity. The physical Weyl nodes have three eigen-velocities; the two perpendicular

[2]Here, b denotes a barn with unit of meter squared, eV denotes an electron volt with unit of joule, sr denotes a steradian which is dimensionless, and Å denotes an Ångström with unit of meter.

to the internode direction are equal to v_{D} whereas the parallel one is smaller, and v_{F} should be the geometric mean of all three, viz., Eq. (5.3). We conservatively took all three velocities to be identical, i.e., $v_{\mathrm{D}} = v_{\mathrm{F}}$. Furthermore, the energy transfer $\hbar\omega$ has been expressed in terms of the displacement of the momenta of the excitations from the Weyl point. We have taken it to be k_0, which is the largest possible as explained in the previous paragraph. Since the result scales as ω^2, the cross-section decreases quickly for momenta below this optimistic value. Finally, $(F^x_{\perp,x})^2$ is taken as $(m_e v_{\mathrm{D}}/k_0)^2$. Despite the fact that $\chi''^{\mu\nu}_{(+)}$ is suppressed by a factor $(\hbar\omega)^2/v_{\mathrm{F}}^3 \propto p^2/v_{\mathrm{F}}$ from the density of states, the coupling squared, $(F^x_{\perp,x})^2$, partly cancels this suppression leaving the product to have an order $\lesssim v_{\mathrm{F}}$ resulting in Eq. (6.4b). This implies that a higher node velocity leads to a higher intensity of the cross-section. For a typical Fermi velocity $v_{\mathrm{F}} = c/300$, Eq. (6.4b) is $\lesssim 1.7 \times 10^{-4}$ mb/meV Å^3 sr. Assuming a typical unit cell has volume $V = (5\text{Å})^3$, the estimate of the cross-section becomes,

$$\frac{q_i}{q_f}\frac{\mathrm{d}^2\sigma^{(+)}(\mathbf{q},\omega)}{\mathrm{d}\Omega \mathrm{d}E_f} \lesssim 2 \times 10^{-2}\ \frac{\mathrm{mb}}{\mathrm{meV\,sr\,f.u.}}\,. \tag{6.5}$$

Had one taken into account the anisotropic velocities of the four-band model, then the estimate Eq. (6.5) still holds for Weyl node positions $k_0 \approx 10^{-1} - 10^{-2}$ Å^{-1} corresponding to half energy band gap $E_{1/2} \approx 100 - 10$ meV. As anticipated for a semimetal, the intensity is low but much higher than the early estimates [66] of the neutron cross-section for normal one-electron metallic band structures, which were of order $10^{-4} - 10^{-3}$mb/meV sr. Our estimate for the four-band model is only of order

$10^{-2} - 1$ smaller than what has been observed in scattering of spin-$\frac{1}{2}$ particle-hole pairs related phenomena [82, 83, 84, 85, 86][3].

In any real experiment, there will always be other background scattering channels besides the Weyl node scattering as illustrated in Fig. 6.2. The relative strength of background channels to Weyl node scattering will vary from compound to compound.

The magnitude of Weyl node scattering is proportional to the squared coupling of neutrons to Weyl fermions. This coupling will likely depend on the given compound, as illustrated with the four-band toy model (see Sec. 5.4). However, the extent of this variation is at present uncertain because of the use of a toy model, only. This toy model served as a proof of principle that the coupling between neutrons and Weyl fermions can be larger than the bare coupling of neutrons to electrons. For a real estimate of a coupling, one needs to know in detail the form of the material's wave functions. In this way, the coupling can be calculated for any type-I Weyl semimetal from Eq. (3.15) for any given band structure.

Likewise, the magnitudes of the background scattering channels will vary from compound to compound depending on the band structure and elemental/isotope composition. For example, at low neutron momentum transfer, a generic magnetic Weyl semimetal could have channels from: (1) multiple scattering involving phonons, (2) incoherent or diffusive scattering from the sample's elements, (3) inelastic magnetic

[3]We thank Youzhe Chen, Jonathan Gaudet, and Collin Broholm for discussing the state of the art in measuring electronic excitations via neutron scattering and providing references.

scattering from local magnetic moments in the sample (c.f. doping by magnetic impurities in the toy model of Sec. 5.4), and (4) magnetic scattering from electronic degrees of freedom such as other bands crossing the chemical potential. On the other hand, a non-magnetic Weyl semimetal could have all of the above but negligible (3). The extent to which each of these channels contribute depends to a large extent on the compound at hand. For example, (4) can be eliminated by choosing an ideal model material where the Weyl nodes are the only bands near the chemical potential as illustrated in Fig. 1.3. Hence, experimentalists should take all these considerations into account when choosing a material for experiments, and preferably estimate the material's coupling to neutrons, Eq. (3.15), before attempting to measure Weyl fermion scattering. Another advantage of calculating the coupling prior to the experiment is that the cross-section for the Weyl fermion scattering channel (see Eq. (4.1) and Eq. (4.7)) can be predicted for any neutron momentum and energy transfers.

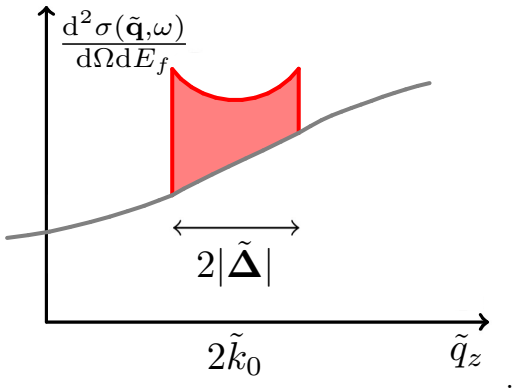

Figure 6.2: Sketch of cross-section including background scattering along $\tilde{q}_z$ in Fig. 2.2 for the M^+ process. The intensity jumps discontinuously at the boundary between the region describing internode scattering (red area) and that which does not (white area), while there might be background scattering (gray curve).

In order to isolate the Weyl fermion scattering component from background, the experimentalist's prior knowledge of the position of the Weyl fermion scattering in energy and momentum space is immediately useful. Figure 2.2 illustrates the fact that the Weyl fermion scattering channel is confined to two very specific regions in momentum space: two ellipsoidal, or spherical, regions centered at $\pm 2\mathbf{k}_0$, which at maximum momentum transfer should appear with an edge above a background intensity if the Weyl fermion scattering channel's intensity is sufficiently large. This discontinuous edge of the Weyl fermion scattering region (see Fig. 6.2 and 6.3) is a strong signature of scattering Weyl fermions, because background scattering channels are expected to be continuous.

In principle, a sharp jump can be separated out from a smooth background by differentiating, but the edge of Weyl fermion scattering region would have to be significantly larger than square root of the background intensity due to counting statistics. This method of differentiation is typically not used in analysis of noisy scattering data because the error bar grows, which may make this method useless. Instead, one can use prior knowledge, from ARPES for example, about the dispersion of Weyl nodes, with which one knows that the region of the Weyl fermion scattering channel (see Eq. (3.7b)) is confined to $\hbar\omega \geq v_{\mathrm{F}}\sqrt{\mathbf{\Delta}^{\mathrm{T}}\lambda^{(2),\mathrm{T}}\lambda^{(2)}\mathbf{\Delta}}$. One can use this knowledge to fit the cross-section data in order to single out the Weyl fermion scattering channel's intensity from background intensity. We know from Sec. 3.1.1.1 and 5.3 that this process determines the principal axis transformation $\mathcal{T}$ from the experiment. As $\mathcal{T}$

has to have determinant $|\mathcal{T}| = 1$, this sets a constraint on the fitting parameters. Once $\mathcal{T}$ is estimated, one has to check that the ellipsoidal regions transform into spheres as illustrated in Fig. 5.2 and 5.3. The intensity region that is singled out by this measured $\mathcal{T}$ will contain the Weyl fermion scattering channel with possibly a background residual, see Fig. 6.2.

To identify the Weyl fermion scattering contribution in this spherical region, one should look for (isotropic) momentum $\tilde{\mathbf{\Delta}}$-dependence, because as Sec. 6.2 explains, angular $\tilde{\mathbf{\Delta}}$-dependence in this region is a sign of scattering Weyl fermions. While the residual background intensity may also show $\tilde{\mathbf{\Delta}}$-dependence, the Weyl fermion cross-section transforms in very particular ways as will be explained in Sec. 6.3. In isotropic coordinates, $\tilde{\mathbf{\Delta}}$, the cross-section with an unpolarized detector consists of terms that transform as a spherical tensor with angular momentum $l = 0$ and 2 if the incident neutron beam is unpolarized, and transform as angular momentum $l = 1$ if the incident neutron beam is polarized. These $\tilde{\mathbf{\Delta}}$-dependencies may be different from that of the background residual. However, if the background scattering is inversion symmetric, then it consists of terms transforming as spherical harmonics of even angular momentum like the cross-section for an unpolarized incident neutron beam. In order to identify whether a background residual is present, one may utilize a feature of the Weyl fermion scattering channel in a fully unpolarized experiment (see Sec. 6.3.1). That is, there is a relation between the cross-section at minimum and maximum momentum transfer for a given energy transfer. One can use this relation to

predict the Weyl fermion scattering channel for any momentum and energy transfers, and to use this as a benchmark to check that the background scattering residual has been removed in the spherical region. However, if it is deemed that a background residual is present in an experiment with an unpolarized incident neutron beam, one may have to proceed to an experiment with a polarized incident neutron beam, see Sec. 6.3.2. Here, the Weyl fermion scattering cross-section consists of a term that transforms as a spherical tensor of angular momentum $l = 1$, which is different from that of an inversion invariant background residual, and these two contributions can therefore be separable.

In addition, to help single out the Weyl fermion scattering channel, it may be possible to use applied fields or energy discrimination, etc. However, the particular techniques that will be needed will vary with compound and also depend on the experimental facility.

In many materials, a term independent of pseudospin, $\mathbf{v}_0^{(i)} \cdot \mathbf{p}$, will be present as explained in Sec. 1.3. Yet, we neglected such a contribution for reasons given in Sec. 3.1.2. To understand what a small $\mathbf{v}_0^{(i)}$ term will do to the cross-section, it is beneficial to recap (see Sec. 3.1.2) what the origin is of the discontinuous jump in the density of states at the surface of the spherical region. It can be understood in two ways. Physically, it is a sum of two-dimensional van Hove singularities [28] along the line of the constant energy contour (which is a degenerate line from 0 to $\tilde{\mathbf{\Delta}}$) illustrated in

Fig. 6.1. Mathematically, it is due to Lorentz-invariance. Hence, the discontinuous jump is unique to the case where $\mathbf{v}_0^{(i)} = \mathbf{0}$ in Eq. (3.1). Consequently, when the vector $\mathbf{v}_0^{(i)}$ is nonvanishing, the dynamics of the excitations are no longer Lorentz invariant.

So, for any type-I Weyl semimetal[4] with $0 < |\mathbf{v}_0|/v_\mathrm{F} < 1$, Lorentz invariance of the cross-section is broken in a more significant way than in the case with $\mathbf{v}_0^{(i)} = \mathbf{0}$, where it was only broken by the coupling parameters $\mathbf{F}^\mu$. As explained in Sec. 1.3, this term only changes the kinematics, with the effect that the constant energy contour for particle-hole pairs are *not* ellipsoids anymore. This has the physical consequence that the cross-section will *not* discontinuously jump to zero at the edge of the scattering region (see Fig. 6.2 and 6.3), but will vanish continuously. If $|\mathbf{v}_0|/v_\mathrm{F}$ is very small, this jump happens in a layer of thickness proportional to $|\mathbf{v}_0|/v_\mathrm{F}$, so when $|\mathbf{v}_0|/v_\mathrm{F} \ll 1$, it seems to be a sharp jump.

On the other hand, when $|\mathbf{v}_0|/v_\mathrm{F}$ is not small, the density of states will vanish smoothly. In this case, spin-momentum locking of Weyl fermions (see Sec. 6.2) could still be observed; it would still cause the cross-section to vary strongly as a function of momentum transfer. However, the susceptibility would not be as simple as Eq. (4.4) and (4.6). To precisely understand how sensitive the predictions (to be obtained in the remaining part of this chapter) are to a non-small $|\mathbf{v}_0|/v_\mathrm{F}$, one has to calculate the corresponding cross-section. Luckily, it is in fact possible to calculate the cross-section

[4]In this case, the terms independent of pseudospin, $\mathbf{v}_0^{(i)} \cdot \mathbf{p}$, of the two nodes are negatives of one another by symmetry (either inversion or time reversal), i.e., $\mathbf{v}_0^{(1)} = -\mathbf{v}_0^{(2)} = \mathbf{v}_0$. This term cannot be removed by a coordinate transformation, contrary to the anisotropic term $\lambda^{(i)}$ which can still be transformed to isotropic form as in Sec. 3.1.1.

for *any* type-I Weyl semimetal, $|\mathbf{v}_0|/v_\mathrm{F} < 1$, as is outlined in our publication Ref. [28].

In order to proceed forming interpretations and making predictions for this theory, the remaining sections 6.2, 6.3, and 6.4 assume that the term independent of pseudospin, $\mathbf{v}_0^{(i)}$, is negligible. Furthermore, it will be assumed that the Weyl fermion scattering in the total measured cross-section has been isolated from background scattering. This means that the cross-sections for the Weyl fermion channel are accurately given by Eq. (4.1) and (4.7) with the suceptibility Eq. (4.4) or (4.6), depending on the symmetry relating Weyl nodes. Lastly, it is assumed that the principal transformation, $\mathcal{T}$, has been determined in the experiment.

6.2 Probing Spin-momentum Locking in a Fully Unpolarized Experiment

While Ch. 4 stated the susceptibility, this chapter will explain[5] it intuitively in terms of familiar concepts of spin matrix elements and spin-momentum locking of Weyl fermions (see Fig. 1.2). This enables us to understand how a fully unpolarized measurement can probe the spin-momentum locking of Weyl spinors, which at first seems like a contradiction. In doing so, we will discover a tool to our advantage: a

[5]Appendix B explains the susceptibility in terms of Lorentz transformations of spinors for the case of scattering between time-reversal symmetric nodes. Ref. [28] offers, in addition, an explanation in terms of the representations of the Lorentz group.

way to control both the momentum and spin of individual particle-hole pairs among the whole continuum contributing to the measured response. This allows us to circumvent one of the major obstacles outlined in Ch. 2.

As mentioned in the introduction of Ch. 6, the cross-section measured in an experiment, Eq. (4.7), depends on the type of symmetry relating the two nodes which we assume to be on the z-axis, $\mathbf{k}_{0,2} = -\mathbf{k}_{0,1} = k_0\hat{\mathbf{z}}$. To cleanly isolate the effects of the susceptibility from the coupling, and to guide our intuition, we will explain it here for the case of the coupling that most closely resembles conventional purely magnetic scattering, i.e., $\mathbf{F}^0 = \mathbf{0}$ and $F^i_j = \delta_{i\,j}$. The unpolarized cross-section, Eq. (4.7a), becomes $\pi\Sigma^{(+)}(\mathbf{q},\omega) = \chi''^{x\,x}_{(+)}(\mathbf{q},\omega) + \chi''^{y\,y}_{(+)}(\mathbf{q},\omega)$, which clearly highlights the fact (see Eq. (3.15)), that neutrons only couple to components of the coupling vectors that are perpendicular to the internode direction[6]. This has the desirable consequence that the cross-section will have angular $\tilde{\mathbf{\Delta}}$-dependence. By the end of this section, it will become clear that observing any angular $\tilde{\mathbf{\Delta}}$-dependence of the cross-section is a signature of probing spin-momentum locking of Weyl spinors. Recall, that the cross-section is proportional to the integrand of the density of states, Eq. (3.21), multiplied by the squared matrix element of the interaction between initial and final states, $|\langle f_{\mathrm{w}}, f_{\mathrm{n}}|H_{int}|i_{\mathrm{n}}, i_{\mathrm{w}}\rangle|^2$, which is summed over all initial and final neutron spin states, $|f_{\mathrm{n}}\rangle$ and $|i_{\mathrm{n}}\rangle$, and internal Weyl fermion degrees of freedom $|f_{\mathrm{w}}\rangle$ and $|i_{\mathrm{w}}\rangle$.

[6]This is analogous to any other neutron scattering experiment, where only components of the interaction perpendicular to neutron momentum transfer enters the cross-section.

The neutron states do not depend strongly on momentum. On the other hand, the Weyl states depend strongly on momentum because their components are the solutions to the Weyl equation (called $\mathbf{c}(\mathbf{p})$ in Sec. 3.2.1), which inherit the singularity at the nodes. This is the origin of the momentum dependence of the cross-section, which together with spin-momentum locking of Weyl fermions (see Fig. 1.2), leads to the property that neutrons become polarized upon scattering off Weyl nodes. This means, that neutrons become polarized although the Weyl semimetal may not have a permanent magnetic order.

First, let us investigate the consequence of energy-momentum conservation (c.f. Sec. 6.1) in a scattering event. A consequence of momentum conservation is that the initial $|i_{\mathrm{w}}\rangle = |\widehat{\tilde{\mathbf{p}}}_i; -\chi_i\rangle$ and final $|f_{\mathrm{w}}\rangle = |\widehat{\tilde{\mathbf{p}}}_f; +\chi_f\rangle$ Weyl states are related by $\tilde{\mathbf{p}}_f = \tilde{\mathbf{p}}_i - \tilde{\mathbf{\Delta}}$, and energy conservation dictates that any pair $\tilde{\mathbf{p}}_i$ and $\tilde{\mathbf{p}}_f$ are restricted to the ellipsoid constant energy contour in Fig. 6.1. In the limit of exact internode scattering, i.e., $\tilde{\mathbf{\Delta}} = \tilde{\mathbf{p}}_i - \tilde{\mathbf{p}}_f = \mathbf{0}$, the allowed initial and final states are pairs $\tilde{\mathbf{p}}_f = \tilde{\mathbf{p}}_i$ on a sphere of radius $\hbar\omega/2v_{\mathrm{F}}$, and the polarization of the Weyl spinors are thus related by,

$$\langle f_{\mathrm{w}}|\boldsymbol{\sigma}|f_{\mathrm{w}}\rangle = \mp\langle i_{\mathrm{w}}|\boldsymbol{\sigma}|i_{\mathrm{w}}\rangle \quad \text{for} \quad \chi_f = \pm\chi_i\,. \tag{6.6}$$

In other words, the initial and final spinors are antiparallel for same chirality, whereas

they are parallel for opposite chirality[7]. All these different spinors only contribute to the cross-section at a single point, so there is no signature that distinguishes between $\chi_f = \pm\chi_i$ apart from a constant factor of 2 (which cannot be measured unless one knows the values of the coupling parameters).

For increasing $|\tilde{\mathbf{\Delta}}|$, the energy conserving contour takes a more extreme prolate spheroid form, and the cross-section will have angular $\tilde{\mathbf{\Delta}}$-dependence because the Weyl state contributions depend on the direction of $\tilde{\mathbf{\Delta}}$.

In the extreme limit of possible momentum transfer for a given energy transfer, $|\tilde{\mathbf{\Delta}}| \approx \hbar\omega/v_{\mathrm{F}}$, the energy conserving contour becomes an extremely slim, elongated prolate spheroid, which degenerates to a line at maximum $|\tilde{\mathbf{\Delta}}| = \hbar\omega/v_{\mathrm{F}}$. The initial and final unit vectors along the momenta are therefore approximately $\hat{\tilde{\mathbf{p}}}_i \approx \hat{\tilde{\mathbf{\Delta}}} \approx -\hat{\tilde{\mathbf{p}}}_f$, so states are $|i_{\mathrm{w}}\rangle \approx |\hat{\tilde{\mathbf{\Delta}}}; -\chi_i\rangle$ and $|f_{\mathrm{w}}\rangle \approx |\hat{\tilde{\mathbf{\Delta}}}; -\chi_f\rangle$. This means that spinors are related as,

$$\langle f_{\mathrm{w}}|\boldsymbol{\sigma}|f_{\mathrm{w}}\rangle = \pm\langle i_{\mathrm{w}}|\boldsymbol{\sigma}|i_{\mathrm{w}}\rangle \quad \text{for} \quad \chi_f = \pm\chi_i, \tag{6.7}$$

which is the reverse of Eq. (6.6). Because of this, the momenta of the particle and hole are opposite to each other, while the spins Eq. (6.7) are parallel or antiparallel to one another depending on the type of symmetry.

This means that at maximal momentum transfer, $|\tilde{\mathbf{\Delta}}| = \hbar\omega/v_{\mathrm{F}}$, both excitations

[7]To understand this, remember that the initial state has a negative energy and the final state has a positive energy.

in a particle-hole pair must move parallel to the transferred momentum and thus, their spin states are uniquely determined. Hence, as far as pseudospin degree is concerned, there is just a single spin state of excitation produced rather than a continuum. This simple observation will be to our advantage: it can be used to resolve definite spin and momentum properties of Weyl excitations despite the measured neutron response receiving contributions from a particle-hole continuum. In other words, at maximal momentum transfer, the spin-momentum locking of particle-hole pairs is fully observable as will be clear in the next paragraph. This knowledge will be used in Sec. 6.3 and 6.4.

Let us apply the above insight to understand how anisotropic angular dependence of the cross-section occurs despite all neutron spin states being summed in the experiment. For the coupling in consideration the interaction of electrons and neutrons is proportional to $H_{int} = \sigma_x\tau_x + \sigma_y\tau_y$, where $\boldsymbol{\sigma}$ and $\boldsymbol{\tau}$ are Pauli spin matrices of the electron and neutron, respectively. It clearly shows that only components of the neutron and the Weyl fermion spin Pauli matrices which are transverse to the internode direction enter the interaction. The cross-section is proportional to the integral of the matrix element squared, $|\langle\tau_f, \chi_f; \widehat{\widetilde{\mathbf{p}}}_f|\sigma_x\tau_x + \sigma_y\tau_y|\widehat{\widetilde{\mathbf{p}}}_i; -\chi_i, \tau_i\rangle|^2$, over all possible final states of the electron. Even in the case of unpolarized neutrons, which averages this over all initial and final neutron spin states, the result $|\langle\chi_f; \widehat{\widetilde{\mathbf{p}}}_f|\sigma_x|\widehat{\widetilde{\mathbf{p}}}_i; -\chi_i\rangle|^2 + |\langle\chi_f; \widehat{\widetilde{\mathbf{p}}}_f|\sigma_y|\widehat{\widetilde{\mathbf{p}}}_i; -\chi_i\rangle|^2$ is still asymmetric. The effect of this

interaction, in which σ_x or σ_y are applied to the Weyl fermion's pseudospin, is different depending on the initial direction of the momenta of the Weyl fermions: for some directions it is more likely to flip it, and for others it is more likely not to. This causes the cross-section to oscillate over the surface of the sphere of constant momentum transfer. This oscillation has a different form for the time-reversal and inversion-symmetric cases. For example, at maximum momentum transfer for the time-reversal symmetric case, the spin directions before and after scattering must be parallel according to Eq. (6.7), so the cross-section is zero when $\tilde{\mathbf{\Delta}} \to \pm\hbar\omega/v_{\mathrm{F}}\hat{\mathbf{z}}$ (in which case, both σ_x and σ_y flip the spin). Likewise, the cross-section is maximum on this axis in the inversion-symmetric case because the Weyl fermions must flip spin. This behavior for both the time-reversal symmetric and inversion-symmetric case is an explicit example of the observation from the previous paragraph: at maximum momentum transfer, the spin and momentum of the excitations are fully locked. These features are illustrated in Fig. 6.3, which plots the variation of the cross-section as a function of $|\tilde{\mathbf{\Delta}}|$ on the $\tilde{\Delta}_z$-axis for the two types of symmetry. The analog features in the $\tilde{\Delta}_x\tilde{\Delta}_y$-plane, are also illustrated. Furthermore, from Fig. 6.3 one can also see the discontinuous jump of the cross-section at the $|\tilde{\mathbf{\Delta}}| = \hbar\omega/v_{\mathrm{F}}$ surface of the spherical region containing scattering from Weyl fermions.

In general for any given coupling, due to energy and momentum constraints of the excitations, the scattering channels are effectively those of a polarized measurement for any $|\tilde{\mathbf{\Delta}}| > 0$ with the degree of polarization being maximal for maximal

momentum transfer $|\tilde{\mathbf{\Delta}}| = \hbar\omega/v_{\mathrm{F}}$. Hence by sweeping $\tilde{\mathbf{\Delta}}$, i.e., by sweeping external neutron momentum transfer $\mathbf{q}$, one indirectly performs a polarized experiment despite not using polarized neutrons. This is exactly what Fig. 6.3 illustrates for the specific coupling considered here, viz., $\mathbf{F}^0 = \mathbf{0}$ and $F^i_j = \delta_{i\,j}$. For the same coupling, Fig. 6.4(a),(b) and (c) plot the full $\tilde{\mathbf{\Delta}}$-dependence of the cross-section for the case of inversion symmetric nodes. Furthermore, for a given energy and momentum transfer the cross-section intensity oscillates over the surface of the sphere of constant momentum transfer $|\tilde{\mathbf{\Delta}}|$. This variation depends on the specific coupling, Eq. (3.15), of the Weyl semimetal, which is illustrated in Fig. 6.4 for three different couplings. For the reasons explained above, any angular $\tilde{\mathbf{\Delta}}$-dependence of the cross-section is a consequence of probing a correlation between spin and momentum of the Weyl particle-hole pairs, which at maximal momentum transfer is fully spin-momentum locked.

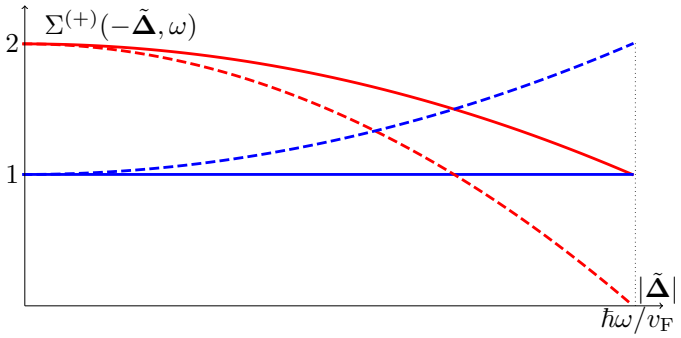

Figure 6.3: Cuts of the unpolarized cross-section for a coupling $\mathbf{F}^0 = \mathbf{0}$ and $F^i_j = \delta_{i\,j}$. The cross-section is plotted as a function of $|\tilde{\mathbf{\Delta}}|$ for scattering between nodes related by time-reversal ($\chi_f = +\chi_i$) in red lines, and nodes related by inversion symmetry ($\chi_f = -\chi_i$) in blue lines. Full lines are for momentum transfer in the $\tilde{\Delta}_x\tilde{\Delta}_y$-plane, and dashed lines are for momentum transfer along the $\tilde{\Delta}_z$-axis.

To recap, the angular $\tilde{\mathbf{\Delta}}$-dependence of the cross-section of unpolarized neutrons results from a combination of two facts: first, the electron polarization is dependent on the transferred momentum, and second, the coupling $F^i_{\perp,j}$ is anisotropic (not only for the specific coupling discussed above, but in general), so it is possible to see the variation of the electron-polarization even with unpolarized neutrons. If, hypothetically, it had been the case that $F^i_{\perp,j} = \delta_{i\,j}$, then the cross-section would have no angular $\tilde{\mathbf{\Delta}}$-dependence, but would be spherically symmetric as a function of $|\tilde{\mathbf{\Delta}}|$ for a given ω. However, $F^i_{\perp,j}$ can *never* be diagonal because in a coordinate system where $\hat{\mathbf{k}}_0 = \hat{\mathbf{z}}$, $F^i_{\perp,j}$ would have two columns orthogonal to $\hat{\mathbf{k}}_0$ because $\mathbf{F}^i_\perp \cdot \hat{\mathbf{k}}_0 = 0$ holds *always*. This generally implies angular $\tilde{\mathbf{\Delta}}$-dependence. However, although this condition rules out $F^i_{\perp,j} = \delta_{i\,j}$, there *is* a way that the spin-momentum locking could be hidden in the time-reversal symmetric case. The coupling,

$$F^i_{\perp,j} = \begin{pmatrix} 1 & 0 & 0 \\ 0 & 1 & 0 \\ i & 0 & 0 \end{pmatrix}_{i\,j} , \tag{6.8}$$

gives a cross-section $\pi\Sigma^{(+)}(\mathbf{q},\omega) = \chi''^{x\,x}_{(+)}(\mathbf{q},\omega) + \chi''^{y\,y}_{(+)}(\mathbf{q},\omega) + \chi''^{z\,z}_{(+)}(\mathbf{q},\omega)$, which has the same effect as if $F^i_{\perp,j} = \delta_{i\,j}$. Such a coupling is allowed, though probably not very likely to occur since it is very specific. Consequently, any angular $\tilde{\mathbf{\Delta}}$-dependence of the Weyl fermion scattering cross-section *implies* probing spin-momentum locking.

The reverse statement *is* necessarily true for inversion-symmetric nodes, whereas it is *not* necessarily true for time-reversal symmetric nodes. Notice, for both time-reversal and inversion symmetric nodes, it may happen that the coupling is such that no angular $\tilde{\mathbf{\Delta}}$-dependence of the cross-section occurs for a specific energy transfer $\hbar\omega = \hbar\omega_0$. However, unless the coupling happens to be exactly Eq. (6.8) for time-reversal symmetric nodes, angular $\tilde{\mathbf{\Delta}}$-dependence is guaranteed to be observed for any $\hbar\omega \neq \hbar\omega_0$ within the allowed energy window.

Notice that the above statements were for the cross-section containing the Weyl fermion scattering channel only. If background scattering contributions have not been entirely removed from the spherical region $\hbar\omega \geq |\tilde{\mathbf{\Delta}}|$, it may be that background scattering contributions also show $\tilde{\mathbf{\Delta}}$-dependence. As discussed in the previous chapter, 6.1, one should therefore identify and remove any residual background contributions in this spherical region, before one can conclude that observed angular $\tilde{\mathbf{\Delta}}$-dependence of the total cross-section is evidence of probing spin-momentum locking. To check that the angular $\tilde{\mathbf{\Delta}}$-dependence of the cross-section is indeed due to Weyl fermion scattering, one should check that the angular $\tilde{\mathbf{\Delta}}$-dependence has the characteristics of the Weyl fermion cross-section as will be explained in next section, 6.3.

As a fully unpolarized experiment is the easiest inelastic neutron scattering experiment, the above simple fact may serve as a useful way of observing Weyl nodes. Its utility is due to the fact that observing angular $\tilde{\mathbf{\Delta}}$-dependence does not require a

full resolution of the nodes' dispersions. That is so, because the probing mechanism is measuring correlations of Weyl fermions' pseudospinors, which are guaranteed to exist if Weyl nodes are present and near the chemical potential. The strong angular $\tilde{\mathbf{\Delta}}$-dependence of the cross-section reflects that the spherical harmonics, Eq. (4.4) and (4.6), change rapidly as a function of $\tilde{\mathbf{\Delta}}$. For any energy transfer $\hbar\omega$, the cross-section varies strongly on the surface of the sphere $|\tilde{\mathbf{\Delta}}| = \hbar\omega/v_{\mathrm{F}}$. This is a large variation for a small change in momentum. That is because the Weyl particle and hole have their momentum locked to spin, or equivalently, reflecting the singularity of the wavefunctions $|\tilde{\mathbf{p}};\eta\chi\rangle$ at $\tilde{\mathbf{p}} = 0$. This differs from scattering between two pockets of a narrow gap semiconductor (see illustration Fig. 1.3), where there would be no angular $\tilde{\mathbf{\Delta}}$-dependence because the wavefunctions are continuous.

As was briefly mentioned in Sec .1.3.1, one of the simplest ways (at least theoretically) to construct a Weyl semimental is to begin with a narrow gap semiconductor (described as the massive Dirac Eq. (1.1)). Breaking time-reversal or inversion symmetry will generate a Weyl semimetal of either kind. However, if the perturbation is insufficient, the massive Dirac fermions will not split into massless Weyl fermions, and a narrow gap remains, meaning that the material is still an ordinary semiconductor. An inherent surface probe such as ARPES will have difficulty distinguishing such a state from a Weyl semimental by a bulk dispersion measurement because of finite resolution effects, and the fact that only holes are probed. On the other hand, an inelastic neutron scattering experiment is not prone to such a misidentification

because the observation of angular $\tilde{\mathbf{\Delta}}$-dependence reflects the Weyl semimental bulk topology.

6.3 Experiment with Unpolarized Detector: Inversion Symmetric Nodes

The cross-section for scattering on any given Weyl semimetal depends on the material's couplings. As illustrated in Fig. 6.4, the unpolarized cross-section intensity pattern changes significantly for just a small change in the couplings. In general, the coupling for inversion-symmetric nodes, Eq. (6.2), can have 8 independent parameters, which are *a priori* unknown. This suggests that there might not be any particular patterns hidden in the cross-section measured for an arbitrary Weyl semimetal. Furthermore, it might not be possible to observe the chiralities of the two Weyl nodes involved in the scattering. Another issue is that while the cross-section has angular $\tilde{\mathbf{\Delta}}$-dependence as illustrated in Figs. 6.3 and 6.4, these variations are smooth. This reflects the fact that the susceptibilities Eq. (4.4) and (4.6) are polynomials of the transferred momentum to maximum second degree. This means that the cross-section has no strong features, like a peak in its intensity. For this reason, we need to identify features of the cross-section that reflect Weyl fermion scattering besides the strong signature of a discontinuous cross-section edge.

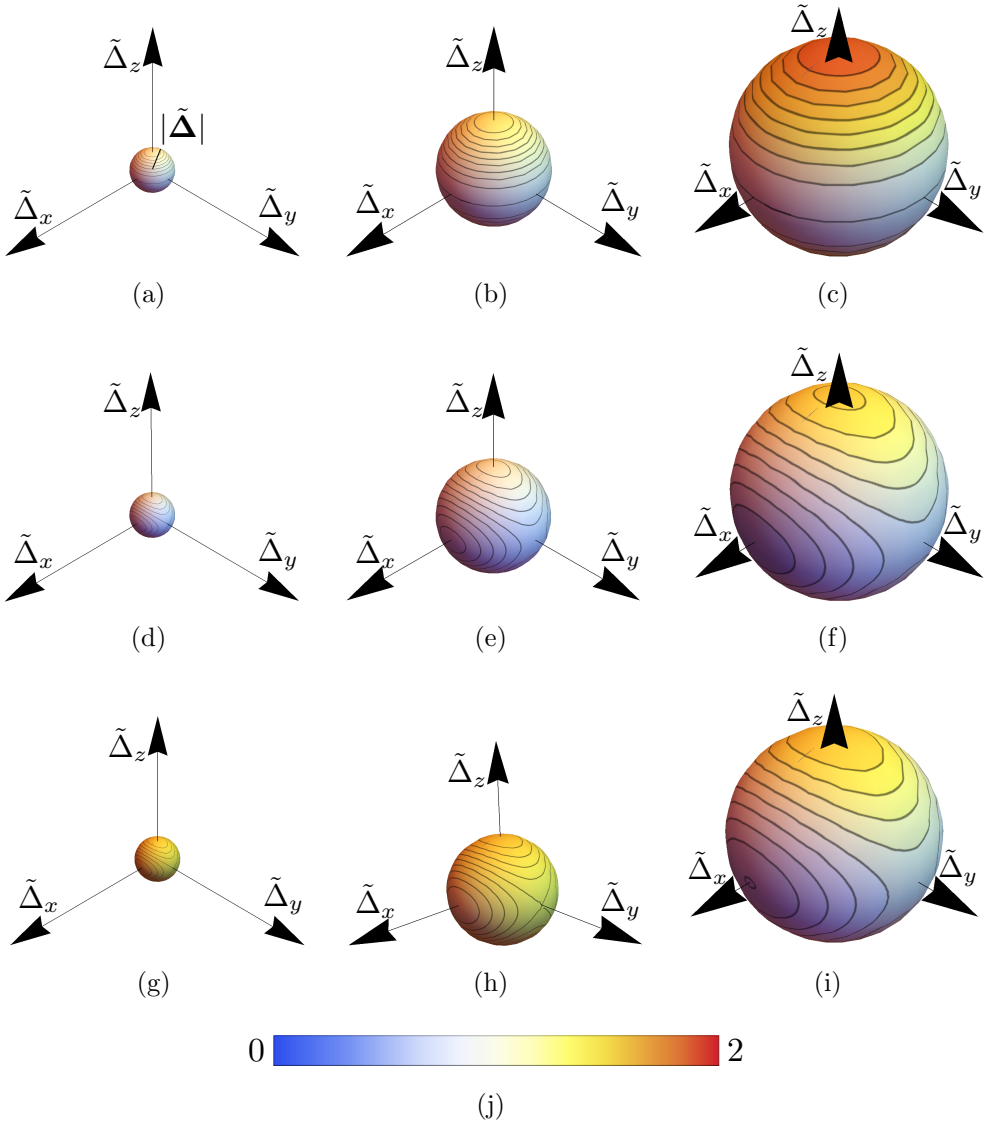

Figure 6.4: Comparison of unpolarized cross-sections for different couplings. The cross-section $\Sigma^{(+)}(-\tilde{\mathbf{\Delta}}, \omega)$ for scattering between inversion symmetric nodes is plotted in isotropic coordinates $\tilde{\mathbf{\Delta}}$ for a given energy transfer $\hbar\omega$. Columns are cuts of $|\tilde{\mathbf{\Delta}}|$ with the left, middle, and right columns at $|\tilde{\mathbf{\Delta}}|v_F/\hbar\omega = 0.2, 0.5$, and 0.95, respectively. All rows are the same case of coupling eigendirections, Eq. (4.8a), $\hat{\mathbf{a}}_1 = \hat{\mathbf{x}}$ and $\hat{\mathbf{a}}_2 = \hat{\mathbf{y}}$ but different eigenvalues α_1 and α_2 and constant $|\mathbf{F}^0_\perp|$. The upper row [(a),(b),(c)] is for $|\mathbf{F}^0_\perp| = 0$ and $\alpha_1 = \alpha_2 = 1$, The middle row [(d),(e),(f)] is for $|\mathbf{F}^0_\perp| = 0$ and $\alpha_1 = 2\alpha_2 = 1$. The lower row [(g),(h),(i)] is for $|\mathbf{F}^0_\perp| = 1/2$ and $\alpha_1 = 2\alpha_2 = 1$. Intensity is given by the temperature scale in subfigure (j).

In this section, we will only consider scattering on inversion symmetric nodes[8]. It will be shown that the $\tilde{\mathbf{\Delta}}$-dependence of the Weyl fermion cross-section transforms in very particular ways, despite the many unknown coupling parameters: the cross-section with an unpolarized detector consists of terms that transform as a spherical tensor with angular momentum $l = 0$ and 2 if the incident neutron beam is unpolarized, and will transform as angular momentum $l = 1$ if the incident neutron beam is polarized. In addition, in an experiment with unpolarized incident neutrons and an unpolarized detector, the discontinuous cross-section edge has a pattern which reflects scattering on Weyl fermions. For the case where the incident neutrons are polarized, it will be shown that the chirality can *only* be extracted from the cross-section if the coupling is known. Section 6.4 explains how one can measure the chirality when the coupling is unknown.

6.3.1 Unpolarized Incident Neutrons

For inversion symmetric nodes, the inelastic cross-section, Eq. (4.7), is determined by the susceptibility, Eq. (4.6), and the coupling, Eq. (6.2), which is restricted to be real. For unpolarized incident neutrons the cross-section, Eq. (4.7a), is,

$$\pi\Sigma^{(+)}(\mathbf{q},\omega) = \alpha_0 \frac{3a}{2}[(\hbar\omega/v_{\mathrm{F}})^2 - |\tilde{\mathbf{\Delta}}|^2] + \frac{a}{2}\sum_{m=1}^{2} \alpha_m \left[(\hbar\omega/v_{\mathrm{F}})^2 + |\tilde{\mathbf{\Delta}}|^2 - 2|\tilde{\mathbf{\Delta}} \cdot \hat{\mathbf{a}}_m|^2\right], \tag{6.9}$$

[8]Ref. [28] considers, in addition, the cross-section for time-reversal symmetric nodes.

where $\hat{\mathbf{a}}_1, \hat{\mathbf{a}}_2$ are the two orthogonal, real eigendirections from the spectral decomposition, Eq. (4.8a), of the effective coupling, and α_1, α_2 are the corresponding eigenvalues. The term $\alpha_0 = \mathbf{F}^0_\perp \cdot \mathbf{F}^0_\perp$ is generically nonzero and allows a scalar $\chi''^{0\,0}_{(+)}$ contribution to the cross-section with no angular $\tilde{\mathbf{\Delta}}$-dependence. As $\chi''^{i\,0}_{(+)} = 0$ and $\mathbf{F}^i_\perp \cdot \mathbf{F}^j_\perp$ is symmetric in spin-indices, only the symmetric part of $\chi''^{i\,j}_{(+)}$ $(i, j = 1, 2, 3)$ contributes. The cross-section therefore consists of terms that transform as spherical tensors with angular momentum $l = 0$ and 2. Because the chirality of the node, where a hole is created, can *only* enter the cross-section through the antisymmetric part of the susceptibility $\chi''^{i\,j}_{(+)}$, it is therefore not possible to measure the chirality of the nodes with unpolarized incident neutrons.

The coupling is unknown without a specific Weyl semimetal band structure, so plotting the cross-section, Eq. (6.9), for many different couplings does not inform us much. However, it is still useful to plot the cross-section for a few possible couplings to illustrate the usefulness of expressing it in isotropic coordinates and using the spectral decomposition of the effective coupling. The cross-section, Eq. (6.9), is plotted in Fig. 6.4 as a function of $\tilde{\mathbf{\Delta}}$ for the case where effective coupling eigendirections of Eq. (4.8a) are $\hat{\mathbf{a}}_1 = \hat{\mathbf{x}}$ and $\hat{\mathbf{a}}_2 = \hat{\mathbf{y}}$ for various eigenvalues values α_1, α_2 and constant α_0. The four-band toy model (see Ch. 5.4) corresponds to an effective coupling with $\hat{\mathbf{a}}_1 = \hat{\mathbf{x}}$, $\hat{\mathbf{a}}_2 = \hat{\mathbf{y}}$, $\alpha_1 = \alpha_2 = (F^x_{\perp,x})^2$ and $\alpha_0 = 0$, the cross-section of which therefore has the same angular dependence as the top row of Fig. 6.4, but the intensity is a factor $2(F^x_{\perp,x})^2$ amplified by the value in Fig. 5.4.

From the plots of the cross-section in Fig. 6.4 for a few specific F's it seems as if there is no pattern that is common for them all. Furthermore, the cross-section intensity distribution for any other coupling (than those in the plots) would be distorted in a different way. But this is not entirely true – the cross-section, Eq. (6.9), *has* a particular pattern[9] on the edge of the scattering region (see Fig. 6.2). To see this, we utilize the fact that the internode direction, $\hat{\mathbf{a}}_3 = \hat{\mathbf{k}}_0$, in pseudospin space is not coupled to the neutron spin. The unit vector $\hat{\mathbf{a}}_3$ completes a basis with the eigendirections, $\hat{\mathbf{a}}_1, \hat{\mathbf{a}}_2$, of the effective coupling. Hence, we can expand the momentum squared in terms of this basis, $|\tilde{\mathbf{\Delta}}|^2 = \sum_{m=1}^{3} (\tilde{\mathbf{\Delta}} \cdot \hat{\mathbf{a}}_m)^2$, to express Eq. (6.9) as,

$$\pi \Sigma^{(+)}(\mathbf{q}, \omega) = \bar{\alpha} a \left[(\hbar\omega / v_F)^2 + \sum_{m=1}^{3} c_m (\tilde{\mathbf{\Delta}} \cdot \hat{\mathbf{a}}_m)^2 \right], \tag{6.10}$$

with constants $\bar{\alpha} = 3\alpha_0/2 + \alpha_1 + \alpha_2$ and $\bar{\alpha} c_m = \alpha_1 + \alpha_2 - 2\alpha_m - 3\alpha_0/2$. Here, $\alpha_3 = 0$ while $\alpha_0, \alpha_1, \alpha_2 \geq 0$ are determined by the material's coupling. In the coordinate system of the experiment, this could be an arbitrary quadratic function of $\tilde{\mathbf{\Delta}}$, but with respect to the $\hat{\mathbf{a}}_1, \hat{\mathbf{a}}_2, \hat{\mathbf{a}}_3$-basis, the $\tilde{\mathbf{\Delta}}$-dependence of this quadratic function is diagonal. At maximum momentum transfer for given energy transfer, the cross-section, Eq. (6.10), is a quadratic form on the surface of a sphere of radius $|\tilde{\mathbf{\Delta}}| = \hbar\omega / v_{\mathrm{F}}$, which has extrema at diametrically opposite pairs of points corresponding to the eigendirections

[9] On a side note, it has not been checked whether the cross-sections, neither unpolarized nor polarized incident or scattered neutrons for time-reversal symmetric nodes, have a similar structure. The method used to derive Eq. (6.10) is still valid for complex basis vectors.

of the effective coupling and the internode direction. Hence, for momentum along these directions the cross-section always takes the values,

$$\pi\Sigma^{(+)}(\mathbf{q},\omega) = \begin{cases} 2a\alpha_2(\hbar\omega/v_{\mathrm{F}})^2 & \text{at } \hat{\tilde{\mathbf{\Delta}}} = \pm\hat{\mathbf{a}}_1 \quad (6.11a) \\ 2a\alpha_1(\hbar\omega/v_{\mathrm{F}})^2 & \text{at } \hat{\tilde{\mathbf{\Delta}}} = \pm\hat{\mathbf{a}}_2 \quad (6.11b) \\ 2a(\alpha_1+\alpha_2)(\hbar\omega/v_{\mathrm{F}})^2 & \text{at } \hat{\tilde{\mathbf{\Delta}}} = \pm\hat{\mathbf{a}}_3 = \pm\hat{\mathbf{k}}_0 \quad (6.11c) \end{cases}$$

The last is the largest since $\alpha_1, \alpha_2 \geq 0$. Figure 6.5 illustrates the signature, Eq. (6.11), of the Weyl fermion scattering cross-section edge illustrated in Fig. 6.2. Although the cross-sections in Fig. 6.4 are not plotted exactly at maximum momentum transfer, one can still see the development of the predicted pattern Eq. (6.11) in Figs. 6.4(i), (f) and (c) along $\hat{\mathbf{a}}_1 = \hat{\mathbf{x}}$, $\hat{\mathbf{a}}_2 = \hat{\mathbf{y}}$ and $\hat{\mathbf{a}}_3 = \hat{\mathbf{z}}$.

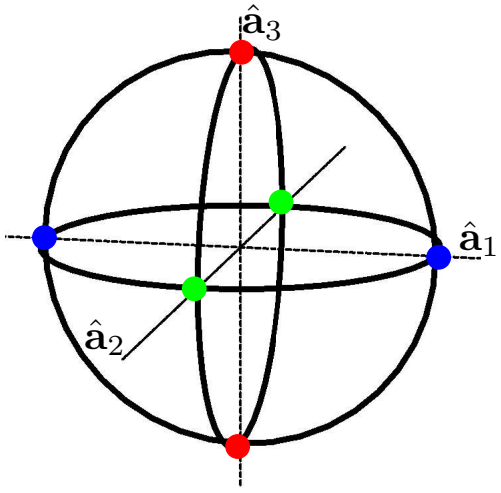

Figure 6.5: Signature of the cross-section edge. Extrema at diametrically opposite pairs of points on the surface of maximum momentum transfer $|\tilde{\mathbf{\Delta}}| = \hbar\omega/v_F$ for a given energy transfer. Cross-section maxima at $\hat{\tilde{\mathbf{\Delta}}} = \pm\hat{\mathbf{a}}_3 = \pm\hat{\mathbf{k}}_0$. Saddel-points and minima at $\hat{\tilde{\mathbf{\Delta}}} = \pm\hat{\mathbf{a}}_2$ and $\hat{\tilde{\mathbf{\Delta}}} = \pm\hat{\mathbf{a}}_1$, or vice versa.

The signature, Eq. (6.11), of the Weyl fermion scattering edge is not universal in the sense of being independent of the material's coupling, nor is it unique to scat-

tering Weyl fermions. First, both the locations and magnitudes of the cross-section's minima and saddle-points depend on the coupling. Second, for a system that is invariant under inversion, the background scattering could also be inversion symmetric. If so, the background scattering should consist of spherical tensors transforming as even angular momentum like the fully unpolarized cross-section for scattering Weyl fermions. Therefore, the background scattering could also exhibit extrema at diametrically opposite points on a $|\mathbf{\Delta}|$-surface for some momentum [87]. However, it is not *a priori* guaranteed that these extrema should occur only at maximum momentum transfer for a given energy, nor that the maxima should be along the internode direction. The discontinuous Weyl fermion scattering cross-section edge is quantitatively universal in the sense that for any coupling, the edge of the associated cross-section at maximum momentum transfer for given energy transfer will always have extrema given by Eq. (6.11) with maxima along the internode direction $\hat{\mathbf{a}}_3 = \hat{\mathbf{k}}_0$.

Another property that may help to identify whether a background scattering residual with the above property is present, is that the Weyl fermion scattering cross-section, Eq. (6.10), at minimum momentum transfer for a given energy transfer takes the value,

$$\pi\Sigma^{(+)}(2\mathbf{k}_0, \omega) = a(3\alpha_0/2 + \alpha_1 + \alpha_2)(\hbar\omega/v_{\mathrm{F}})^2 \quad \text{at} \quad |\tilde{\mathbf{\Delta}}| = 0\,, \tag{6.12}$$

which is larger or equal to half the maxima, Eq. (6.11c), for maximum momentum transfer depending on α_0 being present or not. By measuring the cross-section at minimum momentum transfer, Eq. (6.12), and maximum momentum transfer, Eq. (6.11), for a given energy transfer, one can measure the basis $\hat{\mathbf{a}}_1, \hat{\mathbf{a}}_2$, and $\hat{\mathbf{a}}_3 = \hat{\mathbf{k}}_0$, and parameters α_0, α_1, and α_2. Knowing these means that one knows the effective couplings[10], Eq. (4.8a) and Eq. (4.8b). This information allows one to reconstruct not only the fully unpolarized cross-section (see Eq. (6.10)) but also the partially polarized cross-section (see Sec. 6.3.2) and the fully the polarized cross-section (see Sec. 6.4) of the Weyl fermion scattering for any neutron momentum transfer, $\mathbf{q}$, and energy transfer, $\hbar\omega$. If the measured fully unpolarized cross-section matches the predicted unpolarized cross-section of the Weyl fermion scattering, it is likely that the background scattering residual has been removed. On the other hand, if the predicted Weyl fermion scattering cross-section does not match the measured cross-section, then the background scattering residual has not been removed. In this case, in order to remove the background residual, one may have to proceed to perform an experiment with an unpolarized detector but incident polarized neutron beam, discussed in the next subchapter.

[10]The spectral decomposition, $\mathbf{F}^i_\perp \cdot \mathbf{F}^j_\perp = \sum_{m=1}^2 \alpha_m \hat{\mathbf{a}}^i_m \hat{\mathbf{a}}^j_m$, implies $F^i_{\perp,j} = \sum_{m=1}^2 \sqrt{\alpha_m} \hat{\mathbf{a}}^i_m \hat{\mathbf{a}}'^j_m$ for a certain pair of orthonormal vectors $\hat{\mathbf{a}}'_1, \hat{\mathbf{a}}'_2$, according to the theory of singular value decompositions. Thus, the interaction is $F^i_{\perp,j}\tau_j\sigma_i = \sum_{m=1}^2 \sqrt{\alpha_m}(\hat{\mathbf{a}}_m \cdot \boldsymbol{\sigma})(\hat{\mathbf{a}}'_m \cdot \boldsymbol{\tau})$.

6.3.2 Polarized Incident Neutrons

For polarized incident neutrons, the cross-section, Eq. (4.7b), is,

$$\pi \mathbf{P} \cdot \mathbf{\Sigma}^{(+)}(\mathbf{q}, \omega) = -\chi a \left(\hbar\omega / v_{\mathrm{F}}\right) \mathbf{P} \cdot (\mathbf{F}^i_\perp \times \mathbf{F}^j_\perp) \epsilon_{ijk} \tilde{\Delta}_k. \tag{6.13}$$

Despite the possibility that $\mathbf{F}^0_\perp \neq \mathbf{0}$, there is no $\chi''^{0\,0}_{(+)}$ contribution because $\widehat{\mathbf{k}}_0 \cdot \mathbf{F}^0_\perp \times \mathbf{F}^0_\perp = 0$. As $\chi''^{i\,0}_{(+)} = 0$ and $\mathbf{F}^i_\perp \times \mathbf{F}^j_\perp$ is antisymmetric in spin-indices, only the antisymmetric part of $\chi''^{i\,j}_{(+)}$ contributes[11], which is a term that transforms as a spherical tensor with angular momentum $l = 1$. This $\tilde{\mathbf{\Delta}}$-dependence is different from that of an inversion invariant background residual as explained in the previous section, and may therefore be used to separate the Weyl fermion and background scattering channels.

The cross-section, Eq. (6.13), depends on the chirality where a hole is created. If and only if the coupling is known, it is possible to measure the chirality from Eq. (6.13), i.e., in an experiment with polarized incident neutrons and an unpolarized detector. On the other hand, if the coupling is unknown, then it is not possible to measure the chirality even with polarized neutrons when the detector is unpolarized. The next section explains that the polarization-independent and dependent cross-sections $\Sigma^{(+)}, \mathbf{\Sigma}^{(+)}$ are not enough to determine χ in this case, because there is always at least one choice of $\mathbf{F}^\mu$ that matches the data for each of $\chi = \pm 1$.

[11] From the antisymmetric part of $\chi''^{i\,j}_{(+)}$ one sees that this measures "chiral" fluctuations $\langle \boldsymbol{\sigma}(\mathbf{q}, \omega) \times \boldsymbol{\sigma}(-\mathbf{q}, -\omega) \rangle \cdot \tilde{\mathbf{\Delta}}$ originating in the axial-vector of the interaction.

6.4 Experiment with Polarized Detector and Polarized Incident Neutrons

Let us consider a polarized neutron incident on the Weyl semimetal and a detector filtering the polarization of the scattered neutron. The scattering event was hitherto described as the neutron acting on the Weyl semimetal by its neutron magnetic field (induced by its magnetic moment), creating a particle-hole pair which makes transitions within a continuum of states. Despite being in control (in principle) of both incident and scattered/final neutron spins, what one actually measures is the momentum of the excitations through the neutron's transferred momentum. From this, we ultimately want to infer the chirality of the excitations. This is a daunting task, because the response receives contributions from the whole particle-hole continuum, and furthermore, the coupling between a neutron and a Weyl fermion is *a priori* unknown. We learned in Sec. 6.2 how to circumvent the problem of the particle-hole continuum, but we still have to deal with the latter issue. To this end, it is beneficial to change the interpretation of the scattering event to one where the neutron magnetic moment reacts to a "magnetic" field induced by transitions of Weyl excitations. In this way, we can understand the effects of Weyl fermions acting on the neutron spin that we control.

The outcome is that a scattered neutron beam is fully polarized in a direction determined by the coupling parameters if an incident beam was fully polarized (see

Sec. 6.4.1). This allows one to cleanly determine the couplings. It is also possible to measure the chirality for inversion-symmetric Weyl nodes (see Sec. 6.4.2).

6.4.1 Pure States of Scattered Neutrons

In a fully polarized experiment, a polarized beam of neutrons with polarization vector $\mathbf{P}^i$ is incident on a Weyl semimetal, and the detector measures the polarization vector $\mathbf{P}^f$ of the scattered beam. The Blume-Maleyev polarization matrix describes the relationship between them. Instead of calculating this, we simplify the discussion and consider, for the moment, a single incident neutron in spin state $|\tau_i\rangle$ and measure whether the scattered neutron is in the state $|\tau_f\rangle$ or in the orthogonal one.

Consider the case where the momentum transfer is the maximum possible for a given energy transfer, i.e., $|\tilde{\mathbf{\Delta}}| = \hbar\omega/v_{\mathrm{F}}$. For a given pure initial spin state of the neutron and a fixed momentum transfer, the cross-section, Eq. (4.1), can be shown (see below) to take the form $\frac{\mathrm{d}^2\sigma(\mathbf{q},\omega)}{\mathrm{d}\Omega \mathrm{d}E_f}\big|_{\tau_i}^{\tau_f} \propto (\hbar\omega/v_{\mathrm{F}})^2 \left|\langle\tau_f|\phi\rangle\right|^2$, where the auxiliary state $|\phi\rangle$ depends on the initial neutron state $|\tau_i\rangle$, direction $\tilde{\mathbf{\Delta}}$, and coupling $\mathbf{F}_\perp^\mu$. In other words, the scattered neutron is in a pure state $|\phi\rangle$. This can be demonstrated experimentally by measuring that there is a certain final state into which the scattering rate is zero. This final neutron state is the time-reversed ket[12] of $|\phi\rangle$, i.e., $|\tau_f^{\mathrm{TR}}\rangle = T|\phi\rangle$, since $\langle\tau_f^{\mathrm{TR}}|\phi\rangle = 0$. Because the neutron spin space is 2-dimensional, the only scattering channel available is the final state $|\phi\rangle = c_1|\uparrow\rangle + c_1|\downarrow\rangle$, where c_1 and c_2 are

[12]Time-reversal operator T on a single-particle state is $T = \theta K$, where K is a conjugation operation and $\theta = \sigma_y$, as explained in Sec. 3.1.1.

expansion coefficients of neutron spin states along the z-direction. Hence, the total cross-section, Eq. (4.1), is,

$$\frac{\mathrm{d}^2\sigma(\mathbf{q},\omega)}{\mathrm{d}\Omega \mathrm{d}E_f}\Big|_{\tau_i}^{\tau_f} \propto (\hbar\omega/v_\mathrm{F})^2|\phi|^2\,. \tag{6.14}$$

The fact that there is only one transition available for a given momentum transfer is *direct* evidence of spin-momentum locking.

The reason for the perfect polarization, in more detail, is that in the extreme limit $|\tilde{\boldsymbol{\Delta}}| \approx \hbar\omega/v_\mathrm{F}$, the set of possible internal momenta degenerates from an ellipsoid to a line. According to Eq. (6.7), all the possible momenta are parallel, and therefore the electron and hole spin states are locked oppositely throughout the whole particle-hole continuum. The scattering amplitude $\langle f_\mathrm{n}, f_\mathrm{w}|H_\mathbf{B}|i_\mathrm{w}, i_\mathrm{n}\rangle \propto \langle \tau_f, f_\mathrm{w}|\boldsymbol{\tau}\cdot\boldsymbol{\mathcal{M}}_\perp(\mathbf{q})|i_\mathrm{w},\tau_i\rangle$ is the same for all pairs, so the integral over the state of the electrons and holes simply gives a multiplicative factor, and the cross-section is proportional to,

$$\frac{d\sigma}{d\Omega} \propto |\langle \tau_f, \chi_f; -\widehat{\tilde{\boldsymbol{\Delta}}}|\boldsymbol{\tau}\cdot\boldsymbol{\mathcal{M}}_\perp|\widehat{\tilde{\boldsymbol{\Delta}}}; -\chi_i, \tau_i\rangle|^2\,, \tag{6.15}$$

where the magnetization $\boldsymbol{\mathcal{M}}_\perp$ is given by Eq. (3.14) and $\boldsymbol{\tau}$ is, as above, the neutron spin operator. The dynamics of the neutron spin may be understood as a precession of the neutron in a magnetic field that depends on how the electron transitions. To see this, we factor this expression as $|\langle\tau_f|\boldsymbol{\tau}|\tau_i\rangle\cdot\langle\chi_f; -\widehat{\tilde{\boldsymbol{\Delta}}}|\boldsymbol{\mathcal{M}}_\perp|\widehat{\tilde{\boldsymbol{\Delta}}}; -\chi_i\rangle|^2$, then define the c-number $\boldsymbol{\mathcal{M}}_{fi} = \langle\chi_f; -\widehat{\tilde{\boldsymbol{\Delta}}}|\boldsymbol{\mathcal{M}}_\perp|\widehat{\tilde{\boldsymbol{\Delta}}}; -\chi_i\rangle$. The transition probability can now be

written as $\frac{d\sigma}{d\Omega} \propto |\langle\tau_f|\boldsymbol{\tau}\cdot\boldsymbol{\mathcal{M}}_{fi}|\tau_i\rangle|^2$. Thus, we may define $|\phi\rangle = \boldsymbol{\mathcal{M}}_{fi}\cdot\boldsymbol{\tau}|\tau_i\rangle$, and the cross-section is given by $|\langle\tau_f|\phi\rangle|^2$ as claimed above. Intuitively, when the electron's spin flips in a particular way, the scattered neutron ends up in a pure state if the incident neutron was initially in a pure state. The final state, $|\phi\rangle$, is obtained by applying the operator $\boldsymbol{\mathcal{M}}_{fi}\cdot\boldsymbol{\tau}$ to the initial state $|\tau_i\rangle$. This mechanism is due to the constant energy contour degenerating into a line, and therefore all particle-hole states in the continuum are perfectly spin-momentum locked. If there were significant curvature, the electron spinors would not all be aligned and the final neutron beam would not be fully polarized. Hence, this mechanism is sensitive to the presence of the term independent of pseudospin in the Weyl equation.

In a realistic neutron scattering experiment, the incident beam consists of many neutrons, rather than just a single neutron as in the above considerations. However, if the incident beam has a polarization vector, $\mathbf{P}^i$, all the neutrons scattered to a certain momentum have the same available scattering channel $|\phi\rangle = \boldsymbol{\mathcal{M}}_{fi}\cdot\boldsymbol{\tau}|\tau_i\rangle$, if the initial neutron beam was fully polarized. As above, this state has expansion coefficients,

$$c_1 = \langle\uparrow|\phi\rangle/|\phi| \quad , \quad c_2 = \langle\downarrow|\phi\rangle/|\phi|\,. \tag{6.16}$$

The neutrons scattered into this direction are *fully polarized* and specified by $\mathbf{P}^f\cdot$

$\boldsymbol{\tau}|\tau_f\rangle = |\tau_f\rangle$, where the polarization vector has the components,

$$P_x^f = 2\Re\left[c_1^* c_2\right] \quad , \quad P_y^f = 2\Im\left[c_1^* c_2\right] \quad , \quad P_z^f = |c_1|^2 - |c_2|^2 \,. \tag{6.17}$$

The polarization vector, Eq. (6.17), is to be understood as a field $\mathbf{P}^f(\tilde{\boldsymbol{\Delta}}/|\tilde{\boldsymbol{\Delta}}|)$ on the surface of the sphere of transferred maximum momentum. An example of a possible measured polarization vector for time-reversal symmetric nodes is plotted in Fig. 6.6.

The matrix element of the magnetization can be evaluated explicitly for time-reversal and inversion symmetric nodes, $\boldsymbol{\mathcal{M}}_{fi} = \widehat{\tilde{\Delta}}_i \mathbf{F}^i_\perp$ and $\boldsymbol{\mathcal{M}}_{fi} = (\hat{u}_j + i\chi\hat{v}_j)\mathbf{F}^j_\perp$, respectively, where χ is the chirality of the node where a hole is created. Here, $\hat{\mathbf{u}}$ and $\hat{\mathbf{v}}$ is an arbitrary pair of vectors making a right-handed coordinate system[13] together with $\widehat{\tilde{\boldsymbol{\Delta}}} = \hat{\mathbf{u}} \times \hat{\mathbf{v}}$. The total cross-section, Eq. (6.14), is proportional to $|\phi|^2$, which is,

$$|\phi|^2 = \widehat{\tilde{\Delta}}_i \widehat{\tilde{\Delta}}_j (\mathbf{F}^{i,*}_\perp \cdot \mathbf{F}^j_\perp + \mathbf{P}^i \cdot \widehat{\mathbf{k}}_0 i \widehat{\mathbf{k}}_0 \cdot \mathbf{F}^{i,*}_\perp \times \mathbf{F}^j_\perp) \,, \tag{6.18a}$$

$$|\phi|^2 = (\delta_{ij} - \widehat{\tilde{\Delta}}_i \widehat{\tilde{\Delta}}_j)\mathbf{F}^i_\perp \cdot \mathbf{F}^j_\perp - \chi \mathbf{P}^i \cdot \widehat{\mathbf{k}}_0 \widehat{\tilde{\Delta}}_k \epsilon_{k\,i\,j} \widehat{\mathbf{k}}_0 \cdot \mathbf{F}^i_\perp \times \mathbf{F}^j_\perp \,, \tag{6.18b}$$

for time-reversal and inversion symmetric nodes, respectively[14]. Notice, that the ex-

[13] The expression for time-reversal symmetric nodes follows from $\langle \hat{\mathbf{n}}|\boldsymbol{\sigma}|\hat{\mathbf{n}}\rangle = \hat{\mathbf{n}}$, where $|\hat{\mathbf{n}}\rangle$ is the spin-$\frac{1}{2}$ state aligned with $\hat{\mathbf{n}}$. The expression for inversion symmetric nodes follows from $\langle -\hat{\mathbf{n}}|\boldsymbol{\sigma}|\hat{\mathbf{n}}\rangle = \hat{\mathbf{u}} + i\hat{\mathbf{v}}$, where the arbitrary vectors $\hat{\mathbf{u}}$ and $\hat{\mathbf{v}}$ are orthogonal vectors and orthogonal to the vector $\hat{\mathbf{n}} = \hat{\mathbf{u}} \times \hat{\mathbf{v}}$. Together, the three vectors satisfy $\sigma_0 = \hat{\mathbf{u}}^{\mathrm{T}}\hat{\mathbf{u}} + \hat{\mathbf{v}}^{\mathrm{T}}\hat{\mathbf{v}} + \hat{\mathbf{n}}^{\mathrm{T}}\hat{\mathbf{n}}$. Notice, that $(\hat{\mathbf{u}} + i\chi\hat{\mathbf{v}})/\sqrt{2}$ is a left- or right-circular polarization vector for $\chi = -1$ and $+1$, respectively.

[14] The results, Eq. (6.18), can be derived in a more direct way, where one interprets the neutron spin and coupling acting together as a generalized force on the Weyl fermions to make transitions. Then, the above result is obtained after evaluating the susceptibility $\chi''^{\mu\,\nu}_{(+)}$ at maximum momentum

pression Eq. (6.18b) is in agreement[15] with the cross-sections Eq. (6.9) and (6.13) in the case where $|\tilde{\mathbf{\Delta}}| = \hbar\omega/v_{\mathrm{F}}$. Notice that $|\phi\rangle$ is not of unit norm.

To summarize, the cross-section in a fully polarized experiment is dependent on the initial neutron beam polarization vector, the scattering direction, and the *a priori* unknown coupling. Measuring the polarization vector of the final neutron beam at $|\tilde{\mathbf{\Delta}}| = \hbar\omega/v_{\mathrm{F}}$, one finds that $|\mathbf{P}^f| = 1$ for all scattering directions and any incident fully polarized neutron beam. This is quite remarkable and counter-intuitive as one is probing particle-hole Weyl pairs.

For time-reversal symmetric nodes, it is not possible to measure the chirality of nodes, since the chirality does not appear in Eq. (6.18a). For inversion-symmetric nodes, it is possible to measure the chirality from the cross-section, Eq. (6.18b), if and only if the coupling $\mathbf{F}^i$ is known. The next section shows that it *is* possible to measure the chirality by other means than Eq. (6.18b), when the coupling is unknown.

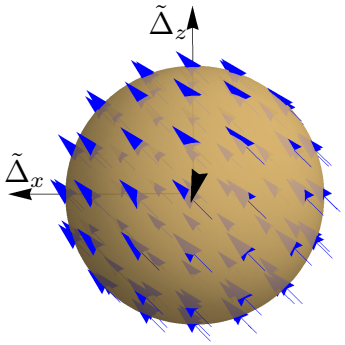

Figure 6.6: Plot of polarization vector, Eq. (6.17), on the surface of a sphere with radius $|\tilde{\mathbf{\Delta}}| = \hbar\omega/v_{\mathrm{F}}$. Initial polarization vector, $|\mathbf{P}^i| = 1$, was chosen arbitrarily, and the couplings are $\mathbf{F}^0 = \mathbf{0}$ and $F^i_j = \delta_{i\,j}$.

transfer. For time-reversal symmetric nodes, it evaluates to $\chi''^{i\,j}_{(+)} \propto (\hbar\omega/v_{\mathrm{F}})^2 \hat{\tilde{\Delta}}_i \hat{\tilde{\Delta}}_j$, whereas for inversion symmetric nodes it evaluates to $\chi''^{i\,j}_{(+)} \propto (\hbar\omega/v_{\mathrm{F}})^2 (\hat{\mathbf{u}} + i\chi\hat{\mathbf{v}})_i (\hat{\mathbf{u}} + i\chi\hat{\mathbf{v}})_j$.

[15]The expression Eq. (6.18a) is also in agreement with the corresponding cross-sections $\Sigma^{(+)}$ and $\mathbf{\Sigma}^{(+)}$ for nodes related by time-reversal symmetry (see Ref. [28]).

6.4.2 Measuring Chiralities of Weyl Fermions

It is possible to measure the chirality of Weyl nodes in an inversion symmetric Weyl semimetal, although it is not straightforward because of the unknown $\mathbf{F}^\mu$ ($\mu = 0, 1, 2, 3$) parameters. It can be easily understood that this is a problem by noticing that chirality χ (where the hole is created) appears in Eq. (6.18b) as $-\chi \mathbf{P}^i \cdot \hat{\mathbf{k}}_0 \widehat{\tilde{\Delta}}_k \epsilon_{k\,i\,j} \hat{\mathbf{k}}_0 \cdot \mathbf{F}^i_\perp \times \mathbf{F}^j_\perp$. Imagine that we perform measurements on two materials with neutrons polarized in the *same* way as they are passed through the materials, which both have nodes $\pm\mathbf{k}_0$ parallel to the z-axis, i.e., $\hat{\mathbf{z}} \cdot \mathbf{F}^i = 0$ for all $i = 1, 2, 3$. If one material has coupling $\mathbf{F}^i_{WSM1} = F^i_x \hat{\mathbf{x}} + F^i_y \hat{\mathbf{y}}$, while the other has $\mathbf{F}^i_{WSM2} = F^i_x \hat{\mathbf{x}} - F^i_y \hat{\mathbf{y}}$ for each i, then it will appear from Eq. (6.18b) as if the materials have the opposite sign of χ, because the sign of $F^i_y \hat{\mathbf{y}}$ differs. In other words, it is possible to compensate for a change in sign of χ by changing the $\mathbf{F}^i$s. To be specific, the cross-section associated with Eq. (6.18b) for scattering on three materials is plotted in Fig. 6.7. Weyl semimetals no. 1 and no. 2 have the same chirality $\chi = -1$, but couplings $\mathbf{F}^i_{WSM1}$ and $\mathbf{F}^i_{WSM2}$, respectively[16]. The cross-section's intensity pattern of material no. 2 is that of material no. 1 if reflected through the $\tilde{\Delta}_x \tilde{\Delta}_y$-plane. From this, one would wrongly conclude that these materials have the opposite chirality. Likewise, a third material has coupling $\mathbf{F}^i_{WSM2}$ but opposite chirality $\chi = 1$. But again, for the same reason as above, one would wrongly conclude that it has the same chirality as material no. 1.

[16]Notice, that the couplings F^x_x and F^y_y of the four-band toy model, Eq. (5.9), were only determined up to a sign, because we expressed them in terms of parameters of the dispersion.

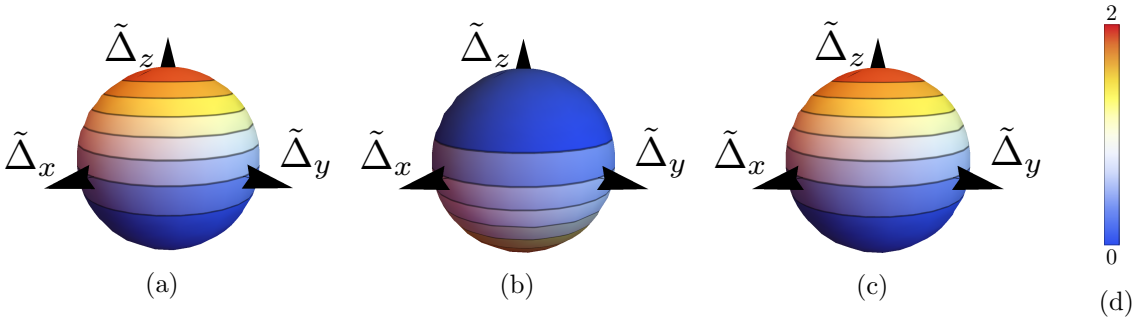

Figure 6.7: Cross-section for a fully polarized measurement on three different Weyl semimetals. Material no. 1, subfig. (a), with coupling $\mathbf{F}^i_{WSM1}$ and chirality $\chi = -1$. Material no. 2, subfig. (b), with $\mathbf{F}^i_{WSM2}$ and $\chi = -1$. Material no. 3, subfig. (c), with $\mathbf{F}^i_{WSM2}$ and $\chi = +1$. The intensity pattern of material no. 2 is that of material no. 1 and 3 when reflected through the $\tilde{\Delta}_x\tilde{\Delta}_y$-plane. Intensity given in subfig. (d).

To get around the aforementioned issue, we will focus on maximum momentum transfer, i.e., $|\tilde{\boldsymbol{\Delta}}| = \hbar\omega/v_{\mathrm{F}}$, as discussed in the last section. From Eq. (6.7) the excitations, i.e., $|i_{\mathrm{w}}\rangle = |\widehat{\tilde{\boldsymbol{\Delta}}}; -\chi_i\rangle$ and $|f_{\mathrm{w}}\rangle = |-\widehat{\tilde{\boldsymbol{\Delta}}}; \chi_f\rangle$, are propagating in opposite directions, but we can reinterpret the excitations as moving in the same direction, $\widehat{\tilde{\boldsymbol{\Delta}}}$, but with opposite spins $-\chi_i$ and $-\chi_f$ since $\chi_i = -\chi_f$. Because the spin and momentum-direction of the excitations in the continuum are fully locked, we may ignore their momentum, and furthermore, simply consider the transition as an electron fixed in space with a neutron scattering off of it. The expression for the cross-section, Eq. (6.15), is then reinterpreted as the cross-section for scattering in which the electron's spin changes from $-\chi_i\tilde{\boldsymbol{\Delta}}$ to $-\chi_f\tilde{\boldsymbol{\Delta}}$, which is always a spin-flip since $\chi_i = -\chi_f$. The interaction operator can be written as,

$$H_{\mathbf{B}}/\mu_B = \boldsymbol{\mathcal{M}}_\perp \cdot \boldsymbol{\tau} = (\boldsymbol{\sigma}\cdot\mathbf{a})\tau_x + (\boldsymbol{\sigma}\cdot\mathbf{b})\tau_y = |\mathbf{a}|\sigma_a\tau_x + |\mathbf{b}|\sigma_b\tau_y\,. \tag{6.19}$$

Here the coupling, Eq. (3.15), is arranged as vectors $\mathbf{a}$ and $\mathbf{b}$ with components $a_i = \mathbf{F}^i_\perp \cdot \hat{\mathbf{x}}$ and $b_i = \mathbf{F}^i_\perp \cdot \hat{\mathbf{y}}$, respectively, and the electron spin Pauli matrices are defined as $\sigma_a = \boldsymbol{\sigma} \cdot \hat{\mathbf{a}}$ and likewise for σ_b. No z-component appears because $\mathbf{F}^i \cdot \hat{\mathbf{k}}_0 = 0$. The $\mathbf{F}^0_\perp$ term of $\boldsymbol{\mathcal{M}}_\perp$ is omitted because it does not contribute to the matrix element for an event in which the electron's spin flips.

The interaction, Eq. (6.19), is unknown because the coupling vectors $\mathbf{a}$ and $\mathbf{b}$ are unknown; they can point in arbitrary directions with any magnitudes. Not only do $\mathbf{a}$ and $\mathbf{b}$ mix components of spin matrices for the neutron, $\boldsymbol{\tau} = (\tau_x, \tau_y, \tau_z)$, and the electron, $\boldsymbol{\sigma} = (\sigma_a, \sigma_b, \sigma_c)$, but also with respect to two *different* coordinate systems. The neutron spin matrices are defined with respect to a right-handed coordinate system with x, y, z-axes. The electron spin matrices, on the other hand, are defined with respect to three axes, a, b and c, which are determined by the coupling, Eq. (3.15), of the Weyl semimetal to neutrons. Furthermore, these a, b, c-axes are *not* required to be orthogonal to one another, nor align with the coordinate system of the neutron. In addition, the component of neutron spin, τ_z, along internode direction does not couple to anything, which is reflected in Eq. (6.19). Notice, that the interaction is not symmetric in $\sigma_c \to -\sigma_c$ despite σ_c not appearing in it. The reason is that spin is a pseudovector and the c-direction is determined by $\sigma_c = -i\sigma_a\sigma_b$. Hence, in order to flip the c-axis, either the a-axis or b-axis should be flipped, but not both. From this, we see that the two couplings $\mathbf{F}^i_{WSM1}$ and $\mathbf{F}^i_{WSM2}$, discussed in the

first paragraph, correspond to a relative sign between the two terms in the interaction Eq. (6.19).

To determine the chirality, we will do experiments where a neutron in spin state $|\tau_i\rangle$ is incident on the target, and the detector filters the scattered neutron in a spin state $|\tau_f\rangle$. What this measures is *not* the electron spin. Actually, what this measures is how the *momentum* $\tilde{\mathbf{\Delta}}$ of the electron changes (by the neutron's momentum transfer), which is locked to the spin of the electron up to a sign (the chirality) that we wish to determine. From the interaction, Eq. (6.19), one would expect a correlation between the electron spin and how the neutron spin has changed. So, we will begin figuring out what one would expect from the interaction between a neutron scattering from an electron spin. We will use this knowledge to understand the actual observed behavior in a real experiment which measures the electron momentum: if the way the electron's *momentum* changes is reversed from the behavior one expects from the spin, it must be because $\chi_i = -\chi_f = 1$, meaning that the spin is antiparallel to the momentum.

The strategy to measure the chirality is to relate the xyz-coordinate system of the neutron to the abc-coordinate system of the electron. For simplicity, let us only consider the intuitive case where the coupling vectors $\mathbf{a}$ and $\mathbf{b}$ are orthogonal to one another with equal magnitudes, i.e., $|\mathbf{a}| = |\mathbf{b}|$. First, we will relate the z- and c-axes, then we relate the xy-plane to the ab-plane, and finally we infer the chirality from

the cross-section measured.

In this case of **a** and **b** vectors, the interaction, Eq. (6.19), can be expressed as $H_{\mathbf{B}}/\mu_B = |\mathbf{a}|(\sigma_-\tau_+ + \sigma_+\tau_-)$, where $\sigma_\pm = (\sigma_a \pm i\sigma_b)/\sqrt{2}$ and $\tau_\pm = (\tau_x \pm i\tau_y)/\sqrt{2}$ are raising and lowering operators of the electron and the neutron spin, respectively. Hence, the sum of each spin component along the axis perpendicular to the plane spanned by the coupling vectors, $\sigma_c + \tau_z$, is conserved. If the neutron flips from up to down, it is not possible for the electron spin to also flip from up to down, since then the net spin would change by $2\hbar$. After all, it is surprising that there is a correlation between flips of the neutron's spin along the z-axis and flips of the electron's spin along the c-axis, since these components of spin operators do not appear in the interaction. The spin conservation along the z- and c-axes reveals how these axes are related, which we will use after the relation between the neutron xy-plane and the electron ab-plane has been established. Unfortunately, there is no spin conservation in the x- and a-axes (and likewise y- and b-axes), as can be seen from,

$$\begin{aligned}
\sigma_a\tau_x + \sigma_b\tau_y|{\rightarrow_a}, {\rightarrow_x}\rangle &= |{\rightarrow_a}, {\rightarrow_x}\rangle - |{\leftarrow_a}, {\leftarrow_x}\rangle\,, \\
\sigma_a\tau_x + \sigma_b\tau_y|{\leftarrow_a}, {\rightarrow_x}\rangle &= |{\leftarrow_a}, {\rightarrow_x}\rangle + |{\rightarrow_a}, {\leftarrow_x}\rangle\,,
\end{aligned}$$

where $|{\rightarrow_x}\rangle$ denotes a neutron spin state prepared parallel to the x-axis, and likewise for the electron.

Hence, we need to find another method to relate the neutron xy-plane and elec-

tron *ab*-plane. This can be done by just focusing on the rate of spin-flip scattering of the neutron, which is automatically accompanied by a spin flip of the electron. So, consider an experiment where the neutron is prepared with a certain incident polarization direction $\hat{\mathbf{N}}$ and one measures the cross-section, $f_{\hat{\mathbf{N}}}(\widehat{\tilde{\mathbf{\Delta}}})$, that it flips to $-\hat{\mathbf{N}}$ as a function of the direction of momentum transfer $\tilde{\mathbf{\Delta}}$. In the end of this subchapter, we will return to this measurement. We begin calculating the probability, $f_{\hat{\mathbf{N}}}(\hat{\mathbf{E}})$, as a function of the direction of the initial *spins* of the neutron and electron, $\hat{\mathbf{N}}$ and $\hat{\mathbf{E}}$, respectively, rather than momentum $\widehat{\tilde{\mathbf{\Delta}}}$. Recall, that the initial spin of the electron is related to momentum by $\hat{\mathbf{E}} = -\chi_i \widehat{\tilde{\mathbf{\Delta}}}$. We can use $f_{\hat{\mathbf{N}}}(\hat{\mathbf{E}})$ instead of $f_{\hat{\mathbf{N}}}(\widehat{\tilde{\mathbf{\Delta}}})$ to determine the electron *a*- and *b*-axes because these axes can only be determined up to an overall sign, meaning that factor $-\chi_i$ cannot be resolved from knowing the *a*- and *b*-axes. The probability of the electron flipping from $\hat{\mathbf{E}}$ to $-\hat{\mathbf{E}}$ and the neutron flipping from $\hat{\mathbf{N}}$ to $-\hat{\mathbf{N}}$ comes out to be[17],

$$f_{\hat{\mathbf{N}}} \propto \left|\langle -\hat{\mathbf{N}}, -\hat{\mathbf{E}}|(\boldsymbol{\sigma}\cdot\mathbf{a})\tau_x + (\boldsymbol{\sigma}\cdot\mathbf{b})\tau_y|\hat{\mathbf{E}},\hat{\mathbf{N}}\rangle\right|^2, \tag{6.20a}$$

$$= |\mathbf{a}|\left[(N_x E_a + N_y E_b)^2 + (N_z - E_c)^2\right], \tag{6.20b}$$

where E_a, E_b, E_c are the components of $\hat{\mathbf{E}}$ along the directions of $\hat{\mathbf{a}}, \hat{\mathbf{b}}$, and a third direction, $\hat{\mathbf{c}}$, forming a right-handed coordinate system $\hat{\mathbf{c}} = \hat{\mathbf{a}} \times \hat{\mathbf{b}}$. A striking effect is

[17]To show, this one uses $\langle -\hat{\mathbf{n}}|\boldsymbol{\sigma}|\hat{\mathbf{n}}\rangle = \hat{\mathbf{u}} + i\hat{\mathbf{v}}$, where $|\hat{\mathbf{n}}\rangle$ is a spinor oriented along the $\hat{\mathbf{n}}$ direction of the Bloch sphere, and the two arbitrary unit vectors $\hat{\mathbf{u}}$ and $\hat{\mathbf{v}}$ are making a right-handed coordinate system together with $\hat{\mathbf{n}} = \hat{\mathbf{u}} \times \hat{\mathbf{v}}$. Together, these three unit vectors satisfy a completeness identity $\hat{\mathbf{u}}^{\mathrm{T}}\hat{\mathbf{u}} + \hat{\mathbf{v}}^{\mathrm{T}}\hat{\mathbf{v}} + \hat{\mathbf{n}}^{\mathrm{T}}\hat{\mathbf{n}} = \sigma_0$. We have such relations for both the neutron $(\hat{\mathbf{u}}_n, \hat{\mathbf{v}}_n, \hat{\mathbf{N}})$ and electron $(\hat{\mathbf{u}}_e, \hat{\mathbf{v}}_e, \hat{\mathbf{E}})$.

that for any direction of the initial neutron spin, $\hat{\mathbf{N}}$, there are two initial spin directions of the electron, $\hat{\mathbf{E}}$, for which spin-flips of the neutrons have zero probability. In other words, the probability, Eq. (6.20b), considered as a function of electron spin, $\hat{\mathbf{E}}$, will have nodes where the cross-section is zero, i.e., $f_{\hat{\mathbf{N}}}(\hat{\mathbf{E}}) = 0$. Notice that these zero nodes will be perfect and located at,

$$E_a = \pm N_y \quad , \quad E_b = \mp N_x \quad , \quad E_c = N_z \tag{6.21}$$

in the electron spin space.

To find the relation between the neutron x, y-axes and the electron a, b-axes, we perform a series of measurements with initial neutron polarization in the xy-plane, i.e., $N_z = 0$. According to Eq. (6.21), for a given neutron polarization, this will create two cross-section zero nodes in the electron ab-plane as a function of $\hat{\mathbf{E}}$. These cross-section zero nodes will always be equal and opposite to each other on the equatorial circle of a $|\hat{\mathbf{E}}| = 1$ sphere. Thus, although a real experiment measures nodes as a function of momentum, $\hat{\tilde{\mathbf{\Delta}}}$, it also reveals where the nodes as a function of electron spin, $\hat{\mathbf{E}}$, are. In general, the neutron xy-plane and electron ab-plane will be rotated with respect to each other.

The electron a- and b-axes are unknown, but according to the Eq. (6.21), we can find them up to an ambiguity in their directions by two measurements. A measurement with neutron polarization $\hat{\mathbf{N}} = (1, 0, 0)$ will create two zero cross-section

nodes at $\hat{\mathbf{E}} = (0, \mp 1, 0)$, i.e., we have located the b-axis but not its positive direction. Likewise, a measurement with neutron polarization $\hat{\mathbf{N}} = (0, 1, 0)$ will create two zero cross-section nodes at $\hat{\mathbf{E}} = (\pm 1, 0, 0)$, which is on the a-axis, but again the positive direction is ambiguous. The neutron polarization of these two measurements is illustrated in Fig. 6.8(a), and the corresponding electron nodes are illustrated in Fig. 6.8(b). Since the a-and b axes' orientation relative to each other is still undetermined, we do not yet have a way to refer to any point in the electron ab-plane by specifying its position with respect to the a- and b-axes. For this reason, we arbitrarily superimpose a north-south-east-west reference system on the ab-plane as indicated in Fig. 6.8(b).

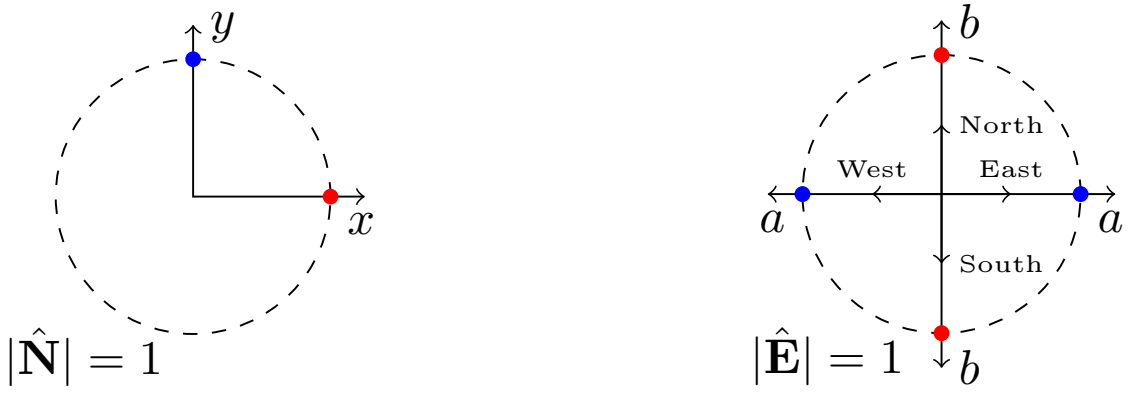

(a) Neutron polarization

(b) Nodes of the electron spin

Figure 6.8: Two measurements with initial neutron polarization in the xy-plane in subfig. (a) are indicated by colored dots. The corresponding zero nodes of the electron spin in the ab-plane are illustrated in subfig. (b). The directions of the a- and b-axes are undetermined. For later reference, is arbitrarily superimposed on top of the ab-plane a north-south-east-west reference system.

The ambiguity in the relative orientation of the electron a- and b-axes is only present when doing two measurements with $\hat{\mathbf{N}} = (1, 0, 0)$ and $\hat{\mathbf{N}} = (0, 1, 0)$. To deter-

mine the relative orientation of the a- and b-axes, we perform a third measurement with neutron polarization at -45 degrees, $\hat{\mathbf{N}} = (1, -1, 0)/\sqrt{2}$, which is illustrated in Fig. 6.9(a). This will create two nodes in the electron ab-plane at $\hat{\mathbf{E}} = \mp(1, 1, 0)/\sqrt{2}$. To plot these electron zero nodes in the ab-plane, we need to specify the orientation of the a- and b-axes; there are two sets of orientations that satisfy $\hat{\mathbf{E}} = \mp(1, 1, 0)/\sqrt{2}$: either a-axis points towards the east and b-axis points towards the north, or a-axis points towards the west while b-axis points towards the south, as illustrated in Figs. 6.9(b) and 6.9(c), respectively. The cross-section cannot measure the overall sign of the a- and b-axes, but only their relative orientation. We can therefore simply define the electron a-and b-axes to be those in Fig. 6.9(b).

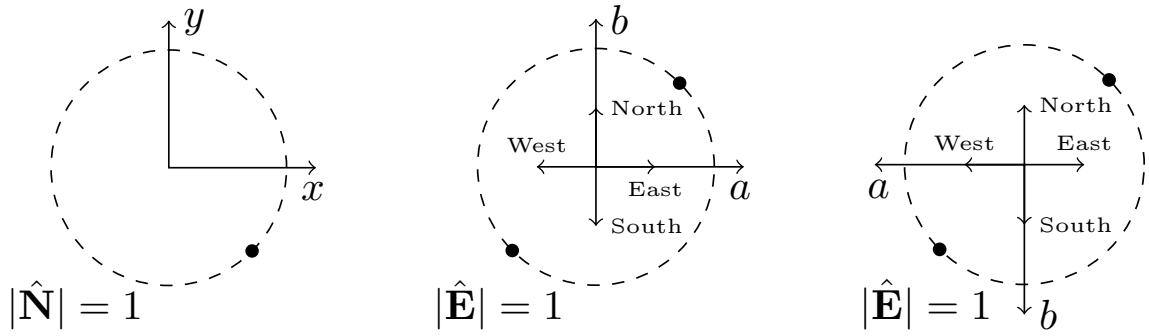

(a) Neutron polarization

(b) Nodes of the electron spin

(c) Nodes of the electron spin

Figure 6.9: A measurement with initial neutron polarization at -45 degrees is illustrated in subfig. (a). The corresponding electron zero nodes in the ab-plane determine the orientation of the a- and b-axes. The two possibilities are illustrated in subfig. (b) and (c), respectively.

Once we know the directions of the electron a-and b-axes, we can figure out the direction of the c-axis because spin is always defined in a right-handed coordinate sys-

tem. This means that the c-axis is simply found from $\hat{\mathbf{c}} = \hat{\mathbf{a}} \times \hat{\mathbf{b}}$, since flipping both the a-and b-axes does not change the c-axis direction. Hence, even though we only determined the a- and b-axes up to an overall sign, we know the c-axis completely. Alternatively, the c-axis can be found by moving the neutron polarization out of the xy-plane, i.e., $N_z > 0$. The electron zero nodes will move out of the ab-plane as $E_c = N_z$. These zero nodes will no longer be antipodal to one another, but will be located oppositely on a small circle of the electron $|\hat{\mathbf{E}}|^2 = 1$ sphere. The hemisphere that the nodes move into is in the direction of the positive c-direction.

The orientation of the electron abc-coordinate system relative to the neutron xyz-coordinate system has been established. With this, we can infer the chirality of the Weyl nodes from a real experiment. First, recall that the above procedure predicted the zero cross-section nodes for the initial electron spin $\hat{\mathbf{E}}$. However, the real experiment does not measure $\hat{\mathbf{E}}$ but rather $\widehat{\tilde{\mathbf{\Delta}}}$, which is related to spin by $\hat{\mathbf{E}} = -\chi_i \widehat{\tilde{\mathbf{\Delta}}}$. This means that $\widehat{\tilde{\mathbf{\Delta}}}$ is parallel to $\hat{\mathbf{E}}$ if $\chi_i = -1$, and antiparallel if $\chi_i = 1$.

In a real experiment, the electron zero cross-section nodes, Eq. (6.20b), are measured as a function of $\widehat{\tilde{\mathbf{\Delta}}}$, i.e., where $f_{\hat{\mathbf{N}}}(\widehat{\tilde{\mathbf{\Delta}}}) = 0$. By moving the initial neutron polarization out of the xy-plane, i.e., $N_z > 0$, the electron zero nodes will move out of the ab-plane. The nodes will no longer be antipodal to one another, but will be located oppositely on a small circle of the electron $|\widehat{\tilde{\mathbf{\Delta}}}|^2 = 1$ sphere. The question is, will the electron zero cross-section nodes as a function of momentum $\widehat{\tilde{\mathbf{\Delta}}}$ move in the

positive or negative c-direction? By observing this, we can infer the chirality because the direction of the c-axis is defined by the electron spin. If the electron zero nodes in the real experiment move towards the positive c-direction (predicted from the electron spin), then $\widehat{\tilde{\mathbf{\Delta}}}$ is parallel to $\hat{\mathbf{E}}$, meaning that chiralities are $\chi_i = -\chi_f = -1$. On the other hand, if the nodes move towards the negative c-direction, then $\widehat{\tilde{\mathbf{\Delta}}}$ is antiparallel to $\hat{\mathbf{E}}$, meaning that chiralities are $\chi_i = -\chi_f = 1$. These two possibilities are illustrated in Figs. 6.10(a) and 6.10(b), respectively.

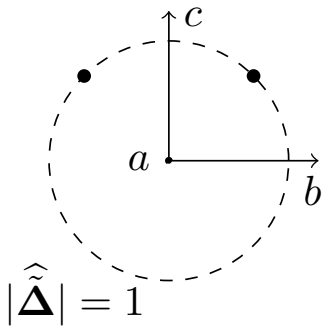

(a) Cross-section zero nodes for $\chi_i = -\chi_f = -1$

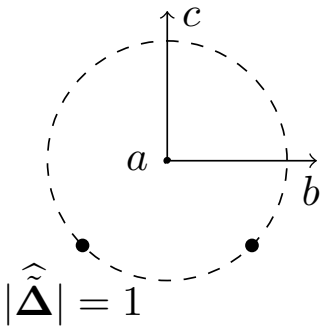

(b) Cross-section zero nodes for $\chi_i = -\chi_f = +1$

Figure 6.10: Measurement of chirality. For a measurement with initial neutron polarization out of the xy-plane, $N_z > 0$, the corresponding cross-section zero nodes moves either towards the positive or negative c-direction determined in Fig. 6.9(b) depending on the chirality of the Weyl excitations. The two possibilities are illustrated in subfigs. (a) and (b).

In general, for any two vectors **a** and **b** with arbitrary magnitudes that are not parallel to one another, the same routine (with slight modifications) allows one to measure the chirality (see Ref. [28]). However, the difference to the case described here, is that the total spin along z- and c-axes are not exactly conserved. So after

all, spin conservation along z- and c-axes is not absolutely necessary in order to measure chirality. The ability to measure chirality is due to two things: a correlation between spin-flips along the z- and c-axes, together with a relation between the xy- and ab-planes (by relating electron zero cross-section nodes to neutron polarization). In the degenerate case where **a** and **b** are parallel, while spin is conserved along that direction, it is not possible to relate the xy- and ab-planes by the method outlined here. It is therefore not possible to measure the chirality by this method when **a** and **b** are parallel.

A few final comments about this method are in order. Because the method relies on finding zero nodes of the cross-section, this method is not resilient to the presence of non-Weyl fermion background scattering channels in the total cross-section. Unless background scattering can be entirely removed in the region of Weyl fermion scattering, it will be difficult to locate a node of zero cross-section. We do not pretend that this method is practical, but it is a proof of principle that inelastic neutron scattering can measure the chirality of inversion symmetric nodes. It is likely that another experimentally more useful method can be found, partly because this method only considered neutron spin-flip processes. To this end, it may be useful to calculate the full Blume-Maleyev polarization cross-section (relating initial and scattered neutron polarizations vectors), which could be analyzed for stable patterns (similar to Ch. 6.3.1) reflecting the chirality of nodes. Alternatively, the method outlined here

suggests that from the Blume-Maleyev polarization cross-section, one could measure the chirality by including neutron spin-flip processes.

Chapter 7

Conclusion and Discussion

Weyl semimetals are recently discovered, fascinating states of matter, partly because their bulk excitations are condensed matter physics' incarnation of Weyl fermions in high-energy physics, but also because their stability is topologically protected. The manifestation of their bulk topology leads to a plethora of new fundamental phenomena, such as topological surface states and responses in applied electromagnetic fields, which are promising candidates for future applications. For these reasons, the research of Weyl semimetals is broadly classified into three categories: engineering of Weyl semimetals, predicting responses to applied fields, and detection of either of these. This dissertation attempts to span the latter two fields. The primary goal was to show that it is possible for inelastic neutron scattering to probe bulk excitations of type-1 Weyl nodes. The secondary goal was to investigate the response of Weyl nodes to a magnetic field to look for new phenomena in Weyl semimetals.

As the development of most new theories begins with simple case studies, so too does ours. However, while we assumed the Weyl nodes to be aligned at (or near) the chemical potential, and a vanishing term independent of pseudospin, $\mathbf{v}_0$, in the Weyl equation, the nodes were allowed a realistic anisotropy. These assumptions are not overly simplistic, and in fact, many of the desirable predictions of Weyl semimetals rely on exactly the same assumptions. In addition, these assumptions offer a good starting point for understanding neutron scattering from Weyl semimetals. This is because the pseudospin susceptibility is Lorentz invariant, which has several interesting and useful consequences: the dynamics of the excitations have relativistic symmetry, and the cross-section can therefore easily be calculated by using Lorentz invariance. Furthermore, this is reflected in the cross-section by a discontinuous edge of the region of scattering, which is both measurable and a strong signature of scattering Weyl fermions, because non-Weyl fermion background scattering is expected to be continuous.

The predictions of this theory (summarized below) are shown to be stable against a small, $|\mathbf{v}_0|/v_\mathrm{F} \ll 1$, breaking of Lorentz invariance of Weyl nodes. It has not been investigated how a larger $|\mathbf{v}_0|/v_\mathrm{F}$ influences the theory, but such an analysis can be done by calculating the corresponding cross-section. Reference [28] outlines how the cross-section for scattering off any type-1 Weyl semimetal, $|\mathbf{v}_0|/v_\mathrm{F} < 1$, is analytically tractable.

The ability to measure the predictions of this theory rely on the Weyl fermion scattering channel being cleanly isolated from background scattering channels, and the principal axis transformation $\mathcal{T}$ being measured in an experiment. Yet, in any real experiment there will always be background channels in the measured cross-section. Whether it is possible to cleanly separate the Weyl fermion and background channels and to measure $\mathcal{T}$, therefore depends on the relative strength of the Weyl fermion scattering channel to background channels. As the magnitudes of the background channels can only be estimated for real materials (and they are very compound specific), estimates of these have therefore been left out. On the other hand, the strength of the Weyl fermion scattering cross-section can be calculated for any type-1 Weyl semimetal, if its band structure is available, by using Eq. (3.15) to calculate the coupling of Weyl fermions to neutrons.

Many well-versed physicists would entirely dismiss taking up a project like this, because of the simple reason that the density of states of a Weyl node is low for small energies, and the fact that neutron scattering is known to have difficulties probing electronic excitations of semimetals due partly to this. In addition, a close examination reveals that probing Weyl fermions with neutron scattering faces a multitude of conceptual issues about the prospects of measuring properties of Weyl fermions, such as spin-momentum locking, and the chirality of excitations when a whole Weyl particle-hole continuum is contributing to the measured response. Furthermore, the

Weyl fermion pseudospin is not related to real spin in a definitive way. This means that the amplitude for a change in the neutron and Weyl fermion spin is a linear combination of material specific parameters analog to the $\frac{g}{2}$-factor of an electron. Therefore, there is no simple analog of spin-conservation for a neutron scattering from a Weyl fermion. Moreover, these material-dependent g-factors are *a priori* unknown and can be given by 8 and 12 independent parameters for time-reversal and inversion symmetric nodes, respectively.

Understanding the depth of the aforementioned insurmountable challenges provided the keys to circumvent them. After all, this is perhaps the most intriguing aspect of this work. The construction of the cross-section separated it into a Lorentz invariant susceptibility and a symmetry breaking coupling of neutrons to Weyl fermions determined by *a priori* unknown material specific g-factors. This had advantages: first, the scattering process was thereby mapped to a relativistic process. Lorentz invariant properties of the susceptibility, describing the excitations' dynamics, are reflected in the cross-section. Most noteworthy is that the region of scattering has a discontinuous edge. This allows one to control the momentum of the particle-hole pairs by focusing on the maximum momentum transfer for a given energy, then both excitations must end up moving parallel to the transferred momentum. Thus, their spin states are uniquely determined. Under this situation, one can see the spin-momentum locking especially clearly. For example, if the initial neutron beam is perfectly polar-

ized, then the scattered beam is rotated in a definite direction by the g-factors, so it remains perfectly polarized. Furthermore, despite the arbitrary material parameters, it is possible to measure the chirality for inversion symmetric nodes. That is, one can measure whether the excitations' momenta are parallel or antiparallel to their pseudospin, even though one can only measure the pseudospin through its interaction with the neutron determined by unknown arbitrary g-factors, which reflect its topological character. The second advantage lies in the anisotropy of the g-factors, as they render spin-momentum locking observable even in a fully unpolarized experiment. In principle, the simple fact of observing any neutron momentum transfer dependence in the Weyl fermion scattering cross-section is a signature of probing spin-momentum locking. Furthermore, the g-factors can enhance the cross-section intensity as they, in principle, can take any value from zero to diverging, which differs from the single bare coupling value $\frac{g}{2} = 1$. As a proof of concept, we estimated the intensity under optimistic conditions to be $q_i/q_f \times \mathrm{d}^2\sigma^{(+)}(\mathbf{q},\omega)/\mathrm{d}\Omega\mathrm{d}E_f \lesssim 2 \times 10^{-2}$ mb/meV f.u. sr for a toy model. This is low but remarkably only of order $10^{-2} - 1$ smaller than what *has* been observed in scattering off spin-$\frac{1}{2}$ particle-hole pair related phenomena [82, 83, 84, 85, 86].

Inelastic neutron scattering can thus provide a platform to understand the intrinsic behavior of Weyl semimetals, such as the spin and orbital effects discussed here. It can test the form of the Weyl equation in materials including monitoring changes in it such as: relocation in energy and momentum space, distortion of dispersion,

redistribution of occupation numbers due to applied fields, currents, or elastic and magnetic deformations as predicted in Ref. [88, 89, 90, 91, 92, 93].

Some of the details that have appeared in this careful study could give new information about Weyl materials. For example, the many g-factors describing the emergent magnetic moment of the Weyl fermions show how Weyl fermions couple to an external magnetic field, which does not have to be from a neutron. In particular, it would be interesting to study how these parameters evolve as a realistic magnetic Weyl semimetal approaches the transition point [6, 94, 95, 96, 97]. The four-band model shows that they depend on the strength of the spontaneous magnetic ordering and hybridization between bands, and they diverge near the transition point, at least in this model. These g-factors can be determined theoretically for any type-1 Weyl semimetal, by using Eq. (3.15), if the band structure is available. The cross-sections presented in this dissertation show that the g-factors can be measured in inelastic neutron scattering experiments.

Besides the specific problem of neutron scattering, particle-hole correlators (as calculated here) are relevant to Weyl semimetals' intrinsic properties. For example, particle-hole bound states (like plasma waves) might form, and their self-energy is closely related to the pseudospin-susceptibility. If a particle-hole bound state from excitations at distinct Weyl points can form, we would expect strong angular momentum-dependent properties. For example, it should have an effective mass

that is proportional to the matrix elements between the two Weyl points and hence would be strongly momentum dependent. Also, just as there is an emergent magnetic moment of Weyl excitations, there could be an emergent electric dipole moment, which is not ruled out by symmetry unlike the case of an electron in free space [98]. This could influence the bound state's dynamics through pseudospin dipole-dipole interactions. It is necessary to understand carefully what properties of Weyl fermions are universal for such analyses, and the relativistic method developed here should be useful.

Furthermore, it would be interesting to extend our method to derive the cross-section for scattering between emergent Bogoliubov-de Gennes Weyl nodes induced in a monopole superconducting Weyl semimetal [99].

In conclusion, the theory developed here provides helpful guidelines for the neutron scattering community to probe electronic excitations in type-1 Weyl semimetals by elaborating suitable ways to manipulate cross-section data. From a broader perspective, our work constitutes an important development in the burgeoning field of topological semimetals by opening an unexpected avenue in the studies of these, as this experimental tool resolves properties other techniques cannot.

Appendix A

Symmetry Constraints on Couplings

In 2^{nd} quantization, the Hamiltonian in $\mathbf{r}$-representation of the i^{th} Weyl node is $H_i = \int \mathrm{d}\mathbf{r}\, \Psi_i^\dagger(\mathbf{r},t) H_{0,i}(\boldsymbol{\nabla}_\mathbf{r}) \Psi_i(\mathbf{r},t)$, where $\Psi_i(\mathbf{r},t)$ is the 2^{nd} quantized Weyl fermion field, and $H_{0,i}$ is on the 1^{st} quantized isotropic form Eq. (3.5) with momentum $\tilde{\mathbf{k}}$ replaced by $-i\hbar\boldsymbol{\nabla}_\mathbf{r}$. The interaction for scattering between nodes is given by $H_\mathbf{B} = \int \mathrm{d}\mathbf{r}\, \mathcal{H}_\mathbf{B}(\mathbf{r},t)$, where interaction density is $\mathcal{H}_\mathbf{B}(\mathbf{r},t) = -\mathbf{M}(\mathbf{r},t)\cdot\mathbf{B}(\mathbf{r})$ with magnetization Eq. (3.13). For scattering between nodes related by either time-reversal or inversion symmetry [32, 57, 100], the coupling is constrained, as will be explained in Appendix A.1 and A.2, respectively.

A.1 Time-reversal Symmetric Nodes

Let $\hat{\tau}$ denote the antiunitary time-reversal operator acting on Ψ_i. Weyl nodes related by time-reversal symmetry is the requirement $\hat{\tau}H_2\hat{\tau}^{-1} = H_1$, and the fields are therefore related by,

$$\hat{\tau}\Psi_2\hat{\tau}^{-1} = \theta^\dagger\Psi_1 \quad , \quad \hat{\tau}\Psi_1\hat{\tau}^{-1} = -\theta^*\Psi_2, \tag{A.1a}$$

$$\hat{\tau}\Psi_2^\dagger\hat{\tau}^{-1} = \Psi_1^\dagger\theta \quad , \quad \hat{\tau}\Psi_1^\dagger\hat{\tau}^{-1} = \Psi_2^\dagger(-\theta^T). \tag{A.1b}$$

Here $\hat{\tau}\Psi_2\hat{\tau}^{-1} = \theta^\dagger\Psi_1$ is the definition of time-reversal symmetric fields, whereas $\hat{\tau}\Psi_1\hat{\tau}^{-1} = -\theta^*\Psi_2$ follows by applying $\hat{\tau}^2\Psi_1\hat{\tau}^{-2}$ to an arbitrary state $|\alpha\rangle$ with n_w Weyl fermions. The remaining two follow from these by Hermitian conjugation. The 1^{st} quantized Hamiltonians are thus related by $H_{0,1}(\boldsymbol{\nabla}_\mathbf{r}) = \theta H^*_{0,2}(\boldsymbol{\nabla}_\mathbf{r})\theta^\dagger$, for any choice of θ up to a unitary matrix. Hence, by defining $H_{0,2}$ we can find the time-reversal symmetric $H_{0,1}$. Here we choose $\theta = \sigma_y$ as it brings both nodes to the standard isotropic form Eq. (3.5) with same chirality $\chi_1 = \chi_2$. Since the external magnetic field $\mathbf{B}$ is odd under time-reversal transformation, a symmetry of the theory is the time-reversal of the interaction with reversed magnetic field. Thus, we require that $\mathcal{H}_\mathbf{B} = \hat{\tau}\mathcal{H}_{-\mathbf{B}}\hat{\tau}^{-1}$, which implies that the coupling strengths are restricted to Eq. (6.1).

To derive Eq. (6.1) above, we tacitly used that $\hat{\tau}\mathbf{B}\hat{\tau}^{-1} = \mathbf{B}$, but how can that be? After all, the interaction $H_\mathbf{B}$ between a neutron and nodes involves the neutron's magnetic field $\mathbf{B}(\mathbf{r})$, induced by its magnetic moment $\boldsymbol{\mu}_\mathrm{n}$, which is *odd* under time-

reversal symmetry. Mathematically that is $\tilde{\tau}\mathbf{B}\tilde{\tau}^{-1} = -\mathbf{B}$, since a spinning current loop changes direction under time-reversal, where the time-reversal operator acting on the neutron is $\tilde{\tau}$. The point is, that we do not want to find the operator $\tilde{\tau}$, but only the time-reversal operator $\hat{\tau}$ acting on the neutron coupling to nodes. Hence, the trick is to utilize the fact that $\tilde{\tau}\mathbf{B}\tilde{\tau}^{-1} = -\mathbf{B}$ by inserting this minus sign by hand while simultaneously treating the magnetic field $\mathbf{B}$ as unaffected (does not get conjugated and does not change sign) by the operator $\hat{\tau}$, i.e., $\hat{\tau}\mathbf{B}\hat{\tau}^{-1} = \mathbf{B}$, which is treating the magnetic field components as real classical numbers. Therefore, the symmetry constraint is $\mathcal{H}_{\mathbf{B}} = \hat{\tau}\mathcal{H}_{-\mathbf{B}}\hat{\tau}^{-1}$.

A.2 Inversion Symmetric Nodes

Let $\hat{\rho}$ denote the unitary inversion operator acting on Ψ_i. Weyl nodes related by inversion symmetry is the requirement $\hat{\rho}H_2\hat{\rho}^{-1} = H_1$, and the fields are therefore related by,

$$\hat{\rho}\Psi_2\hat{\rho}^{-1} = \theta^\dagger\Psi_1 \quad , \quad \hat{\rho}\Psi_1\hat{\rho}^{-1} = \theta\Psi_2, \tag{A.2a}$$

$$\hat{\rho}\Psi_2^\dagger\hat{\rho}^{-1} = \Psi_1^\dagger\theta \quad , \quad \hat{\rho}\Psi_1^\dagger\hat{\rho}^{-1} = \Psi_2^\dagger\theta^\dagger. \tag{A.2b}$$

Here $\hat{\rho}\Psi_2\hat{\rho}^{-1} = \theta^\dagger\Psi_1$ is the definition of inversion symmetric fields, whereas $\hat{\rho}\Psi_1\hat{\rho}^{-1} = \theta\Psi_2$ follows from $\hat{\rho}^2 = 1$ and $\hat{\rho}^{-1} = \hat{\rho}^\dagger$. The remaining two follow from these by Hermitian conjugation. The 1^{st} quantized Hamiltonians are thus related by

$H_{0,1}(-\boldsymbol{\nabla}_{\mathbf{r}}) = \theta H_{0,2}(\boldsymbol{\nabla}_{\mathbf{r}})\theta^{\dagger}$, so by defining $H_{0,2}$ we can find the inversion symmetric $H_{0,1}$. This holds for any choice of θ, arbitrary up to a unitary one. Here we choose $\theta = \sigma_0$ as it brings both nodes to the standard isotropic form Eq. (3.5) with opposite chirality $\chi_1 = -\chi_2$. Since the external magnetic field $\mathbf{B}$ is even under inversion transformation, a symmetry of the theory is $\mathcal{H}_{\mathbf{B}} = \hat{\rho}\mathcal{H}_{\mathbf{B}}\hat{\rho}^{-1}$, which implies that the coupling strengths are restricted to Eq. (6.2).

Appendix B

Susceptibility for Time-reversal Symmetric Nodes

For time-reversal symmetric nodes, the matrix element Eq. (3.19) connects only nodes with same chirality, i.e., $\chi_i = \chi_f \equiv \chi$. One now seeks 4×4 operators with the same properties and finds that $\gamma^0\gamma^\mu$ also connects nodes with the same chirality. The susceptibility Eq. (3.19) can be rewritten in terms of this operator by transforming from 2-spinors to 4-spinors, where it is given by,

$$T^{\mu\,\nu}_{\chi\to\chi}(\mathrm{Q}) \;\to\; (-1)^{\xi_\chi}\tilde{T}^{\mu\,\nu}_{\chi\to\chi}(\mathrm{Q})\,, \tag{B.1a}$$

$$\tilde{T}^{\mu\,\nu}_{\chi\to\chi}(\mathrm{Q}) \;=\; c\int\frac{\mathrm{d}^3\,\tilde{\mathbf{p}}_i}{2\tilde{p}_i^0}\int\frac{\mathrm{d}^3\,\tilde{\mathbf{p}}_f}{2\tilde{p}_f^0}\,\delta^{(4)}\left(\mathrm{Q}-\mathrm{P}\right)\,\Upsilon^{\mu\,\nu}_{\chi\to\chi}. \tag{B.1b}$$

APPENDIX B. SUSCEPTIBILITY FOR TIME-REVERSAL SYMMETRIC NODES

Here the amplitude is $\Upsilon^{\mu\,\nu}_{\chi\to\chi} = 2\tilde{p}_i^0 2\tilde{p}_f^0\, \bar{u}^{\chi}_{\tilde{\mathbf{p}}_i}\gamma^\mu u^{\chi}_{\tilde{\mathbf{p}}_f}\bar{u}^{\chi}_{\tilde{\mathbf{p}}_f}\gamma^\nu u^{\chi}_{\tilde{\mathbf{p}}_i}$, constant $c = \pi V/v_{\mathrm{F}}(2\pi\hbar)^3$, $\xi_R = 0$ for any μ,ν, whereas $\xi_L = 0$ if $\mu = \nu = 0$ or $\mu,\nu \neq 0$, otherwise 1. The matrix element $\tilde{T}^{\mu\,\nu}_{\chi\to\chi}(\mathrm{Q})$ is a Lorentz-invariant rank-2 tensor and by dimensional analysis is quadratic in Q, thus the most general form it can have is,

$$\tilde{T}^{\mu\,\nu}_{\chi\to\chi}(\mathrm{Q}) = a_\chi\,(\mathrm{Q}\cdot\mathrm{Q})\,g^{\mu\,\nu} + b_\chi \mathrm{Q}^\mu\mathrm{Q}^\nu\,, \tag{B.2}$$

where $g^{\mu\,\nu} = \mathrm{diag}(1,-1,-1,-1)$ is the Minkowski metric. The scalars a_χ and b_χ can be determined from the two contractions,

$$g_{\mu\,\nu}\tilde{T}^{\mu\,\nu}_{\chi\to\chi}(\mathrm{Q}) = (4a_\chi + b_\chi)\,\mathrm{Q}\cdot\mathrm{Q}\,, \tag{B.3a}$$

$$\mathrm{Q}_\mu\mathrm{Q}_\nu\tilde{T}^{\mu\,\nu}_{\chi\to\chi}(\mathrm{Q}) = (a_\chi + b_\chi)\,(\mathrm{Q}\cdot\mathrm{Q})^2\,. \tag{B.3b}$$

In a frame where Q is time-like $\tilde{\mathrm{Q}}^\mu = (\tilde{\mathrm{Q}}^0, \mathbf{0})$–i.e., the center-of-momentum (COM) frame of the particle-hole pair, the conservation laws lead to a simple integral over the surface of a sphere where the contractions can easily be calculated. Let us break this down step by step.

Introducing projectors helps to carry out the calculations. Because we have performed a particle-hole transformation, all states have positive energy, and therefore, the only relevant projectors are,

$$2\tilde{p}^0 u^{\chi}_{\tilde{\mathbf{p}}}\bar{u}^{\chi}_{\tilde{\mathbf{p}}} = p_\chi\, p_+(\tilde{p})\gamma^0, \tag{B.4}$$

which project into positive energy states with chirality $\chi = (L, R)$ by p_+ and p_χ, respectively, given by $p_+(\tilde{p}) = \tilde{p}^0 + \gamma^0 \boldsymbol{\gamma}\cdot\tilde{\mathbf{p}}$, $p_L = (\mathbb{1}_{4\times4} - \gamma^5)/2$ and $p_R = (\mathbb{1}_{4\times4} + \gamma^5)/2$. Note that the projector is a Lorentz scalar since $p_+(\tilde{p})\gamma^0 = p^\mu\gamma_\mu$ and is therefore not technically a projector, but constructed to make Eq. (B.1b) Lorentz invariant. Now we can use the COM frame, in which $\tilde{\mathbf{p}}_i = -\tilde{\mathbf{p}}_f$, and express $\Upsilon^{\mu\,\nu}_{\chi\to\chi}(\tilde{Q}) = \mathrm{Tr}[\gamma^\mu p_\chi p_+(-\tilde{\mathbf{p}}_i)\gamma^\nu p_\chi p_+(\tilde{\mathbf{p}}_i)]$ as a trace over gamma matrices. By use of standard trace technology [31], we find $g_{\mu\nu}\Upsilon^{\mu\,\nu}_{\chi\to\chi}(\tilde{Q}) = -8|\tilde{\mathbf{p}}_i|$ and $\tilde{Q}_\mu\tilde{Q}_\nu\Upsilon^{\mu\,\nu}_{\chi\to\chi}(\tilde{Q}) = 0$. Using these latter two expressions in Eq. (B.3), evaluated in the COM frame and performing the spherical integral of Eq. (B.1b), determines the scalars $-a_\chi = b_\chi = a$, where,

$$a = \frac{\pi^2}{3}\frac{V}{v_{\mathrm{F}}(2\pi\hbar)^3}. \tag{B.5}$$

Boosting $\tilde{T}^{\mu\,\nu}_{\chi\to\chi}(\tilde{Q})$ back to the lab-frame, we find $T^{\mu\,\nu}_{\chi\to\chi}(\mathrm{Q})$ has components,

$$T^{0\,0}_{\chi\to\chi}(\mathrm{Q}) = a|\mathbf{Q}|^2, \tag{B.6a}$$

$$T^{0\,i}_{\chi\to\chi}(\mathrm{Q}) = T^{i\,0}_{\chi\to\chi}(\mathrm{Q}) = \chi a \mathrm{Q}^0\mathrm{Q}^i, \tag{B.6b}$$

$$T^{i\,j}_{\chi\to\chi}(\mathrm{Q}) = a\left[\mathrm{Q}^i\mathrm{Q}^j - g^{i\,j}\left(\mathrm{Q}_0^2 - |\mathbf{Q}|^2\right)\right], \tag{B.6c}$$

where $g^{i\,j}$ is the spatial component of the Minkowski metric. Notice, the only difference between R to R and L to L scattering is the term $\chi\mathrm{Q}^0\mathrm{Q}^i\left(\delta^\mu{}_i\delta^\nu{}_0 + \delta^\mu{}_0\delta^\nu{}_i\right)$, i.e., a sign difference[1] χ. But since $\mathbf{F}^0 = \mathbf{0}$ for time-reversal nodes, see Eq. (6.1), these

[1]This is due to the prefactor $(-1)^{\xi_\chi}$ which originates in the sign difference between σ^μ and $\bar{\sigma}^\mu$

terms will not contribute to the cross-section, which is therefore identical for R to R and L to L scattering. The final result, i.e., Eq. (B.6), is Eq. (4.4) expressed in a non-relativistic notation.

of γ^μ.

Bibliography

[1] P. A. M. Dirac and R. H. Fowler, "The quantum theory of the electron," *Proc. Roy. Soc. Lon.*, vol. 117, pp. 610–624, 1928.

[2] H. Weyl, "Elektron und gravitation. i," *Z. Phys.*, vol. 56, pp. 330–352, 1929.

[3] G. E. Volovik, *The Universe in a Helium Droplet*. International Series of Monographs on Physics, Oxford University Press, 2003.

[4] S. Murakami, "Phase transition between the quantum spin Hall and insulator phases in 3d: emergence of a topological gapless phase," *New J. Phys.*, vol. 9, pp. 356–356, 2007.

[5] S. Murakami, S. Iso, Y. Avishai, M. Onoda, and N. Nagaosa, "Tuning phase transition between quantum spin Hall and ordinary insulating phases," *Phys. Rev. B*, vol. 76, p. 205304, 2007.

[6] X. Wan, A. M. Turner, A. Vishwanath, and S. Y. Savrasov, "Topological

semimetal and Fermi-arc surface states in the electronic structure of pyrochlore iridates," *Phys. Rev. B*, vol. 83, p. 205101, 2011.

[7] H. Nielsen and M. Ninomiya, "Absence of neutrinos on a lattice: (ii). intuitive topological proof," *Nucl. Phys. B*, vol. 193, pp. 173 – 194, 1981.

[8] H. B. Nielsen and M. Ninomiya, "A no-go theorem for regularizing chiral fermions," *Phys. Lett. B*, vol. 105, pp. 219 – 223, 1981.

[9] H. Nielsen and M. Ninomiya, "The Adler-Bell-Jackiw anomaly and Weyl fermions in a crystal," *Phys. Lett. B*, vol. 130, pp. 389 – 396, 1983.

[10] N. P. Armitage, E. J. Mele, and A. Vishwanath, "Weyl and Dirac semimetals in three-dimensional solids," *Rev. Mod. Phys.*, vol. 90, p. 015001, 2018.

[11] B. Yan and C. Felser, "Topological materials: Weyl semimetals," *Annu. Rev. Condens. Matter Phys.*, vol. 8, pp. 337–354, 2017.

[12] M. Z. Hasan, S.-Y. Xu, and G. Bian, "Topological insulators, topological superconductors and Weyl fermion semimetals: discoveries, perspectives and outlooks," *Phys. Scr.*, vol. 2015, p. 014001, 2015.

[13] S.-Y. Xu, I. Belopolski, N. Alidoust, M. Neupane, G. Bian, C. Zhang, R. Sankar, G. Chang, Z. Yuan, C.-C. Lee, S.-M. Huang, H. Zheng, J. Ma, D. S. Sanchez, B. Wang, A. Bansil, F. Chou, P. P. Shibayev, H. Lin, S. Jia, and M. Z. Hasan,

"Discovery of a Weyl fermion semimetal and topological Fermi arcs," *Science*, vol. 349, p. 613, 2015.

[14] S.-M. Huang, S.-Y. Xu, I. Belopolski, C.-C. Lee, G. Chang, B. Wang, N. Alidoust, G. Bian, M. Neupane, C. Zhang, S. Jia, A. Bansil, H. Lin, and M. Z. Hasan, "A Weyl fermion semimetal with surface Fermi arcs in the transition metal monopnictide TaAs class," *Nat. Commun.*, vol. 6, p. 7373, 2015.

[15] H. Weng, C. Fang, Z. Fang, B. A. Bernevig, and X. Dai, "Weyl semimetal phase in noncentrosymmetric transition-metal monophosphides," *Phys. Rev. X*, vol. 5, p. 011029, 2015.

[16] L. X. Yang, Z. K. Liu, Y. Sun, H. Peng, H. F. Yang, T. Zhang, B. Zhou, Y. Zhang, Y. F. Guo, M. Rahn, D. Prabhakaran, Z. Hussain, S. K. Mo, C. Felser, B. Yan, and Y. L. Chen, "Weyl semimetal phase in the non-centrosymmetric compound TaAs," *Nat. Phys.*, vol. 11, p. 728, 2015.

[17] B. Q. Lv, H. M. Weng, B. B. Fu, X. P. Wang, H. Miao, J. Ma, P. Richard, X. C. Huang, L. X. Zhao, G. F. Chen, Z. Fang, X. Dai, T. Qian, and H. Ding, "Experimental discovery of Weyl semimetal TaAs," *Phys. Rev. X*, vol. 5, p. 031013, 2015.

[18] S. Kourtis, J. Li, Z. Wang, A. Yazdani, and B. A. Bernevig, "Universal signatures of Fermi arcs in quasiparticle interference on the surface of Weyl semimetals," *Phys. Rev. B*, vol. 93, p. 041109, 2016.

BIBLIOGRAPHY

[19] H. Inoue, A. Gyenis, Z. Wang, J. Li, S. W. Oh, S. Jiang, N. Ni, B. A. Bernevig, and A. Yazdani, "Quasiparticle interference of the Fermi arcs and surface-bulk connectivity of a Weyl semimetal," *Science*, vol. 351, p. 1184, 2016.

[20] I. Belopolski, S.-Y. Xu, D. S. Sanchez, G. Chang, C. Guo, M. Neupane, H. Zheng, C.-C. Lee, S.-M. Huang, G. Bian, N. Alidoust, T.-R. Chang, B. Wang, X. Zhang, A. Bansil, H.-T. Jeng, H. Lin, S. Jia, and M. Z. Hasan, "Criteria for directly detecting topological Fermi arcs in Weyl semimetals," *Phys. Rev. Lett.*, vol. 116, p. 066802, 2016.

[21] C. M. Wang, H.-Z. Lu, and S.-Q. Shen, "Anomalous phase shift of quantum oscillations in 3d topological semimetals," *Phys. Rev. Lett.*, vol. 117, p. 077201, 2016.

[22] J. Klotz, S.-C. Wu, C. Shekhar, Y. Sun, M. Schmidt, M. Nicklas, M. Baenitz, M. Uhlarz, J. Wosnitza, C. Felser, and B. Yan, "Quantum oscillations and the Fermi surface topology of the Weyl semimetal NbP," *Phys. Rev. B*, vol. 93, p. 121105, 2016.

[23] F. Arnold, M. Naumann, S. C. Wu, Y. Sun, M. Schmidt, H. Borrmann, C. Felser, B. Yan, and E. Hassinger, "Chiral Weyl pockets and Fermi surface topology of the Weyl semimetal TaAs," *Phys. Rev. Lett.*, vol. 117, p. 146401, 2016.

[24] S. Kourtis, "Bulk spectroscopic measurement of the topological charge of Weyl nodes with resonant x rays," *Phys. Rev. B*, vol. 94, p. 125132, 2016.

[25] R. Yu, H. Weng, Z. Fang, H. Ding, and X. Dai, "Determining the chirality of Weyl fermions from circular dichroism spectra in time-dependent angle-resolved photoemission," *Phys. Rev. B*, vol. 93, p. 205133, 05 2016.

[26] F. de Juan, A. G. Grushin, T. Morimoto, and J. E. Moore, "Quantized circular photogalvanic effect in Weyl semimetals," *Nat. Commun.*, vol. 8, p. 15995, 2017.

[27] S. Shivam, R. Coldea, R. Moessner, and P. A. McClarty, "Neutron scattering signatures of magnon Weyl points," *arXiv:1712.08535*, 2017.

[28] M. Bjerngaard, B. Galilo, and A. M. Turner, "Neutron scattering off Weyl semimetals," *Phys. Rev. B*, vol. 102, p. 035122, 2020.

[29] J. D. Bjorken and S. D. Drell, *Relativistic Quantum Mechanics*. International Series in Pure and Applied Physics, McGraw-Hill, 1964.

[30] P. A. Tipler, *Foundations of Modern Physics*. Worth Publishers, Inc., 1969.

[31] M. E. Peskin and D. V. Schroeder, *An Introduction to Quantum Field Theory*. Westviev Press, 1995.

[32] F. Schwalb, *Advanced quantum mechanics*. Springer, 4 ed., 2008.

[33] P. B. Pal, "Dirac, Majorana, and Weyl fermions," *Am. J. Phys.*, vol. 79, pp. 485–498, 2011.

BIBLIOGRAPHY

[34] N. W. Ashcroft and N. D. Mermin, *Solid State Physics*. Brooks/Cole, 1979.

[35] J. Ruan, S.-K. Jian, H. Yao, H. Zhang, S.-C. Zhang, and D. Xing, "Symmetry-protected ideal Weyl semimetal in HgTe-class materials," *Nat. Commun.*, vol. 7, p. 11136, 2016.

[36] M. Buchhold, S. Diehl, and A. Altland, "Vanishing density of states in weakly disordered Weyl semimetals," *Phys. Rev. Lett.*, vol. 121, p. 215301, 2018.

[37] R. Nandkishore, D. A. Huse, and S. L. Sondhi, "Rare region effects dominate weakly disordered three-dimensional Dirac points," *Phys. Rev. B*, vol. 89, p. 245110, 2014.

[38] Z. Huang, T. Das, A. V. Balatsky, and D. P. Arovas, "Stability of Weyl metals under impurity scattering," *Phys. Rev. B*, vol. 87, p. 155123, 2013.

[39] B. Skinner, "Coulomb disorder in three-dimensional Dirac systems," *Phys. Rev. B*, vol. 90, p. 060202, 2014.

[40] S. V. Syzranov, V. Gurarie, and L. Radzihovsky, "Unconventional localization transition in high dimensions," *Phys. Rev. B*, vol. 91, p. 035133, 2015.

[41] J. Von Neumann and E. Wigner, "Über das verhalten von eigenwerten bei adiabatischen prozessen," *Phys. Z.*, vol. 30, pp. 467–470, 1929.

[42] C. Herring, "Accidental degeneracy in the energy bands of crystals," *Phys. Rev.*, vol. 52, pp. 365–373, 1937.

BIBLIOGRAPHY

[43] M. V. Berry, "Quantal phase factors accompanying adiabatic changes," *Prog. Roy. Soc. Lond.*, vol. A 392, pp. 45 – 57, 1984.

[44] Q. Xu, E. Liu, W. Shi, L. Muechler, J. Gayles, C. Felser, and Y. Sun, "Topological surface Fermi arcs in the magnetic Weyl semimetal $co_3sn_2s_2$," *Phys. Rev. B*, vol. 97, p. 235416, 2018.

[45] E. Liu, Y. Sun, N. Kumar, L. Muechler, A. Sun, L. Jiao, S.-Y. Yang, D. Liu, A. Liang, Q. Xu, J. Kroder, V. Süß, H. Borrmann, C. Shekhar, Z. Wang, C. Xi, W. Wang, W. Schnelle, S. Wirth, Y. Chen, S. T. B. Goennenwein, and C. Felser, "Giant anomalous Hall effect in a ferromagnetic kagome-lattice semimetal," *Nat. Phys.*, vol. 14, no. 11, pp. 1125–1131, 2018.

[46] D. F. Liu, A. J. Liang, E. K. Liu, Q. N. Xu, Y. W. Li, C. Chen, D. Pei, W. J. Shi, S. K. Mo, P. Dudin, T. Kim, C. Cacho, G. Li, Y. Sun, L. X. Yang, Z. K. Liu, S. S. P. Parkin, C. Felser, and Y. L. Chen, "Magnetic Weyl semimetal phase in a Kagomé crystal," *Science*, vol. 365, no. 6459, pp. 1282–1285, 2019.

[47] A. A. Burkov, "Topological semimetals," *Nat. Mater.*, vol. 15, pp. 1145–1148, 2016.

[48] A. Bernevig, H. Weng, Z. Fang, and X. Dai, "Recent progress in the study of topological semimetals," *J. Phys. Soc. Jpn.*, vol. 87, p. 041001, 2018.

[49] J.-R. Soh, F. de Juan, M. G. Vergniory, N. B. M. Schröter, M. C. Rahn, D. Y.

Yan, J. Jiang, M. Bristow, P. Reiss, J. N. Blandy, Y. F. Guo, Y. G. Shi, T. K. Kim, A. McCollam, S. H. Simon, Y. Chen, A. I. Coldea, and A. T. Boothroyd, "Ideal Weyl semimetal induced by magnetic exchange," *Phys. Rev. B*, vol. 100, p. 201102, 2019.

[50] A. A. Burkov, M. D. Hook, and L. Balents, "Topological nodal semimetals," *Phys. Rev. B*, vol. 84, p. 235126, 2011.

[51] A. A. Burkov and L. Balents, "Weyl semimetal in a topological insulator multilayer," *Phys. Rev. Lett.*, vol. 107, p. 127205, 2011.

[52] A. Burkov, "Weyl metals," *Ann. Rev. Condens. Matter Phys.*, vol. 9, pp. 359–378, 2018.

[53] H. Weng, R. Yu, X. Hu, X. Dai, and Z. Fang, "Quantum anomalous Hall effect and related topological electronic states," *Adv. Phys.*, vol. 64, pp. 227–282, 2015.

[54] D. Culcer, A. C. Keser, Y. Li, and G. Tkachov, "Transport in two-dimensional topological materials: recent developments in experiment and theory," *2D Mater.*, vol. 7, p. 022007, 2020.

[55] A. W. W. Ludwig, M. P. A. Fisher, R. Shankar, and G. Grinstein, "Integer quantum Hall transition: An alternative approach and exact results," *Phys. Rev. B*, vol. 50, pp. 7526–7552, 1994.

[56] K.-Y. Yang, Y.-M. Lu, and Y. Ran, "Quantum Hall effects in a Weyl semimetal: Possible application in pyrochlore iridates," *Phys. Rev. B*, vol. 84, p. 075129, 2011.

[57] A. B. Bernevig and T. L. Hughes, *Topological Insulators and Topological Superconductors*. Princeton university press, 2013.

[58] T. Meng, *Quantum Critical Matter - Quantum Phase Transitions with Multiple Dynamics and Weyl Superconductors*. PhD thesis, University of Cologne, 2012.

[59] F. D. M. Haldane, "Model for a quantum Hall effect without Landau levels: Condensed-matter realization of the "parity anomaly"," *Phys. Rev. Lett.*, vol. 61, pp. 2015–2018, 1988.

[60] A. M. Turner and A. Vishwanath, *Beyond Band Insulators: Topology of Semimetals and Interacting Phases*, vol. 6 of *Contemporary Concepts of Condensed Matter Science: Topological Insulators*, ch. 11. Elsevier Science, 2013.

[61] J. Y. Liu, J. Hu, Q. Zhang, D. Graf, H. B. Cao, S. M. A. Radmanesh, D. J. Adams, Y. L. Zhu, G. F. Cheng, X. Liu, W. A. Phelan, J. Wei, M. Jaime, F. Balakirev, D. A. Tennant, J. F. DiTusa, I. Chiorescu, L. Spinu, and Z. Q. Mao, "A magnetic topological semimetal $Sr_{1-y}Mn_{1-z}Sb_2$ $(y, z < 0.1)$," *Nat. Mater.*, vol. 16, pp. 905–910, 2017.

[62] Y. F. Guo, A. J. Princep, X. Zhang, P. Manuel, D. Khalyavin, I. I. Mazin, Y. G.

Shi, and A. T. Boothroyd, "Coupling of magnetic order to planar Bi electrons in the anisotropic Dirac metals $A\mathrm{MnBi}_2(A = \mathrm{Sr}, \mathrm{Ca})$," *Phys. Rev. B*, vol. 90, p. 075120, 2014.

[63] Y. Nakajima, R. Hu, K. Kirshenbaum, A. Hughes, P. Syers, X. Wang, K. Wang, R. Wang, S. R. Saha, D. Pratt, J. W. Lynn, and J. Paglione, "Topological RPdBi half-heusler semimetals: A new family of noncentrosymmetric magnetic superconductors," *Sci. Adv.*, vol. 1, 06 2015.

[64] S. Itoh, Y. Endoh, T. Yokoo, S. Ibuka, J.-G. Park, Y. Kaneko, K. S. Takahashi, Y. Tokura, and N. Nagaosa, "Weyl fermions and spin dynamics of metallic ferromagnet SrRuO_3," *Nat. Commun.*, vol. 7, p. 11788, 2016.

[65] W. Yao, C. Li, L. Wang, S. Xue, Y. Dan, K. Iida, K. Kamazawa, K. Li, C. Fang, and Y. Li, "Topological spin excitations in a three-dimensional antiferromagnet," *Nat. Phys.*, vol. 14, pp. 1011–1015, 2018.

[66] S. K. Sinha, J. F. Cooke, and A. P. Murani, "Proceedings of the 1984 workshop on high-energy excitations in condensed matter," techechical report no. la-10227-c-vol.2, Los Alamos National Laboratory, 12 1984.

[67] B. Galilo, "Weyl semimetals," Master's thesis, University of Amsterdam, 2013.

[68] E. Balcar and S. W. Lovesey, *Theory of Magnetic Neutron and Photon Scat-*

tering. Oxford Series on Neutron Scattering in Condensed Matter, Clarendon Press, Oxford, 1989.

[69] L. L. Hirst, "The microscopic magnetization: concept and application," *Rev. Mod. Phys.*, vol. 69, pp. 607 – 627, 1997.

[70] A. G. Grushin, "Consequences of a condensed matter reliazation of Lorentz-violating QED in Weyl semi-metals," *Phys. Rev. D*, vol. 86, p. 045001, 2012.

[71] A. A. Soluyanov, D. Gresch, Z. Wang, Q. Wu, M. Troyer, X. Dai, and B. A. Bernevig, "Type-II Weyl semimetals," *Nature*, vol. 527, p. 495, 2015.

[72] J. Nissinen and G. E. Volovik, "Type-III and IV interacting Weyl points," *JETP Lett.*, vol. 105, pp. 447–452, 2017.

[73] D. C. Lay, *Linear Algebra and its Applications*. Pearson Education Inc., 3 ed., 2006.

[74] J. J. Sakurai, *Modern Quantum Mechaincs*. Addison-Wesley Publishing Company, Inc., 2 ed., 1994.

[75] V. B. Berestetskii, E. M. Lifshitz, and L. P. Piteaevskii, *Relativistic Quantum Theory*, vol. 4 of *Course of Theoretical Physics*. Pergamon Press, 1971.

[76] S. W. Lovesey, *Theory of Neutron Scattering from Condensed Matter*, vol. 2 of *International Series of Monographs on Physics*. Oxford University Press, 1984.

BIBLIOGRAPHY

[77] J. Jensen and A. Mackintosh, *Rare Earth Magnetism - Structures and Excitations*. The International Series of Monographs on Physics, Clarendon Press, Oxford, 1991.

[78] L. D. Landau and E. M. Lifshitz, *Quantum Mechanics (Non-relativistic Theory)*, vol. 3 of *Course of Theoretical Physics*. Butterworth-Heinemann, 3 ed., 1999.

[79] H. Bruus and K. Flensberg, *Many-Body Quantum Theory in Condensed Matter Physics - An Introduction*. Oxford University Press, 2004.

[80] R. D. Mattuck, *A Guide to Feynman Diagrams in the Many-Body Problem*. Dover Publications Inc., 2nd ed., 1992.

[81] C. Y. Guo, F. Wu, Z. Z. Wu, M. Smidman, C. Cao, A. Bostwick, C. Jozwiak, E. Rotenberg, Y. Liu, F. Steglich, and H. Q. Yuan, "Evidence for Weyl fermions in a canonical heavy-fermion semimetal YbPtBi," *Nature Commun.*, vol. 9, p. 4622, 2018.

[82] E. A. Goremychkin, H. Park, R. Osborn, S. Rosenkranz, J.-P. Castellan, V. R. Fanelli, A. D. Christianson, M. B. Stone, E. D. Bauer, K. J. McClellan, D. D. Byler, and J. M. Lawrence, "Coherent band excitations in $CePd_3$: A comparison of neutron scattering and ab initio theory," *Science*, vol. 359, pp. 186–191, 2018.

[83] B. Vignolle, S. M. Hayden, D. F. McMorrow, H. M. Rønnow, B. Lake, C. D. Frost, and T. G. Perring, "Two energy scales in the spin excitations of the high-

temperature superconductor $La_{2-x}Sr_xCuO_4$," *Nat. Phys.*, vol. 3, pp. 163–167, 2007.

[84] A. C. Walters, T. G. Perring, J.-S. Caux, A. T. Savici, G. D. Gu, C.-C. Lee, W. Ku, and I. A. Zaliznyak, "Effect of covalent bonding on magnetism and the missing neutron intensity in copper oxide compounds," *Nat. Phys.*, vol. 5, pp. 867–872, 2009.

[85] M. Fujita, H. Hiraka, M. Matsuda, M. Matsuura, J. M. Tranquada, S. Wakimoto, G. Xu, and K. Yamada, "Progress in neutron scattering studies of spin excitations in high-$T_c$cuprates," *J. Phys. Soc. Jpn.*, vol. 81, p. 011007, 2012.

[86] M. Janoschek, P. Das, B. Chakrabarti, D. L. Abernathy, M. D. Lumsden, J. M. Lawrence, J. D. Thompson, G. H. Lander, J. N. Mitchell, S. Richmond, M. Ramos, F. Trouw, J.-X. Zhu, K. Haule, G. Kotliar, and E. D. Bauer, "The valence-fluctuating ground state of plutonium," *Sci. Adv.*, vol. 1, 2015.

[87] É. D. Kuznetsov and K. V. Kholshevnikov, "Estimation of the number of extrema of a spherical harmonic," *Sov. Aston.*, vol. 36, p. 220, 1992.

[88] C.-K. Chan, P. A. Lee, K. S. Burch, J. H. Han, and Y. Ran, "When chiral photons meet chiral fermions: Photoinduced anomalous Hall effects in Weyl semimetals," *Phys. Rev. Lett.*, vol. 116, p. 026805, 2016.

[89] S. A. A. Ghorashi, P. Hosur, and C.-S. Ting, "Irradiated three-dimensional

Luttinger semimetal: A factory for engineering Weyl semimetals," *Phys. Rev. B*, vol. 97, p. 205402, 2018.

[90] A. Cortijo, Y. Ferreirós, K. Landsteiner, and M. A. H. Vozmediano, "Elastic gauge fields in Weyl semimetals," *Phys. Rev. Lett.*, vol. 115, p. 177202, 2015.

[91] M. P. Ghimire, J. I. Facio, J.-S. You, L. Ye, J. G. Checkelsky, S. Fang, E. Kaxiras, M. Richter, and J. van den Brink, "Creating Weyl nodes and controlling their energy by magnetization rotation," *Phys. Rev. R.*, vol. 1, p. 032044, 2019.

[92] Y. Araki, "Magnetic textures and dynamics in magnetic Weyl semimetals," *Ann. Phys.*, vol. 532, p. 1900287, 2020.

[93] A. Sekine, D. Culcer, and A. H. MacDonald, "Quantum kinetic theory of the chiral anomaly," *Phys. Rev. B*, vol. 96, p. 235134, 2017.

[94] L. Crippa, A. Amaricci, N. Wagner, G. Sangiovanni, J. C. Budich, and M. Capone, "Nonlocal annihilation of Weyl fermions in correlated systems," *Phys. Rev. R.*, vol. 2, p. 012023, 2020.

[95] P.-Y. Chang and P. Coleman, "Parity-violating hybridization in heavy Weyl semimetals," *Phys. Rev. B*, vol. 97, p. 155134, 2018.

[96] V. Ivanov, X. Wan, and S. Y. Savrasov, "Topological insulator-to-Weyl semimetal transition in strongly correlated actinide system UNiSn," *Phys. Rev. X*, vol. 9, p. 041055, 2019.

[97] A. Sekine and K. Nomura, "Electron correlation induced spontaneous symmetry breaking and Weyl semimetal phase in a strongly spin–orbit coupled system," *J. Phys. Soc. Jpn.*, vol. 82, p. 033702, 2013.

[98] S. L. I.B. Khriplovich, CP Violation Without Strangeness: Electric Dipole Moments of Particles, Atoms and Molecules. Springer-Verlag Berlin, 1997.

[99] C. Sun, S.-P. Lee, and Y. Li, "Vortices in a monopole superconducting Weyl semimetal," *arXiv:1909.04179*, 2019.

[100] A. W. W. Ludwig, "Topological phases: classification of topological insulators and superconductors of non-interacting fermions, and beyond," *Phys. Scr.*, vol. T168, p. 014001, 2015.

Vita

Michael Bjerngaard received his M.Sc. degree in physics from the University of Copenhagen, Denmark, in 2011. The following year, he enrolled in the Ph.D. program at the University of Amsterdam, The Netherlands. Following his supervisor Ari M. Turner, Michael Bjerngaard became a Visiting Graduate Student at Johns Hopkins University in 2014. Eventually, he enrolled in the graduate program at Johns Hopkins University under the supervision of Oleg Tchernyshyov in 2017.